TECHNISCHE UNIVERSITÄT WIEN
Vienna University of Technology

Dissertation

Measurement of Linear Gradient Strain Fields at Macroscopic and Microscopic Scale Using Digital Image Correlation

carried out for the purpose of obtaining the degree of Doctor technicae (Dr. techn.), submitted at TU Wien, Faculty of Mechanical and Industrial Engineering, by

Dipl.-Ing. Nedaa Amraish, MSc

Mat.Nr.: 01528544

under the supervision of

Univ.Prof. Dipl.-Ing. Dr.techn. Dieter H. Pahr

Institute of Lightweight Design and Structural Biomechanics, E317

reviewed by

Prof. Dr.
Luca Cristofolini
Dept. of Industrial Engineering,
University of Bologna,
40126 Bologna

Prof. DI Dr.sc.nat.
Philipp J. Thurner
Institute of Lightweight Design and Structural Biomechanics, TU Wien,
1040 Vienna

This thesis was supported partly by the Gesellschaft für Forschungsförderung Niederösterreich m.b.H. via the Dissertation scholarship 2018 [grant number SC18-006], and partly by the Karl Landsteiner University for Health Sciences.

I confirm, that going to press of this thesis needs the confirmation of the examination committee.

Affidavit

I declare in lieu of oath, that I wrote this thesis and performed the associated research myself, using only literature cited in this volume. If text passages from sources are used literally, they are marked as such.

I confirm that this work is original and has not been submitted elsewhere for any examination, nor is it currently under consideration for a thesis elsewhere.

I acknowledge that the submitted work will be checked electronically-technically using suitable and state-of-the-art means (plagiarism detection software). On the one hand, this ensures that the submitted work was prepared according to the high-quality standards within the applicable rules to ensure good scientific practice "Code of Conduct" at the TU Wien. On the other hand, a comparison with other student theses avoids violations of my personal copyright.

Vienna, June, 2024

Nedaa Amraish

For every stateless person in this world,
you belong,
whether others decide otherwise or not!
.....
For Shireen Abu Akleh, the Journalist.
For the +14000 children
the +224 UN workers
the +97 journalists
the +9000 women
killed in Gaza in 6 month.
For Palestine and its life long struggle for freedom!

Acknowledgements

This journey would not have been possible without my husband (Michael Kramer), I thank you for your unconditional support and understanding especially during the hardest times, and for being in my life, 'Ja, wir schaffen es'. I would like to thank my supervisor Prof. Dieter H. Pahr for his supervision, advice and for always thinking of the big picture. As well, I would like to thank my colleagues (Sarah-Jane Estermann, Othniel James Aryeetey, Juan Silva, Morteza Amini, Martin Frank, and Stefanie Stelzer) for the interesting time together, the valuable discussions and the fun lunch breaks. Last but not least, thanks to Lucas Warnung for his help and assistance in the lab, thanks to Christina Penz and Maria Höpfner for their administration assistance.

I would like to thank my family, especially my mother (Aida) and my father (Sade), thank you for your courage and support and for being a role model in persistence and determination, my beloved dad, you may rest in peace, I love you. Thanks to my brothers (Nidal, Hamza, Rafe, Fadi) and sisters (Ahlam, Kifah, Samah, Suzan, Iman, Noor) for being there for me. Our lives are shaped with the people we meet, I would like to thank my teachers from whom I loved science, Kareem Tahboub and Ramzi Qawasmeh, from Palestine Polytechnic University.

Finally, since practically, this thesis would not have been possible without all the research that was conducted before. To the colleagues around the world, you enriched my literature and my mind, so thank you. At the end, life is all about optimization, I wish the next colleagues of PhDs will optimize what I tried to do.

Contents

Abstract

Motivation: Digital Image Correlation (DIC) allows non-contact measurement of mechanical strain fields. Various factors affect its accuracy, necessitating validation for surface strain fields. This work aims to test the applicability of DIC to measure linear gradient strain fields. Despite its advantages, DIC's accuracy validation and filter parameter optimization remains essential, especially for linear gradient strain fields.

Goals: The primary goal of this thesis is to assess the feasibility of measuring linear gradient strain fields at both macroscopic and microscopic scales using DIC. To achieve this main goal, the following sub-goals have been defined: (1) investigate filtering methods for simulated noisy constant strain fields, and simulated noisy linear and quadratic gradient strain fields, (2) experimentally apply DIC to measure linear gradient strain fields on a novelly designed sample at the macroscopic scale (using cortical bone as a case study), and (3) investigate the application of DIC to measure surface strain fields of trabecular bone at the microscopic scale based on the findings of the preceded studies.

Methodological approach: To achieve the first aim, a study was designed to examine various filtering strategies and DIC measuring parameters. Three filtering strategies were applied to determine the optimal filtering parameter suitable for both constant strain fields and gradient strain fields across different strain window sizes. The second aim was pursued by designing an innovative specimen shape capable of exhibiting two pre-defined linear gradient strain fields and a constant strain field region. Finally, the third aim was addressed by utilizing a camera

equipped with a high-resolution telecentric lens. Global and local trabecular strains were investigated.

Main results: The first study demonstrated that employing an optimal filtering strategy reduced noise in simulated constant strain fields and linear gradient strain fields. Gaussian low-pass filtering emerged as the optimal choice, resulting in a significant reduction in error between 60% and 77% for linear and quadratic gradient strain fields for different strain window sizes. The second study revealed the reliability of DIC strain measurements on a novel specimen shape, showcasing two linear gradient strain fields and a constant strain field. DIC accuracy with respect to strain gauges measurements was confirmed in the constant strain field region. Gaussian low-pass filtering enhanced the detection of strain gradients in both biological and engineering samples. The surface strain fields in the measurement area of the specimens exhibited qualitative similarity to results of finite element analyses. The third study showed that employing a telecentric lens enabled the measurement of surface strain fields at the microscopic scale on the surface of trabeculae. At this scale, pure bending states were detected and results showed an 8-fold increase in strain at the edge of the trabeculae compared to the center of the trabeculae. This longitudinal trabecular strain showed no magnification compared to the global strain.

Conclusion: In this thesis, it was found that optimal filtering parameters are necessary to improve the accuracy of DIC measured strains. The effectiveness of the filtering strategies in reducing noise without significantly affecting the measurement data must be tested, similar filters can generate different results. DIC can measure constant strain fields with high accuracy with respect to strain gauges, however, it can measure linear gradient strain fields with certain accuracy. Validating constant strain fields of DIC against strain gauges gives a very good indication of the accuracy of the DIC measurements. Measuring local trabecular strain and investigating bending states of trabeculae at the microscopic scale was possible due to a high-resolution telecentric lens, which counted for out-of-plane movements.

Kurzfassung

Motivation: Die Digital Image Correlation (DIC) ermöglicht die berührungslose Messung mechanischer Dehnungsfelder. Verschiedene Faktoren beeinflussen ihre Genauigkeit, was eine Validierung für Oberflächendehnungsfelder erforderlich macht. Diese Arbeit zielt darauf ab, die Anwendbarkeit von DIC zur Messung linearer Gradientendehnungsfelder zu testen. Trotz ihrer Vorteile bleibt die Validierung der Genauigkeit von DIC und die Optimierung der Filterparameter, insbesondere für lineare Gradienten-Dehnungsfelder, unerlässlich.

Ziele: Das Hauptziel dieser Arbeit ist es, die Machbarkeit der Messung linearer Gradientendehnungsfelder sowohl im makroskopischen als auch im mikroskopischen Maßstab unter Verwendung von DIC zu bewerten. Zur Erreichung dieses Hauptziels wurden folgende Teileziele definiert: (1) Untersuchung von Filtermethoden für simulierte, verrauschte konstante Dehnungsfelder sowie simulierte, verrauschte lineare und quadratische Gradientendehnungsfelder, (2) Experimentelle Anwendung von DIC zur Messung linearer Gradientendehnungsfelder an einer neuartigen Probenform im makroskopischen Maßstab (unter Verwendung von kortikalem Knochen als Fallstudie), und (3) Untersuchung der Anwendung von DIC zur Messung von Oberflächendehnungsfeldern des Trabekelknochens im mikroskopischen Maßstab auf Basis der Ergebnisse der vorangegangenen Studien.

Methodischer Ansatz: Für das Erreichen des ersten Zieles, wurde eine Studie entworfen, um verschiedene Filterstrategien und DIC-Messparameter zu untersuchen. Drei Filterstrategien wurden angewendet, um den optimalen Filterparameter für konstante Dehnungsfelder und Gradientendehnungsfelder über verschiedene

Dehnungsfenstergrößen hinweg zu bestimmen. Das zweite Ziel wurde verfolgt, indem eine innovative Probenform entworfen wurde, die in der Lage ist, zwei vordefinierte lineare Gradientendehnungsfelder und eine konstante Dehnungszone aufzuweisen. Schließlich wurde das dritte Ziel durch die Verwendung einer Kamera mit hochauflösender telezentrischer Linse angegangen. Globale und lokale Trabekeldehnungen wurden untersucht.

Hauptergebnisse: Die erste Studie zeigte, dass die Verwendung einer optimalen Filterstrategie das Rauschen in simulierten konstanten Dehnungsfeldern und linearen Gradientendehnungsfeldern reduzierte. Die Gauß-Tiefpassfilterung erwies sich als optimale Wahl und führte zu einer signifikanten Reduzierung des Fehlers zwischen 60% und 77% für lineare und quadratische Gradientendehnungsfelder bei unterschiedlichen Dehnfenstergrößen. Die zweite Studie enthüllte die Zuverlässigkeit von DIC-Dehnungsmessungen an einer neuartigen Probenform, die zwei lineare Gradientendehnungsfelder und eine konstante Dehnungszone aufwies. Die DIC-Genauigkeit im Vergleich zu Dehnungsmessstreifen wurde in der konstanten Dehnungszone bestätigt. Die Gauß-Tiefpassfilterung verbesserte die Erkennung von Dehnungsgradienten in biologischen und künstlichen Proben. Die Oberflächendehnungsfelder im Messbereich der Proben zeigten eine qualitative Ähnlichkeit zu den Ergebnissen von Finite-Elemente-Analysen. Die dritte Studie zeigte, dass die Verwendung einer telezentrischen Linse mit hoher Auflösung die Messung von Oberflächendehnungsfeldern im mikroskopischen Maßstab auf der Oberfläche von Trabekeln ermöglichte. In diesem Maßstab wurden reine Biegezustände sowie eine 8-fache Zunahme der Dehnung am Rand der Trabekel im Vergleich zum Zentrum festgestellt. Diese longitudinale Trabekeldehnung zeigte keine Vergrößerung im Vergleich zur globalen Dehnung.

Fazit: In dieser Arbeit wurde herausgefunden, dass optimale Filterparameter erforderlich sind, um die Genauigkeit der von DIC gemessenen Dehnungen zu verbessern. Die Wirksamkeit der Filterstrategien bei der Reduzierung von Rauschen, ohne die Messdaten signifikant zu beeinträchtigen, muss vorab getestet werden, da ähnliche Filter unterschiedliche Ergebnisse liefern können. DIC kann konstante Dehnungsfelder mit hoher Genauigkeit im Vergleich zu Dehnungsmessstreifen mes-

sen, jedoch kann es lineare Gradientendehnungsfelder nur mit einer bestimmten Genauigkeit messen. Die Validierung konstanter Dehnungsfelder von DIC gegen Dehnungsmessstreifen gibt einen sehr guten Hinweis auf die Genauigkeit der DIC-Messungen. Die Messung lokaler trabekulärer Dehnungen und die Untersuchung der Biegezustände der Trabekel im mikroskopischen Maßstab waren aufgrund einer hochauflösenden telezentrischen Linse möglich, die Bewegungen außerhalb der Bildebene berücksichtigte.

List of Figures

List of Tables

List of Abbreviations and Symbols

Abbreviations

2D	Two-dimensional
3D	Three-dimensional
BV/TV	Bone volume to total volume
CC	Cross-correlation function
CT	Computed tomography
DIC	Digital image correlation
DFT	Discrete Fourier transform
DVC	Digital volume correlation
FE	Finite element
IFT	Inverse Fourier transform
LPF	Low-pass filter
NA	Not available
NCC	Normalized cross-correlation function
NSDD	Normalized sum-squared difference function
PMMA	Poly methyl methacrylate
RMSE	Root mean square error
ROI	Region of interest
SDD	Sum-squared difference function
SED	Strain energy density
SG	Strain gauge
ZNCC	Zero-normalized cross-correlation function
ZNSDD	Zero-normalized sum-squared difference function

Symbols

ε	Strain [ ]
K_{s}	Gauge factor [ ]
R	Strain gauge's resistance [Ohm]
γ_{xy}	Engineering shear strain [radian]
f	Focal length [mm]
∇u	Displacement gradient tensor field [ ]
F	Deformation gradient tensor [ ]
E_{G}	Green strain tensor [ ]
ε_{xx}	Normal Strain in the $x-$direction [ ]
ε_{xy}	Shear strain [ ]
$\varepsilon_{\mathrm{eq}}$	Equivalent strain [ ]
E	Apparent Young Modulus [GPa]
$\sigma(x)$	Stress at point x [GPa]
λ	Slenderness ratio [ ]
ε_x	Facet-point strain in $x-$direction [ ]
ϕ	Angle deviation from the main loading axis [°]
ε_y	Facet-point strain in $y-$direction [ ]
$\varepsilon_{y'}$	Transformed facet-point strain in $y-$direction [ ]

CHAPTER 1

Introduction

" and God, increase my knowledge."
Quran (20:114)

1.1 Motivation

This section shows the possibilities and challenges of measuring inhomogeneous strain fields in biological samples, especially bones. Inhomogeneous strain fields are characterized by varying strain values across the measured surface, rather than being constant. In this thesis, particular attention is devoted mainly to linear gradient strain fields, where the strain experienced by a material varies linearly along a specific dimension.

Digital image correlation (DIC) was introduced as an alternative method for measuring strain in the 1980s [1]. Full-field strain measurements on the surface of specimens became possible by capturing images during deformation. Due to its advantages in measuring surface strains on specimens with irregular shape and different sizes with a relatively easy sample preparation procedure, this method is being increasingly employed to measure the surface strain of engineering and biological materials in different experimental setups [2, 3, 4, 5]. DIC was employed

to measure homogeneous and inhomogeneous strain fields [6], as well as strain gradients [7, 8, 9]. However, many studies have found that the noise in the DIC strain measurements is considerably high, reaching a few hundred to thousands of micro-strains [10, 11, 12, 13, 14, 15], making the accuracy of this method questionable. Since the strain fields are quantities derived from the displacement, the noise in the original displacement measurements is amplified in the strain fields; in some cases, this does not allow for accurate strain computation [16, 17, 18, 19]. Therefore, measuring small-magnitude strain fields using a DIC technique is challenging due to the signal-to-noise ratio in the strain fields, making noise one of the main limitations for reliable DIC measurements. Further research is needed to explore the reliability of DIC in measuring strain on the surface of irregularly shaped samples where strain gradients are expected and to effectively reduce noise through systematic filtering.

The accuracy of DIC strain measurements can be validated against another, more accurate, method. The DIC strain measurement can either be verified against measurements made with another device, such as strain gauges or extensometers [20, 6, 21, 22], which is limited to one measurement point and does not allow for a full-field strain comparison [23, 15, 24], or using finite element (FE) models [13, 14, 25], which can predict full-field strain measurements. Using parameters such as the geometry, material behaviour and boundary conditions, FE models are suitable for evaluating strain inhomogeneity [25, 26, 27]; thus, these can - under certain considerations - be compared to methods used to perform full-field DIC strain measurements.

Verifying the accuracy of the DIC measurement is not always feasible, because attaching a strain gauge or an extensometer to a sample is not possible, for instance, when measuring the surface strain on the superior neck of human femurs [28, 29]. Here, the noise can be estimated by making a zero-load measurement of strain, which indicates the noise level. Filtering the strain fields plays an important role in noise reduction, but creates a trade-off between losing information and removing noise. Baldoni et al. [13] explored different filtering strategies to reduce the noise while minimizing the loss of information in the DIC strain fields.

Filtering can be applied to the captured images [30, 31, 13], and/or the displacement fields [17, 32, 19, 33, 34, 35], or even to the computed strain fields [13]. Filtering offers the possibility to reduce this noise. However, filters must be carefully chosen, as they predominantly affect areas of strain gradients, and filtering the DIC-captured image has proved to be an ineffective strategy [13, 36, 37]. An optimal filtering parameter that is independent of the load level, strain field size, and the degree of strain concentration has not yet been found. Furthermore, little is known about the accuracy or the effectiveness of the filtering strategies when the deformed specimen results in a linear gradient or inhomogeneous strain fields.

Despite the apparent limitations of the DIC method in measuring the surface strain of engineering materials, it remains a crucial tool for gaining insights into the strain deformation of biological materials, especially at the microscopic scale. Due to their nature, shape, size, and material compositions, biological materials pose greater challenges for strain measurements. For instance, hard tissues such as bone are structurally complex and hierarchically designed, exhibiting multifunctionality and strength. Due to the significant morphological differences in bone, it is divided into cortical and trabecular bone. In terms of mechanical properties, the strength of bone depends on its type, anatomical location, and load-bearing capacity, resulting in cortical bone being stiffer than trabecular bone but more brittle [38, 39]. In contrast to cortical bone, trabecular bone is porous and composed of different individual trabeculae, which are divided into rods and plates [40, 41]. The thickness and separation of these rods and plates significantly contribute to the mechanical properties of trabecular bone.

Different methods have been employed to investigate strains of trabecular bone specimens, see Figure 1.1. Conventional strain measurement techniques such as strain gauges and extensometers, as will be explained later, are not practical for such a measurement because of the sample architecture and porosity which does not allow for an easy clamping, nevertheless, Acciaioli et al [15] managed to clamp an extensometer to a trabecular bone cylinder. The cross-head movement of the testing machine or a clamp-to-clamp can be taken for the displacement and strain

measurement, however, it was found earlier that strains computation based on the relative displacements of the two loading platens, always underestimate apparent modulus of bone samples [42]. DIC and digital volume correlation (DVC) are among the most effective methods for full-field strain analysis. Both methods could be employed to obtain full-field strain of the surface or volumetric strain measurements, for DIC and DVC respectively, as well as using a virtual extensometer for the global strain measurements. DIC was employed to measure full-field surface strain of trabecular bone at a resolution of 10 µ × 10 µm [43], and, DVC was employed for strain measurements at a voxel resolution of 39 µm × 39 µm × 39 µm [44], 24.6 µm × 24.6 µm × 24.6 µm [45], 3.6 µm × 3.6 µm × 3.6 µm [46], and Palanca et al. 1.6 µm × 1.6 µm × 1.6 µm [47]. Despite the numerous advantages and the new insights these techniques can provide, they suffer from some drawbacks that could compromise the strain measurements. In contrast, DIC has an easy sample preparation procedure, can measure full-field strain, and the measurement can be performed while the sample is still hydrated, overcoming the limitation of DVC which risks changing the material properties due to dehydration of the sample.

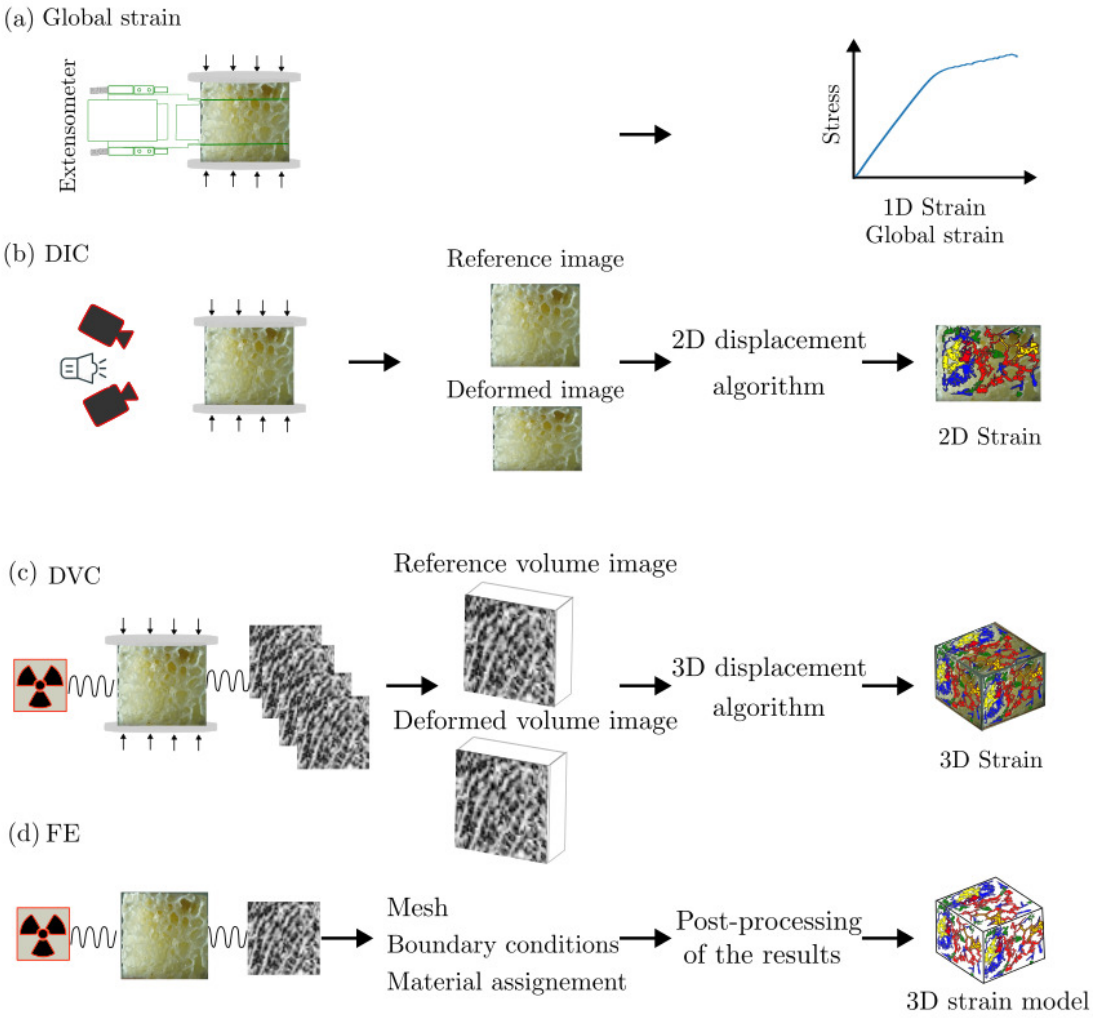

Figure 1.1: Overview of strain acquisition methods of trabecular bone structures where strain gradients are expected. (a) The cross-head movement of the testing machine or an extensometer is used to obtain the global strain of a trabecular structure, this method does not offer strain measurements at single trabeculae, (b) DIC allows for full-field surface strain of trabecular bone structures at the microscopic scale, the measurement is limited to the surface in 2D, details of single trabeculae can be obtained depending on the resolution of the cameras, (c) DVC allows for full-field strain in 3D of the structure at the microscopic scale as well, depending on the voxel resolution, and (d) FE results in strain analysis of the trabecular structure based on specific boundary condition and material properties fed into the FE model.

To reduce the costs of physically testing biological tissues, strain can be obtained from FE analysis. FE models are based on segmented microcomputer tomography (CT) images of trabecular bone. This segmentation is usually based on a global threshold that directly influences bone volume fraction and trabecular connection. Thin trabeculae might get lost in this process, especially if the image resolution is low. High image resolution (voxel size is less than one-fourth of the trabecular thickness [48]) and mesh density and type play a crucial role in the accuracy of the FE models of trabecular bone, mainly when strain and stresses are investigated. Additionally, FE models suffer under the material assignment of trabecular bone, which in many cases is assumed to be linearly elastic and homogeneous [49, 50, 51, 52], even though the apparent modulus of bone ranges between 12 and 25 GPa. FE models that considered trabecular bone as heterogeneous had a lower apparent modulus than specimen-specific homogeneous models, regardless of the volume fraction of the investigated bone and the source of the image for the FE model [53]. Additionally, FE models often lack proper validation of the local strain.

Considering the possibilities and challenges associated with various methods for determining strain in irregular structures, it is scientifically relevant to investigate the DIC method in more detail to obtain reliable full-field surface strain measurements at different length scales, especially at a microscopic scale.

1.2 Goals

The primary goal of this thesis is to assess the feasibility of measuring linear gradient strain fields at both macroscopic and microscopic scales using DIC. To achieve this goal, the following *sub-goals* were defined:

- investigate filtering methods for simulated noisy constant strain fields, and simulated noisy linear and quadratic gradient strain fields
- experimentally apply DIC to measure linear gradient strain fields on a novelly designed sample at the macroscopic scale (using cortical bone as a case study)

- investigate the application of DIC to measure surface strain fields of trabecular bone at the microscopic scale based on the findings of the preceded studies.

Based on these tasks, this thesis work is composed of three studies which are graphically summarized in Figure 1.2.

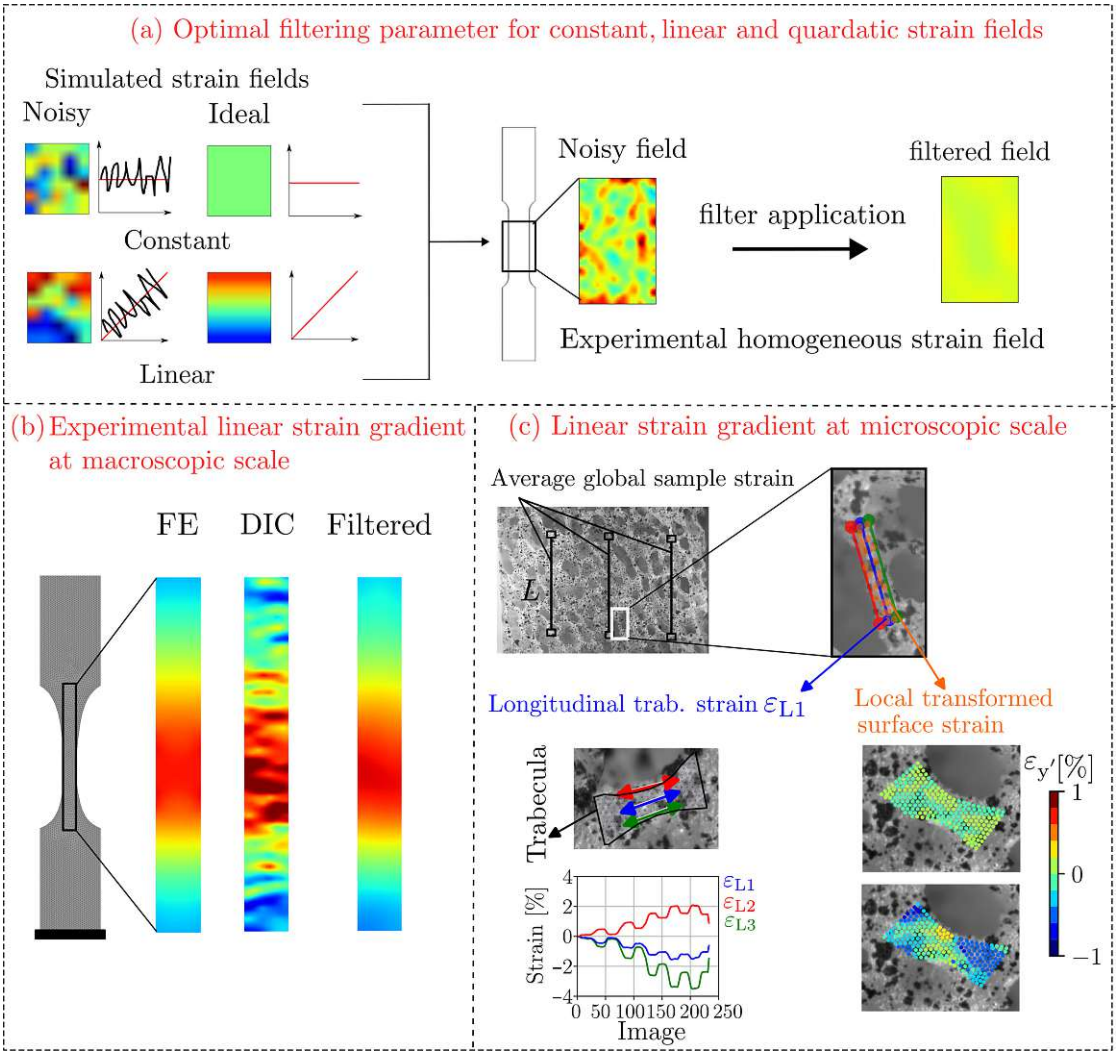

Figure 1.2: Overview of this thesis work. (a) To reduce the noise in DIC fields, filtering options were applied to noisy simulated constant strain fields, and to linear and quadratic gradient strain fields. The optimal filter parameters were applied to experimentally constant DIC strain fields from a steel specimen. (b) To test the application of DIC beyond constant strain fields, a novel specimen shape was designed to investigate the accuracy of DIC strain measurements for measuring linear gradient fields experimentally at the macroscopic scale. (c) A special DIC system with a telecentric lens was used to investigate the applicability of using DIC to measure surface strain at the microscopic scale of trabeculae.

1.3 Thesis outline

This section gives an overview of the content of the different chapters of this thesis.

Chapter 2 provides a literature review of DIC applications in bone strain analysis.

Chapter 3 provides relevant background information. The following topics are addressed: strain measurement methods applied in this thesis work (section 3.1), providing detailed information about the working principle of strain gauges (section 3.1.1), extensometers (section 3.1.2), and DIC (section 3.1.3), the accuracy and precision of strain measurement (section 3.2), and different filtering approaches applied to DIC strain measurements (section 3.3).

Chapter 4 describes a study carried out to investigate the potential for using different filtering options, namely, simple mean filtering, Gaussian mean filtering, and Gaussian low-pass filtering (LPF) methods, to reduce noise in simulated strain fields while maintaining the full-field information based on constant strain fields, and linear and quadratic gradient strain fields. The findings were then applied to experimentally constant DIC strain fields for steel specimens.

Chapter 5 describes a study on strain gradient fields. In this study, a novel specimen shape showed two linear gradients (high- and low-gradients) under deformation. This novel specimen was used to investigate the accuracy of DIC strain measurements for measuring strain gradients. Strains were obtained globally (full-field) and locally (at strain gauges positions). The optimal filtering option described in Chapter 4 was applied to reduce the noise in the full-field DIC strain for engineering and biological materials.

Chapter 6 describes a study in which a special DIC system with a telecentric lens was employed to investigate the applicability of using DIC to measure surface strain at the microscopic scale for individual trabeculae within their trabecular structure. As well, evaluating the strain magnification between the global sample

strain and the longitudinal trabecular strains of different trabeculae.

Chapter 7 summarizes the main findings, providing concluding remarks and suggestions for future research.

1.4 List of appended papers

In the course of this thesis three peer-reviewed publications were published.

Amraish, N., Reisinger, A., Pahr, D.H. Robust Filtering Options for Higher-Order Strain Fields Generated by Digital Image Correlation. Appl. Mech. 2020, 1, 174-192. https://doi.org/10.3390/applmech1040012

Amraish, N., Reisinger, A., Pahr, D. A novel specimen shape for measurement of linear strain fields by means of digital image correlation. Sci Rep 11, 17515 (2021). https://doi.org/10.1038/s41598-021-97085-x

Amraish, N., Pahr, D. High-resolution local trabecular strain within trabecular structure under cyclic loading. JMBBM (2023) https://doi.org/10.1016/j.jmbbm.2023.106318.

CHAPTER 2

Literature review of DIC applications in bone strain analysis

Biomechanics is a multidisciplinary field that investigates the forces, stresses, strains, motions, and mechanical properties of biological tissues to gain insights into their behaviour and characteristics. These insights contribute to a better understanding of the mechanical response of biological tissues, with the potential to advance the research for treatments and interventions to improve the quality and function of these tissues. One of the tissues of interest in biomechanics is bone, which is particularly susceptible to forces, stresses, and strains, and exhibits responses to mechanical loading.

This section provides an overview of studies that have utilized DIC to measure strain fields on bone tissue, since cortical and trabecular bone specimens were employed as an example in this thesis to assess the applicability of DIC for measuring linear gradient strain fields. A homogeneous strain field is one where the strain is constant for all points on a surface. This condition can be achieved if the specimen has a simple geometry and the deformation remains within its elastic range. For instance, engineering materials such as steel or aluminum, with standard

geometrical forms like a dog-bone shape, exhibit homogeneous strain fields in the gauge region when loaded below their yield points. The yield point marks the onset of plastic deformation in the specimen. In such cases, DIC may not be the optimal choice for strain measurement since strain can be accurately measured using strain gauges or extensometers. Homogeneous strain fields can be utilized to verify the accuracy of DIC strain fields for standard specimens such as aluminum [54, 30, 13, 15] or steel [55] with a constant cross-section. For these samples, strain gauges or extensometers can be employed to estimate the error in DIC strain measurements. In contrast to homogeneous strain fields, inhomogeneous (or heterogeneous) fields do not exhibit constant strain values at all points; instead, the strain fields vary in terms of strain magnitude across the surface. Engineering and many biological materials often demonstrate a non-uniform distribution of plastic strain. Strain gradients may be present in specimens with irregular shapes [56] or in specimens composed of composite materials [57, 58]. Unlike specimens with homogeneous strain fields, strain gradients cannot be measured using a single strain gauge or an extensometer.

For engineering materials, many studies have applied DIC to measure inhomogeneous strain fields. Heterogeneity in the strain fields can occur due to various factors, such as the loading condition, as observed when a rubber-like material is subjected to biaxial loading [59, 60], or due to strain localization resulting from different deformation temperatures [61, 36], or even due to the material composition itself. Examples of the latter include fiber-reinforced composites [62], talc- and elastomer-modified polypropylene compounds [63], carbon-carbon composite materials [57], and thin and flat steel specimens [64]. Furthermore, complex geometry can lead to inhomogeneous deformation measurements in specimens containing pores [65, 66, 67] or complex structures [68, 69, 70]. DIC measurement is an advantageous method not only for measuring inhomogeneous strain fields but also for measuring strain gradients [7, 8, 9, 58], as well as strains beyond the yielding point of a material [71].

Heterogeneity in the strain fields predominates in non-engineering materials, particularly in biological tissues, which exhibit complex geometrical forms and material

compositions [72, 6, 73]. Bone, one of the tissues in the human body subject to mechanical loading, is structurally complex and hierarchically designed, possessing multifunctionality and strength. It can endure significant compression loads, serving as the load-bearing component of the human skeleton [74]. Bone tissue facilitates movement and shields vital organs, with its mechanical properties being crucial for its functionality. Deterioration in these properties due to aging and/or disease can lead to severe consequences, such as hip fractures, which contribute to both mortality and morbidity [75]. Cortical and trabecular bone represent two distinct types, each exhibiting significant morphological differences. Therefore, comprehensively understanding the mechanical behavior of bone is intricate, given the intricate interplay among bone physical loading, material deformation, and mechanical response. This complexity is reflected in the strain fields, which are best assessed using a contactless optical measurement device such as DIC.

In recent years, DIC has been employed often to measure full-field surface strain in bone specimens, see table 2.1.

The noise in DIC strain measurements is non-negligible. However, most studies that have measured DIC strain on macroscopic scale bone samples, such as the femoral bone, have focused on validating DIC strain measurements and/or reducing the noise in the DIC strain fields. For microscopic scale bone samples, noise in the DIC strain was not systematically reported or reduced.

At a macro-scale, DIC measurements of strain were obtained for human femoral bone tested in a configuration resembling a single stance [6, 14] and a fall to the side [87, 28, 29]. In the stance configuration, Hensley et al. [14] verified the DIC strain locally with strain gauges in cadaveric and composite femurs. The authors found an average relative difference between DIC and strain gauges for cadaveric specimens of 74±95 μstrain for maximum and 52±31 μstrain for minimum principal strains respectively, with half of the difference found in composite femurs. Variability in strain gauge application and measurement on hard tissues related to bone temperature and surface features such as micro holes, protuberances, and wrinkles contributed to the variation seen in the cadaveric femurs [89, 14].

Table 2.1: Overview of publications that measured strain on bone specimens using DIC.

Bone sample	n	Loading	DIC	Noise [$\mu\varepsilon$]	Strain field
Bull trabeculae [76]	31	tensile	2D	NA	yes
Bovine trabeculae [77]	30	tensile/bending	2D	NA	no
Human trabecular [43]	30	compression	3D	NA	no
Human trabecular [78]	10	wedge splitting	2D	NA	yes
Bovine trabecular [79]	7	wedge splitting	2D	NA	no
Swine trabecular [52]	10	compression	2D	NA	yes
Bovine trabecular [80]	20	compression	2D	NA	yes
Human vertebrae [81]	6	compression	3D	NA	no
Porcine vertebrae [82]	10	compression	3D	500	yes
Porcine vertebrae [83]	8	compression	3D	NA	no
Porcine vertebrae [84]	3	compression	3D	140	yes
Porcine vertebrae [85]	3	compression	3D	180	yes
Murine tibia [58]	4	compression	3D	300	yes
Mouse forearm [21]	3	compression	3D	2000	yes
Bovine femora [86]	10	tensile	3D	NA	yes
Human femora [6]	3	compression/stance	3D	659	yes
Human femora [14]	4	compression/stance	3D	169	yes
Human femora [87]	20	compression/fall	3D	375	yes
Human femora [28]	12	compression/fall	3D	NA	yes
Human femora [29]	10	compression/fall	3D	200	yes
Human femora [88]	5	compression/fall	3D	137	yes

Grassi et al. extensively studied the human femur [20, 6, 90, 28]. In one study [20], they used DIC to validate FE models on six composite femurs, and the root-mean-square error varied between approximately 600 µstrain and 1700 µstrain. Composite femurs were used as an example of complex geometry to test the feasibility of DIC to accurately measure strain in such structures [91, 92, 93, 14]. In another study [6], the authors obtained full-field strain measurements in three human femurs at physiologically relevant strain rates. A control plate was used to evaluate the noise, and the average major principal strain on the control plate while the machine was turned on but not operating was less than 50 µstrain, with a maximum value of 361 µstrain. During testing, the noise increased, and the maximum recorded major principal strains during the test were slightly below 700 µstrain [6]. Nevertheless,

strain localization was detected in the full-field strain data on the femoral neck. Subsequently, Grassi et al. [90] validated a subject-specific FE model with DIC strain fields in three specimens in a single-leg-stance configuration. The results indicate that the subject-specific FE model could predict the strain response and fracture load. The accuracy of the measurements was evaluated by pooling all the DIC strain data and comparing it with the FE strain data for the same area, resulting in a determination coefficient (R^2) of 0.94, regression slope of 0.96, and intercept of 133 μstrain [90].

The femur was not only tested in the stance configuration but also in a fall-to-the-side configuration. Gilchrist et al. [87] measured DIC strain fields on the bones of 20 femoral necks and validated the DIC measurements against those measured with strain gauges. The results indicate that the minimum principal strains were accurate to 127±239 μstrain [87], with no filtering applied to the strain fields or the collected DIC images. Likewise, Grassi et al. [28] tested twelve cadaveric femurs, but these authors employed a bilateral DIC system to measure strains on the medial and lateral sides of the femoral neck. Strain localizations were detected in the DIC strain fields near the cortical pores [28]. Not all studies reported the accuracy of the strain measurement or followed a systematic approach to reduce noise. Indeed, few studies followed a systematic approach to validate strain in femoral bone. For instance, DIC strains were compared to strain gauges to quantitatively assess the validity of FE models [14, 24]. Additionally, DIC measurements provided insights into the influence of implants on the femur. The use of DIC enabled strain-shielding zones to be identified due to the hip implant [94, 88], and different strain pattern distributions were detected for different implants [95].

Bone from different animal models has also been investigated using DIC. Sztefek et al. [58] measured the full-field surface strain of a murine tibia during compressive loading, and the strain fields showed a local strain response that could not be obtained with another measurement method. A mouse forearm was also studied using three strain measurement methods: strain gauges, DIC, and FE. The FE and DIC results differed by 3-14%, while the strain gauge values and the FE results differed between 37-56% [21]. Different factors contributed to these variations in

the strain measurements; the FE strain is influenced by bone geometry, and the attachment of the strain gauges to the bone specimens artificially stiffens the bone and restricts its deformation [21]. Gustafsson et al. [86] studied bovine cortical bone of different lengths with DIC and small/wide-angle X-ray scattering to link the local deformations at the tissue and nanoscales. These authors found that the strain magnitude at all lengths was influenced by the orientation of the microstructure relative to the tensile loading [86].

The vertebrae have also been subjected to strain analysis using DIC. Due to the heterogeneity and complex geometry of vertebrae, strain cannot be measured with a single strain gauge. Spera et al. [82] applied 3D DIC on a fresh porcine functional spine unit loaded under anterior, posterior, and lateral compression. An analysis of the DIC strain fields revealed detailed information about local variations in the structural response when the load was applied to different regions of the porcine intervertebral disc [82]. High-speed 3D DIC was used to make surface strain measurements of porcine cervical spinal specimens subjected to high-speed impacts applied using a falling mass of 12.86 kg [83]. Subsequently, strain distributions were obtained across the lateral and frontal views of a vertebral body, and on the intervertebral discs and ligaments of four vertebrae extracted from a porcine spine using 3D DIC [84]. An analysis of strain fields showed that the intervertebral disc had higher strain values (i.e., tens of thousands of microstrain) than the vertebral body (i.e., below 2000 μstrain) [84], and these results were confirmed by Palance et al. [85], who also detected strain gradients in a DIC analysis of spine segments.

Trabecular bone, at the micro-scale, is also of interest for DIC strain analysis. This type of bone is porous and composed of thin rods and plates of bone tissue; it is typically found at the ends of long bones such as the femur. Trabecular bone undergoes morphological changes due to age and/or disease, which can weaken it and make it susceptible to fracture. Characterizing trabecular bone is more challenging than cortical bone due to its highly inhomogeneous geometry and the difficulties associated with sample preparation and displacement measurement in such a porous structure. Only five studies have investigated trabecular bone strain fields using DIC, as shown in Table 2.1.

In the work of Acciaioli et al. [43], despite using a 3D DIC system, it was not possible to conduct a local strain investigation of the surface of single trabeculae due to the presence of large pores in some regions of the trabecular bone. Nevertheless, a good agreement was found between the apparent elastic modulus from DIC and the physical extensometer. Bokam et al. [79, 78] employed 2D DIC on bovine and human bone with cement. In their first study [79], a bovine trabecular bone was subjected to a wedge-splitting test to precisely define crack tip positions and measure crack opening displacement. Although this study reports full-field strain for a 15 $\times$15 mm^2 surface area, it does not provide information on the local strain fields of single trabeculae, and no differentiation between pores and trabeculae was made. Their second study [78] investigated the fracture behavior of cancellous bone and the cancellous bone-poly methyl methacrylate (PMMA) bone cement interface. Similar to the first study, neither local strain fields at single trabeculae nor differentiation between pores and trabeculae were addressed. Tsirigotis et al. [80] and Belda et al. [52] employed a 2D-DIC system to measure the deformation of trabecular bone under a compression test. Belda et al. [52] accompanied their measurements with micro-CT scans at a 22 µm spatial resolution, which was used for the FE model. The authors found that the equivalent strain was the best predictor of the compression fracture pattern for both methods, DIC and FE. It is worth noting that Belda et al. did not apply speckle patterns to the sample, but instead relied on the irregular microstructure of the trabecular bone. The full-field strain reported in this study was interpolated, and the strain of single trabeculae was not identified. However, a crack region could be identified, and the peak strain differences between FE and DIC ranged from 10-24% [52]. Tsirigotis et al. [80], on the other hand, showed interpolated surface strain fields with steep strain gradients; however, no local strain analysis was conducted in their study.

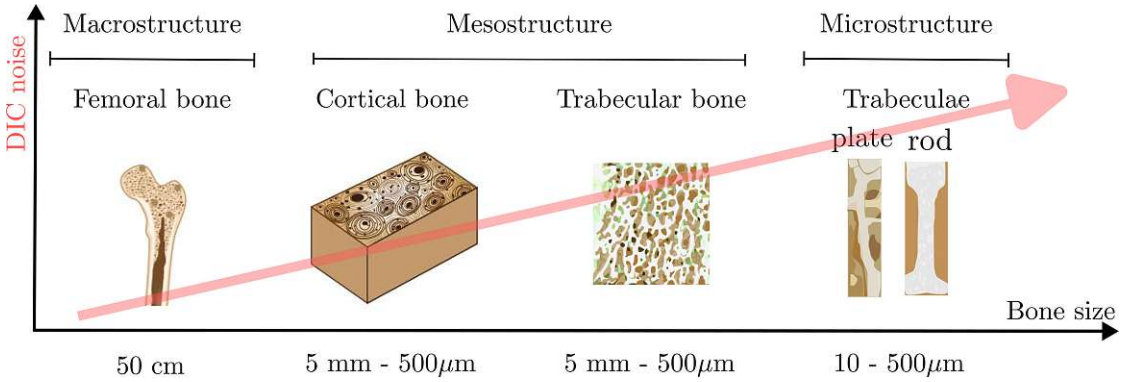

Figure 2.1: Schematic representation of DIC noise versus bone sample size. As the size of the test sample decreases, a loss of spatial resolution will lead to increased uncertainties in DIC measurements.

The literature review of DIC applications in bone strain analysis provides valuable insights. Researchers have extensively used DIC to assess full-field surface strain in femoral bone specimens, detecting strain localizations within DIC strain fields. Validation studies have compared DIC measurements to strain gauges, revealing variations across different femoral bone configurations, including cadaveric and composite specimens. Studies examining full-field strain measurements in human femurs have highlighted noise levels during testing. However, it is notable that not all studies, especially those focusing on trabecular bone, reported the accuracy of strain measurements or employed systematic approaches to reduce noise. While it's true that strain gauges cannot be attached to bone samples at the microstructure level, there are approaches to investigate the noise level in DIC strain measurements, such as at zero load. It is known that the noise of DIC strain measurements increases for small-scale measurements, as schematically represented in Figure 2.1. Some studies systematically validated strain measurements in femoral bone using DIC, with a few comparing DIC strains to strain gauges for quantitative assessment. These findings highlight the importance of both rigorous validation of DIC strain measurements and systematic approaches to ensure accurate results.

In the next chapter, a theoretical background is provided on the strain measurement methods applied in this thesis work, including the accuracy and precision of DIC, as well as some filtering approaches to reduce noise in DIC strain measurements.

CHAPTER 3

Theoretical background

This chapter explains the experimental strain measurement methods applied in this thesis work, including strain gauges, extensometers, and DIC. Explanations are provided for their working principles, with special attention given to the accuracy of DIC measurements. Different filtering options to improve DIC accuracy for strain measurements are also presented.

3.1 Strain measurement methods

Strain is a measure of the deformation undergone by a material subjected to external forces. In this section, three strain measurement methods are explained.

3.1.1 Strain gauges

Strain gauges, invented almost a century ago, can be used to measure the localized deformation of materials. They usually consist of fine wire or foil assembled in a grid pattern, as shown in Figure 3.1(a). In principle, they are constructed from a single wire wound back and forth. When a compression or tensile force is applied, the electrical resistance in the wires decreases or increases, respectively. This

change in resistance can be measured and used to calculate the strain ε using the following formula:

$$\varepsilon = \frac{\Delta R}{R} \frac{1}{K_s} \tag{3.1}$$

where R is the resistance of the conductor in the non-deformed state, ΔR is the change in resistance, and K_s is the gauge factor, which expresses the sensitivity of the strain gauge. Multiple strain gauges can be combined to measure strain in different directions, forming what are called strain gauge rosettes, as illustrated in Figure 3.1. A biaxial rosette utilizes two strain gauges mounted perpendicular to each other, as shown in Figure 3.1(b). The term "biaxial" indicates that a 2D analysis of strain is performed in the xy-plane. In a triaxial rosette, the strain gauges are oriented at 0°-45°-90° angles relative to each other, as depicted in Figure 3.1(c), or at 0°-60°-120° angles. Strain gauges are considered the gold standard for strain measurement due to their high accuracy. However, applying a uniaxial strain gauge is less complicated than using biaxial or triaxial rosettes. Depending on the strain being investigated, a uniaxial gauge might be sufficient. For instance, Cristofolini and Viceconti [96] compared the use of uniaxial and triaxial gauges for investigating stress-shielding on the femur and concluded that uniaxial gauges are sufficient, simplifying the experimental setup compared to when a triaxial rosette is used.

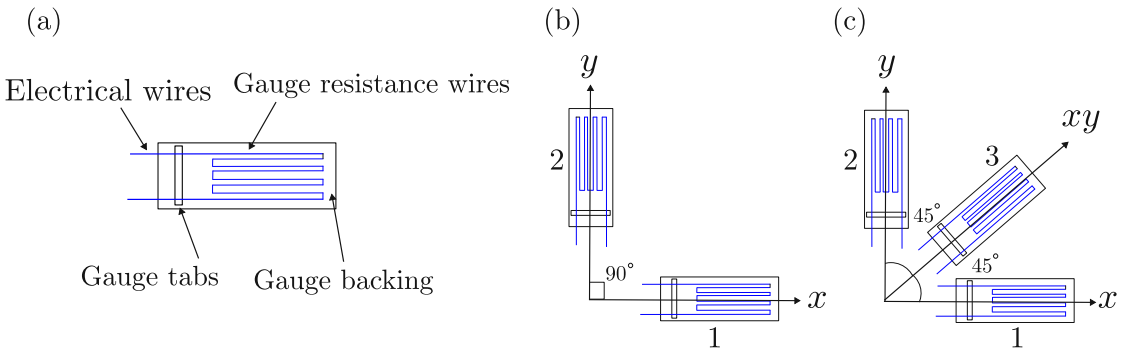

Figure 3.1: Strain gauges are made of fine wire (in blue) which their resistance change when force is applied. A single strain gauge can be used to measure strain as in (a), or a combination of strain gauges can be used to measure strain in multiple directions as in the biaxial or triaxial rosette, (b) and (c), respectively.

Each strain gauge measures strain in only one direction; thus, two gauges, forming a biaxial rosette, are needed to determine strain in the x and y directions. However, shear strain cannot be directly measured by a strain gauge. In Figure 3.1(b), the strain measured by strain gauge 1 is equal to the strain measured in the x direction ($\varepsilon_1 = \varepsilon_x$), and the same applies for the y direction ($\varepsilon_2 = \varepsilon_y$). While the same is true for ε_1 and ε_2 in Figure 3.1(c) (a triaxial rosette), the shear strain γ_{xy} can be computed as $\gamma_{xy} = 2\varepsilon_3 - (\varepsilon_1 + \varepsilon_2)$.

The bonding of the strain gauge to the specimen highly influences the accuracy of the measured strain. To achieve a good bond, a clean and rough specimen surface is needed. Unlike engineering materials that can be easily cleaned and roughened if needed, biological specimens pose more challenges. The main disadvantage of using strain gauges is that they can only measure strain where they are applied, meaning that many strain gauges must be applied to the material's surface to capture a representative strain distribution [97, 98, 99]. In 1966, Roberts [100] developed a procedure for applying strain gauges to bone samples, where strain gauges are glued to the surface using cyanoacrylate glue or epoxy resins, then waterproofed using a sealant [100, 98, 101]. This process is challenging because the bone surface must be thoroughly cleaned to remove soft tissues and degreased using acetone, which could introduce variations in strain measurements [89, 14]. Nevertheless, the root-mean-square noise of the minimum and maximum principal strain signals of

a strain gauge rosette attached to porcine vertebrae can be as small as 1 μstrain [23].

Due to their accuracy, strain gauges have been increasingly applied to investigate strain in bone samples. Kim et al. [98] investigated the influence of hip implants on the strain distribution of proximal human cadaver femora by applying ten strain-gauge rosettes to the surface of six femora. As described by Roberts [100], the site of strain gauge application was cleaned from soft tissues, smoothed with sandpaper, degreased using acetone, and then dried in an O_2 stream. Finally, before bonding the strain gauge, an etchant was applied to the application site and rinsed with saline. After drying, the strain gauges were bonded using a two-component poly methyl methacrylate (PMMA) adhesive and covered with a waterproof epoxy sealant [98]. However, strain gauge coatings have not proven effective in other studies by Begonia et al. [102, 21], where strain gauges were applied to the medial forearm surface of mice bones. Strain gauges have been applied not only *in vitro* but also *in vivo* [103, 104]. Lanyon et al. [105] applied a triaxial strain gauge rosette to the anteromedial aspect of the tibial midshaft of a man. The preparation steps included surgery to gain access to the strain gauge site, tissue infiltration with a local anesthetic solution, careful wiping of the strain gauge site, treatment with a surface activator, application of adhesive to the underside of the gauge, pressing the gauge into position, suturing the wires of the gauge to the periosteum, and closing the wound, leaving the wires to emerge from the proximal end of the incision [106, 105].

Due to the challenges in applying strain gauges to cadaver bone samples, many researchers have opted to use composite bones, which do not significantly differ from cadaver bone samples [107], to study the influence of various parameters on strain distribution. Composite bones mitigate variations in the material itself and allow for the study of strain distribution based on factors such as inclination angle, implants, or loading conditions [108, 93, 109]. In the case of composite femora, strain gauges are bonded to the surface using adhesive glue [109], eliminating the need for surface treatment.

Application of strain gauges to specific locations on the measured surface is benefi-

cial not only for measuring local strain but also for validating strain measured by other, less accurate techniques [107, 23]. Applying strain gauges to the surface of the human femur has been beneficial for validating finite element models [97, 110, 111]. However, the strain measured by strain gauges can also be underestimated due to the stiffness of the gauges when applied to thin materials [112, 89]. In conclusion, strain gauges are widely used for mechanical strain measurement on bone tissue. However, their application is limited to local strain measurement on the surface of tissues, and their accuracy depends largely on the quality of the gauges themselves and their attachment to the surface.

3.1.2 Contact extensometers

An extensometer is a device used to measure changes in the length of an object. The strain can then be calculated as the change in length divided by the original length. Contact extensometers, such as clip-on extensometers, are mounted directly onto the specimen, which is usually flat with a constant thickness, as shown in Figure 3.2. Extensometers provide accurate measurements because no relative movement occurs between the specimen and the extensometer due to the short and stiff mechanical parts that transfer the extension from the specimen to the internal transducer. The main disadvantage of using contact extensometers is that their measurement range is limited to a few millimeters, they can only measure in one direction, the measurement accuracy can be impaired for small or delicate specimens, the thickness of the measured area has to be uniform, and the pins of the clip-on extensometer can mechanically interact with the specimen, causing significant creep indentation, which, in turn, results in an overestimation of the specimen's transverse strain [71].

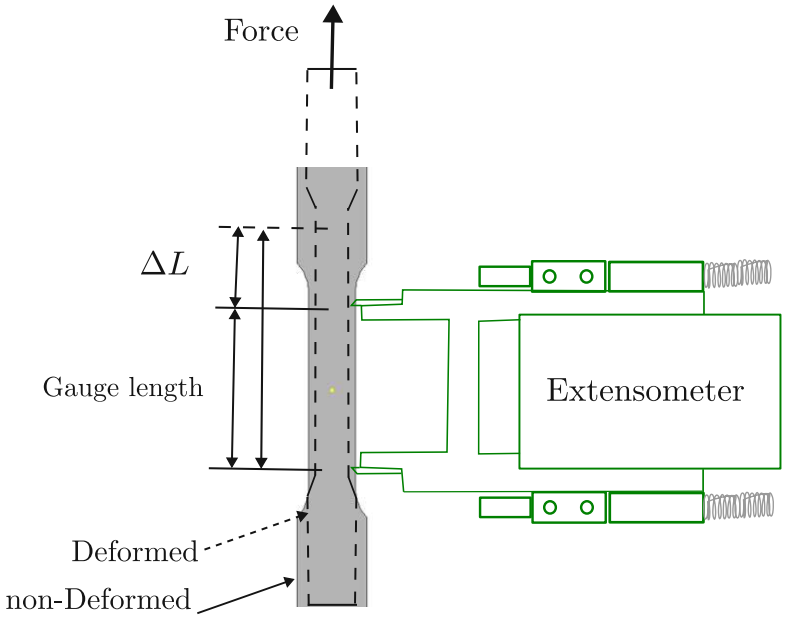

Figure 3.2: An illustration of a contact extensometer. When the sample is deformed under an external force, the extensometer measures a change in the length ΔL. The strain can then be calculated as the change in length divided by the gauge length.

The strain ε can be simply calculated using the following formula:

$$\varepsilon = \frac{\Delta L}{L} \tag{3.2}$$

where L is the original length of the extensometer, and ΔL is the length change due to the elongation or shortening of the sample. Extensometers are more accurate than measurements based on the motion of the testing machine's cross-head because they are mounted directly on the sample. There are a variety of commercially available extensometers that differ in shapes, sizes, measuring capacities, and temperature ratings. The advantages of extensometers over strain gauges lie in their reusability, making them very cost-effective. For engineering materials, extensometers are used to accurately measure material properties, which are homogeneous and require specimen preparation according to ASTM International guidelines for the respective material. However, extensometers are not the first choice when measuring strain in biological tissues due to their limitations regarding

the shape of the specimens. Nevertheless, modified extensometers have been applied to gain more information from the sample under test. For instance, Acciaioli et al. [43] used a four-extensometer technique to measure local axial displacements of cylindrical human trabecular bone specimens. The four-extensometer technique involves attaching two extensometers simultaneously to the specimen using four rubber bands. Initially, two extensometers are positioned vertically at 0° and 180° along the generatrix of the cylindrical specimen, and then they are re-positioned vertically at 90° and 270° [43], allowing for four strain measurements on the surface of the specimen.

As well, Boyd et al. [113] measured uniaxial strain of cylindrical cancellous bone cores extracted from canine femoral condyles during a uniaxial compression test. In this study, the researchers compared the extensometer measurements to the cross-head movement of the testing machine and a clamp-to-clamp measurement using a linear potentiometer between the two loading platens. A good correlation was found between the clamp-to-clamp and cross-head displacement measures, which was not found between the extensometer and both other methods [113]. Earlier studies have found that strain computations based on the relative displacements of the two loading platens always underestimate Young's modulus of bone samples [114, 42].

Extensometers were also used in *in vivo* applications to measure strain rate and/or magnitude. Perusek et al. [115] measured global strain and strain rates in human calcaneus bone during physiological activity. The applied extensometer incorporated two capacitive sensors mounted to intraosseous pins, allowing for strain measurement due to bending in the plane of the extensometer, in addition to uniaxial compression or tension strain measurement [115]. The application of extensometers *in vivo* is less invasive compared to strain gauges and requires less surface preparation.

3.1.3 DIC

Even two decades ago, DIC was being employed to measure strains on the surface of a wide range of materials [1]. DIC systems use a series of sequential digital images to determine the surface deformation and strain of objects. These systems can identify features of an object and track their relative movement across the sequential images. By tracking deformation across the surface, full-field measurements can be obtained, overcoming limitations imposed by strain gauges, which require many gauges to be glued to the specimen's surface for a complete strain distribution picture. This advantage of DIC over other measuring techniques has allowed researchers to track surface deformation and characterize highly anisotropic and inhomogeneous biological samples [6, 23, 116].

Camera systems. DIC systems operate in both two (2D) and three dimensions (3D), as depicted in Figure 3.3. The distinction between these systems lies in the number of cameras or lenses used to capture images. A 2D DIC system utilizes a single camera with one lens, which can be either standard or telecentric, while a 3D DIC system employs two cameras for stereo vision.

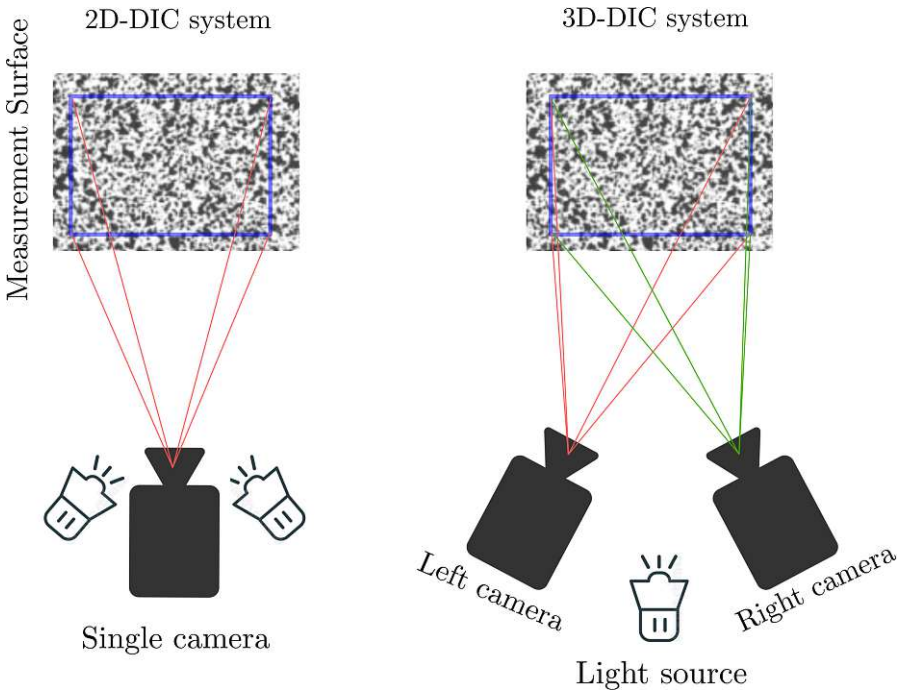

Figure 3.3: DIC measurements can be performed in 2D or 3D using a single camera or stereo cameras, respectively.

The accuracy associated with the camera system helps to determine the DIC system used for surface strain measurement. This accuracy varies between 3D and 2D DIC systems. The former uses two cameras in stereo vision to capture the object from different angles, so that no pseudo strain measurements are detected when the object moves in or out of the focal plane, resulting in more accurate strain measurements [117]. In contrast, a 2D DIC system with a standard lens can be more inaccurate due to out-of-plane movements which cause in-plane strain measurement errors. This limitation of the 2D DIC system can be partly overcome when a telecentric lens is used; due to its working principle, this lens is less sensitive to out-of-plane movement [117]. Figure 3.4 shows the difference between a standard and a telecentric lens.

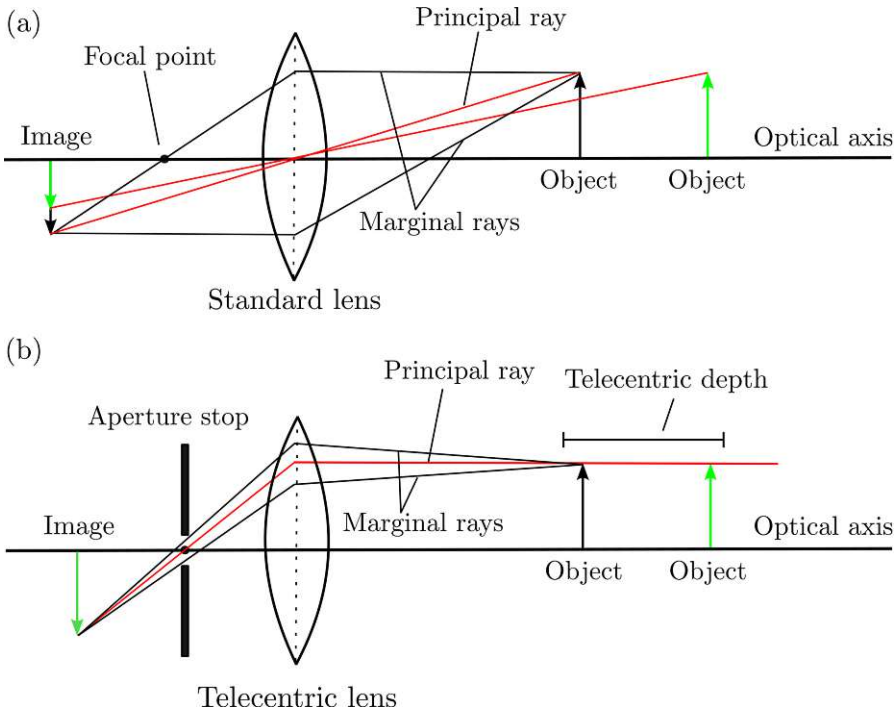

Figure 3.4: Schematic illustration of (a) standard and a (b) telecentric lens, showing the effect of out-of-plane movement. In a standard lens, the out-of-plane movement will result in the object appearing smaller or bigger in the image plane, where the magnification is constant for objects within the telecentric depth when a telecentric lens is used.

A standard lens refracts light from objects and focuses it at a single point called the focal point, where the principal ray (in red) is angled with respect to the optical axis in both the image and object space, as depicted in red in Figure 3.4(a). The principal rays define the angular field of view and travel through the centre of the aperture stop, while the marginal rays define the image position and travel through the edge of the aperture stop, limiting the amount of light able to pass through the lens. In these lenses, the magnification depends on the distance of the object from the lens and its position in the field of view. If the object moves out of the focal plane, it will appear smaller (in green) in the image plane, potentially resulting in pseudo strain measurements.

Unlike standard lenses, the principal ray (in red) on the object side is parallel to the optical axis in a telecentric lens, as depicted in red in Figure 3.4(b).

Because the aperture stop is moved to the focal plane of the lens, and the principal ray has to travel through the centre of the focal point in the middle of the aperture, it must be focused at infinity, meaning that black and green arrows appear at the same magnification regardless of their distance from the lens, because the field of view does not change. This constant magnification reduces errors caused by object movement or tilting on the surface. Sutton et al. [117] studied the effect of out-of-plane movement on strain analysis and concluded that strain errors can be reduced from 1250 µstrain per mm of out-of-plane motion to 25 µstrain per mm.

Speckle patterns. To use a DIC system to successfully track deformation, the surface of the material has to be sprayed with randomly distributed speckle patterns, ideally with a balanced white-to-black ratio of 50%. Speckle patterns can be applied using a black spray can or, preferably, professional airbrushes. The size of the patterns should be large enough to be resolved by the camera. Additionally, they should be small enough to be distinguished for evaluation. Researchers have found that the optimal size of the speckle pattern is 3-5 pixels. The surface pattern should not be reflective, as differences in brightness between the two cameras can prevent accurate computation in the areas affected by reflection. Figure 3.5 shows examples of different speckle patterns.

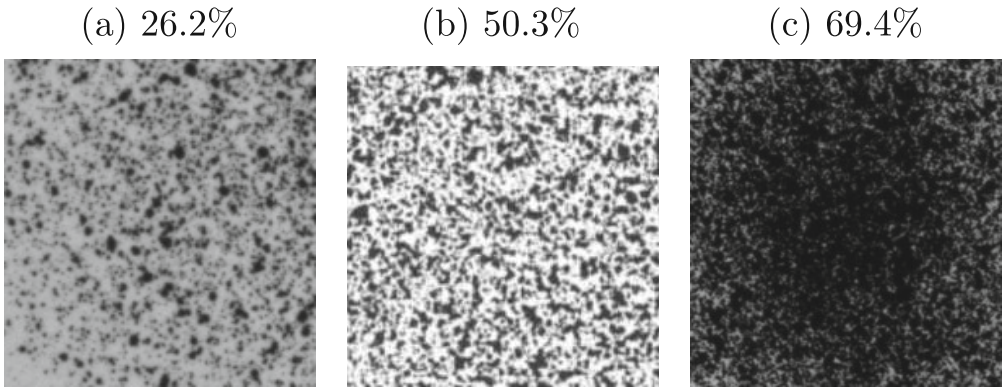

Figure 3.5: Speckle pattern size and distribution influence the accuracy of the DIC measurements. (a) Unsuitable low-contrast speckle pattern with small speckle size, (b) suitable-contrast speckle pattern, and (c) unsuitable low-contrast speckle pattern with large speckle size.

Speckle patterns help to allocate pixels in the camera images by dividing the surface into square areas known as facets. Facets are unique correlation areas,

usually ranging in size from 5 to 20 square pixels, and play a crucial role in the accuracy of DIC measurements. Facets, rather than individual pixels, are selected for tracking movement, as they contain varying grey levels that make them unique and distinguishable from other facets. A facet should contain at least three distinct speckle patterns (see Figure 3.6), and the centre of the facet serves as the measurement point. Larger facets may result in less accurate capture of local effects, while smaller facets offer finer detail but may require more computational resources. The step size determines the density of measurement points and the amount of overlap between adjacent facets. Smaller step sizes increase measurement point density but also prolong computational time, while larger step sizes reduce density but expedite processing.

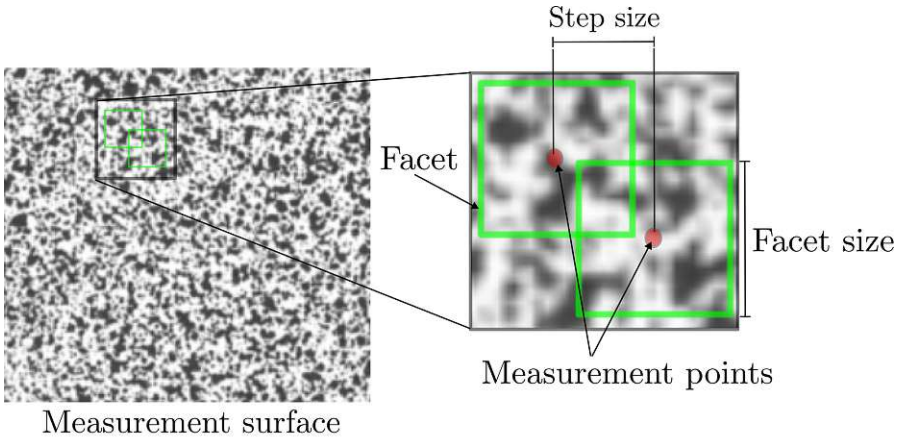

Figure 3.6: The measurement surface is divided into facets, and the centre of the facet is called a measurement point. The distance between two measurement point is known as the step size.

Prior to analysis, system calibration is required. This calibration process establishes an operational area (for 2D) or volume (for 3D) within which the centre point of the facets can be accurately measured. Calibration is achieved by moving a calibration object through a predefined range of motions within the designated area or volume where the measurements will occur.

Triangulation. In a 3D DIC system employing two cameras in a stereo configuration, the images captured by the left and right cameras are divided into facets, each characterized by unique pixel patterns. The centers of these facets

(i.e., the measurement points) are paired with each other, and the 3D coordinates of these measurement points can be obtained through triangulation [118]. This process requires calibration of the stereo cameras using image coordinates where the measurement points are known in both images.

Figure 3.7 explains the triangulation method, which is applied to determine the location of an unknown point $P(x, y, z)$ in space. The 2D coordinates of the measurement points in the left- and right-hand image are defined as $P_1(x_1, y_1)$ and $P_2(x_2, y_2)$. The coordinates (x, y, z) of the point P can be calculated as following:

$$z = \frac{f * B}{x_2 - x_1} \tag{3.3}$$

where B is the distance between the image planes of the two cameras, f is the focal length, and $x_2 - x_1$ is known as the disparity of the point P. After determining z, x and y can be calculated:

$$x = \frac{x_1 * z}{f} \quad \text{and} \quad y = \frac{y_1 * z}{f} \tag{3.4}$$

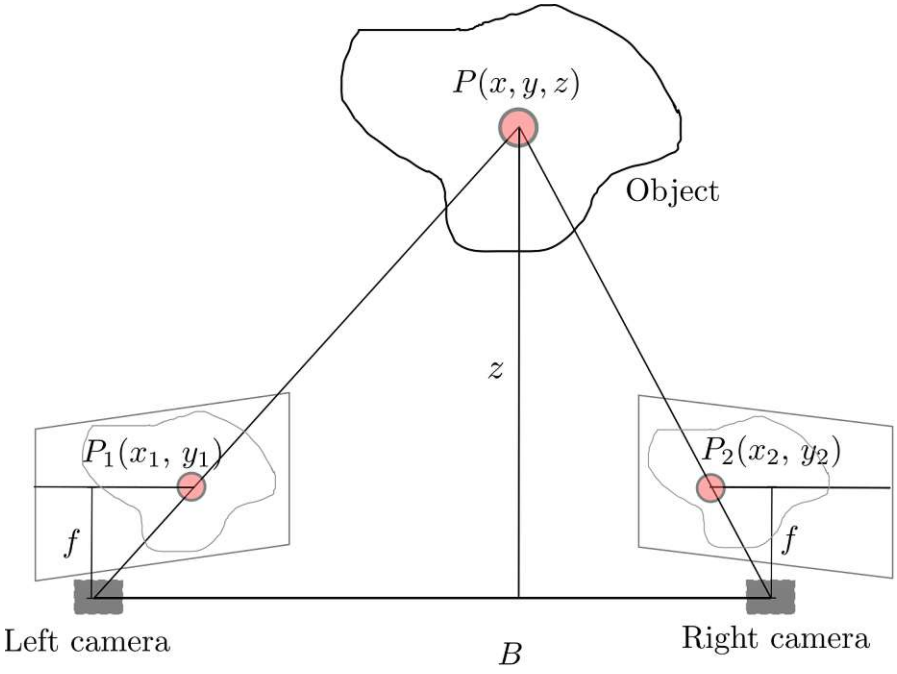

Figure 3.7: Stereo vision is a technique used to create a 3D description of a scene from two different viewpoints. The 3D coordinates of the point $P(x, y, z)$ can be determined if the focal length f, the distance between the image planes B, and the 2D coordinates of the measurement points in the left- and right-hand images are defined.

The stereo camera system has to be calibrated in order to successfully assign the measurement points using a calibration panel before the measurement is made. During the calibration of a 3D DIC system, the distance of the cameras, the angle of the cameras to each other, lens focus, and distortion are determined. The calibration panel has distinct reference points for which the 3D coordinates are calculated from the left- and right-hand cameras. These 3D coordinates for the reference points from the calibration panel are used to calculate the calibration deviation (intersection error), namely, by calculating their 2D coordinates in the left- and right-hand camera images. Correct calibration requires an intersection error between 0.01 and 0.04 pixels to be achieved. The average intersection error of all 3D points should not be larger than 0.1 pixel [119].

Correlation algorithm. The location of a reference facet of (n, m) dimension centred at point $P(x, y)$ in a reference image can be determined in the deformed

image (see Figure 3.8). Using a correlation algorithm, the degree of similarity between the facet in the reference and deformed images can be determined. The correlation criteria as found in the literature can be categorized into two groups, namely the cross-correlation (CC) and sum-squared difference (SSD), where the latter is simply defined as the Euclidean distance between two templates. Either way, the position of the facet in the deformed image is determined once a peak in the correlation coefficient distribution has been found. The cross-correlation and the sum-squared difference criteria can be determined as follows:

$$\mathrm{CC}(x,y) = \sum_{i=1}^{n}\sum_{j=1}^{m} f(x+i, y+j)S(i,j) \tag{3.5}$$

$$\mathrm{SDD}(x,y) = \sum_{i=1}^{n}\sum_{j=1}^{m} [f(x+i, y+j) - S(i,j)]^2 \tag{3.6}$$

where (n, m) are the dimensions of the facet S, and $f(x, y)$ is the reference image of dimensions $N \times M$.

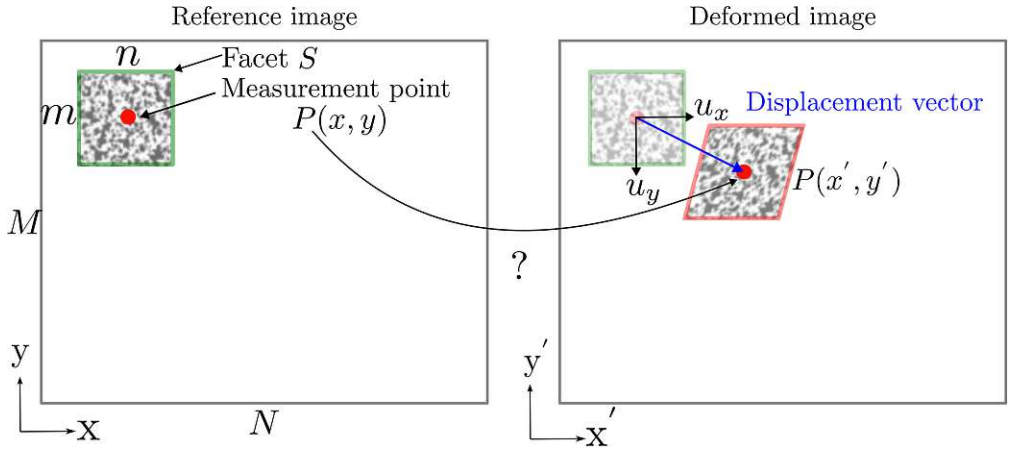

Figure 3.8: Illustration of a facet in the reference and deformed image in 2D. To determine the new location of a point $P(x, y)$, the facet S is compared between the reference and the deformed images using CC or SSD. The point P moves from its original location (x, y) in the reference image to a new location at (x', y') in the deformed image, this movement can be determined by the displacement u_x and u_y in $x-$ and $y-$directions, respectively.

If equation 3.6 is expanded, it becomes obvious that the term CC is included in the

SDD already. Both the CC and SSD correlation criteria are sensitive to lighting fluctuations, making them undesirable for determining the position of the facet in the deformed images. Therefore, the CC or the SSD equations are normalized to eliminate the influence of brightness and contrast. The normalized cross-correlation (NCC) equation can be written as:

$$\mathrm{NCC}(x,y) = \frac{\sum_{i=1}^{n}\sum_{j=1}^{m} f(x+i,y+j)S(i,j)}{\sqrt{\sum_{i=1}^{n}\sum_{j=1}^{m}[f(x+i,y+j)]^2}\sqrt{\sum_{i=1}^{n}\sum_{j=1}^{m}[S(i,j)]^2}} \tag{3.7}$$

Similarly, the normalized sum-of-squared-differences (NSSD) can be written as:

$$\mathrm{NSSD} = \sum_{i=1}^{n}\sum_{j=1}^{m}\left[\frac{f(x+i,y+j)}{\sqrt{\sum_{i=1}^{n}\sum_{j=1}^{m}[f(x+i,y+j)]^2}} - \frac{S(i,j)}{\sqrt{\sum_{i=1}^{n}\sum_{j=1}^{m}S(i,j)]^2}}\right]^2 \tag{3.8}$$

Both NCC or NSSD provide the corresponding maximum similarity for each facet or minimum grey value differences, respectively. They are insensitive to the linear scale in illumination lighting, but are sensitive to offsets in the lighting. This issue can be solved by subtracting the local mean (mean of search area) and mean of the facet, making NCC and NSSD more efficient. This modification of the NCC is called zero-normalized cross-correlation (ZNCC) and can be written as:

$$\mathrm{ZNCC}(x,y) = \frac{\sum_{i=1}^{n}\sum_{j=1}^{m}[f(x+i,y+j)-\bar{f}][S(i,j)-\bar{S}]}{\sqrt{\sum_{i=1}^{n}\sum_{j=1}^{m}[f(x+i,y+j)-\bar{f}]^2}\sqrt{\sum_{i=1}^{n}\sum_{j=1}^{m}[S(i,j)-\bar{S}]^2}} \tag{3.9}$$

where $\bar{f}$ is the mean of the image $f(x,y)$ or a subimage of dimension (n,m) and $\bar{S}$ is the mean of the facet. Similarly, the zero-normalized sum of squared differences (ZNSSD) can be written as:

$$\text{ZNSSD} = \sum_{i=1}^{n}\sum_{j=1}^{m}\left[\frac{f(x+i,y+j)-\bar{f}}{\sqrt{\sum_{i=1}^{n}\sum_{j=1}^{m}[f(x+i,y+j)-\bar{f}]^2}} - \frac{S(i,j)-\bar{S}}{\sqrt{\sum_{i=1}^{n}\sum_{j=1}^{m}[S(i,j)-\bar{S}]^2}}\right]^2 \tag{3.10}$$

ZNCC or ZNSSD correlation criteria are insensitive to the offset and linear scale in illumination lighting [120]; therefore, these are the most common methods used to determine the position of a facet in deformed images. The commercial DIC system used to compute the strain in the experiments conducted as part of this thesis work uses the normalized sum-of-squared-differences to find the minimum grey value differences between the facets in the deformed and reference images. Values of NCC and ZNCC vary between -1 and 1, i.e. the worst- and best-matching, respectively.

Displacement and strain computation. On an image of a test surface, patterns are recognized by projecting facets onto the image. Each facet is defined by its 2D or 3D coordinates and the distribution of gray-scale intensity within it. Following deformation, the pattern is re-recognized under the assumption that the gray-scale intensity distribution within the facet remains unchanged during deformation. Changes in the border coordinates surrounding each facet point are observed to analyze the alterations in the gray-scale intensity distribution. The 2D or 3D displacement gradient tensor field (∇u) is computed at every facet point based on these observations. The following equations explain how the deformation of a line element between the reference and the deformation stage is computed.

Figure 3.9 shows an image in the reference X and deformation x stage. The location of point P in the deformed stage x can be defined as the distance between the origin O and the point P, which can be computed as follows:

$$x + dX = X + dX + u(X + dX) \tag{3.11}$$

Here, $u(X)$ is the displacement vector function that relates the displacement of the

particle in the reference and deformed stages, defined as:

$$u(X) = x - X \tag{3.12}$$

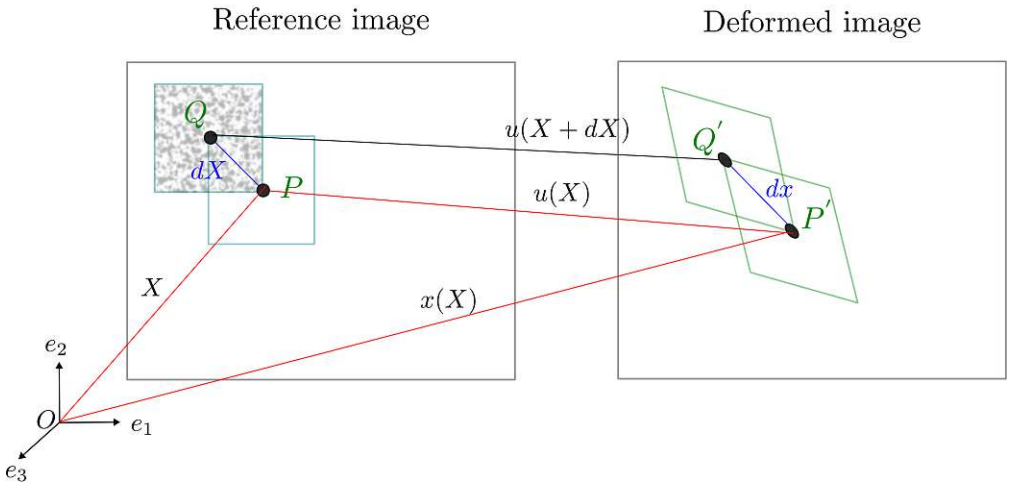

Figure 3.9: Illustration of a reference rectangular facet (in green) in the reference X and deformed x stages. The length between the two points P and Q is determined by dX and dx in the reference and deformed stages, respectively. The displacement function between P and $P^{'}$ is denoted by $u(X)$.

The above equation 3.12 can be rearranged to define the displacement in terms of the change in length of two points in the deformed stage, dx, as follows:

$$dx = dX + u(X + dX) - u(X) \tag{3.13}$$

The term $u(X + dX) - u(X)$ in the equation above is defined as the displacement gradient tensor field ∇u:

$$dx = dX + \nabla u dX \tag{3.14}$$

The displacement gradient tensor field ∇u is defined by the spatial derivatives of the displacement components with respect to the spatial coordinates:

$$\nabla u = \frac{\partial u_i}{\partial X_j} \tag{3.15}$$

The calculation of DIC strain essentially involves computing the derivative of displacement. The variation of subset measurement points in space can be expressed by the gradient matrix F, which represents the change in length between two points before and after deformation. This is formulated as follows:

$$F = \frac{dx}{dX} \tag{3.16}$$

The deformation gradient tensor F relates the reference and deformed states of a material. It's a tensor that characterizes how infinitesimal line elements change between these two states. F can be written in terms of the displacement gradient tensor field ∇u:

$$F = (I + \nabla u) \tag{3.17}$$

As strain is the change in length due to deformation, the relationship between dX and dx can be determined by dotting the equation $dx = FdX$ by itself:

$$dx.dx = FdX.FdX \Rightarrow ||dx||^2 = dX(F^{\mathrm{T}}F)dX \tag{3.18}$$

The difference between the squared magnitudes of the infinitesimal changes in the deformed and reference configurations.

$$||dx||^2 - ||dX||^2 = dX^{\mathrm{T}}(F^{\mathrm{T}}F - 1)dX \tag{3.19}$$

F^TF is known as the right Cauchy-Green tensor C, from which the Green strain tensor E_{G} can be determined, which characterizes the strain without accounting for rotations, equation 3.19 is divide by 2:

$$E_{\mathrm{G}} = \frac{1}{2}(F^{\mathrm{T}}F - I) \tag{3.20}$$

DIC algorithms usually use triangulation as a method to compute strain, where a set of constant strain triangles are defined, figure 3.10. The nodal coordinates and displacement of the triangles are used to derive the Green strain tensor. For a 2D displacement, the deformation gradient tensor F can be defined as a function of u and v which are the components of the displacement vector:

$$F = \begin{bmatrix} \frac{\partial x}{\partial X} & \frac{\partial x}{\partial Y} \\ \frac{\partial y}{\partial X} & \frac{\partial y}{\partial Y} \end{bmatrix} = I + \begin{bmatrix} \frac{\partial u}{\partial X} & \frac{\partial u}{\partial Y} \\ \frac{\partial v}{\partial X} & \frac{\partial v}{\partial Y} \end{bmatrix} \tag{3.21}$$

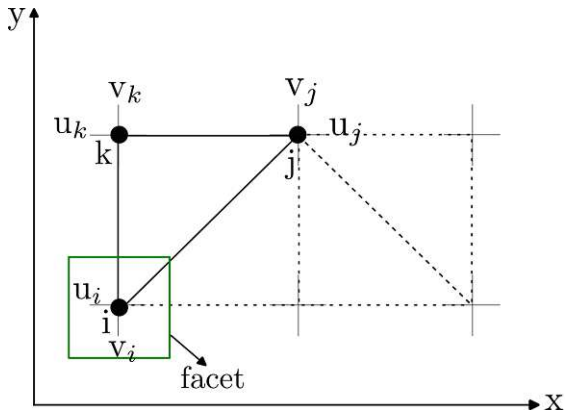

Figure 3.10: Representation of a constant strain triangular element in its undeformed state. The nodal coordinates are displaced by $u_{i,j,k}$ and $v_{i,j,k}$ along the $x-$ and $y-$direction.

After all facets were matched, and their new positions were known in all the deformed images, the displacements vectors (u, v) in $x-$ and $y-$directions can be obtained from the element shape functions N_i, N_j, N_k and the displacement components at each node, $u_{i,j,k}$, $v_{i,j,k}$:

$$\begin{bmatrix} u \\ v \end{bmatrix} = \begin{bmatrix} N_i u_i + N_j u_j + N_k u_k \\ N_i v_i + N_j v_j + N_k v_k \end{bmatrix} \tag{3.22}$$

The shape functions for every node can be determined by the following equations:

$$N_i = \frac{1}{2A}[x_i y_k - x_k y_j + (y_j - y_k)X + (x_k - x_j)Y] \tag{3.23}$$

$$N_j = \frac{1}{2A}[x_j y_i - x_i y_k + (y_k - y_i)X + (x_i - x_k)Y] \tag{3.24}$$

$$N_k = \frac{1}{2A}[x_i y_j - x_j y_i + (y_i - y_j)X + (x_j - x_i)Y] \tag{3.25}$$

where A is the area of the triangular element. From the displacements vectors u and v, the deformation gradient tensor F can be determined and the Green strain tensor E_{G} can be calculated as a function of the nodal coordinates and displacements.

The computation of displacement and strain relies on accurately determining the centre points of the facets (or measurement points) in both the right- and left-hand images (for 3D DIC), and subsequently, in the reference and deformed images. The precision of DIC in capturing local deformations influences the accurate localization of strain. Any inaccuracies or discrepancies in the facet allocation directly impact the measured displacements and strains. The size and spacing of the subsets play a crucial role in determining the accuracy of displacement measurements and the resultant strain values. Larger facets reduce noise in uniformly deformed regions but can smooth out strain gradients, making smaller facet sizes more suitable [121, 70, 18]. Despite DIC being widely used for strain measurement, particularly in cases of uniform displacement fields, it's necessary to assess its accuracy in capturing local non-uniform deformations. The following section provides an overview of the accuracy and precision of DIC in surface strain measurements.

3.2 Accuracy and precision of DIC strain measurements

This section discusses the accuracy and precision of DIC strain measurements with reference to factors influencing these parameters.

Accuracy and precision serve as distinct indicators of error. Accuracy refers to the closeness of a measured value to the true value, and precision relates to the consistency or reproducibility of repeated measurements. Strain measurement, like any measurement technique, is prone to noise which could lead to erroneous strain results. Strain gauges and extensometers are more accurate than DIC strain measurements since they are directly glued or attached to the sample [15]. Strain gauges or extensometers may yield inaccurate results when applied to small or delicate specimens, or when they mechanically interfere with the specimen [71]. In DIC measurements, various factors contribute to noise, including the size of the speckle pattern, which can be either too coarse or too fine [10, 122, 11, 123, 12], the camera resolution being non-optimal or not matching the measured surface, or wrongly selected facet or step sizes [70, 18, 124, 12]. The algorithm used to match facets between the deformed and reference images is critical for ensuring the accuracy of DIC measurements [1, 17, 125, 126, 127, 128]. Therefore, DIC systems must undergo optimization, and a thorough assessment of noise is necessary to evaluate the accuracy of the results. One method to evaluate DIC strain measurements involves comparing them with results from another measurement technique, such as strain gauges or extensometers. However, this approach is applicable only to homogeneous strain fields.

Accuracy can be defined as the difference in bias between the mean DIC strain measurement and the measurement obtained using strain gauges (or any other reference strain), while precision is represented by the standard deviation (random error) of the measurements. The quality of the image forms the foundation for accurate strain computation. The quality of the speckle pattern contributes to the image quality. Speckles should be stochastic, so that each facet is unique from its

neighbouring facets. Lecompte et al. [129] studied different speckle patterns and evaluated the displacement error. They found that using small speckles with a limited scatter of speckle sizes led to more accurate displacement computation, and that using larger facets resulted in a larger random error. The use of the airbrush has proved to be more accurate than the use of a spraying device, because the speckle sizes can be controlled by adjusting the paint and airflow [130, 70, 11]. The accuracy and precision associated with the speckle pattern can be readily assessed under zero-load conditions, where several images of the sample are captured without any applied load. Subsequently, displacement and strain values are computed [131]. Alternatively, accuracy can be assessed by numerically deforming the images and comparing the computed displacements against the numerically imposed displacement [129, 130, 132].

Other parameters that influence the accuracy and precision of DIC and that are also related to the speckle pattern, are the facet size and step size [120, 130, 15]. Larger facets reduce the number of measured points on a surface and hide strain gradients [13]. Smaller facets can increase the error radically if the speckle patterns are not optimal. An optimal speckle pattern size typically ranges from 3 to 5 pixels [1, 12]. The step size is the distance between two consecutive facets. "Smaller step sizes can increase the difficulty of locating facets between the deformed and reference images, leading to a higher likelihood of errors [15], and bigger step sizes result in fewer measurement points. The optimal ratio between facet and step size can be determined under zero-load conditions. By keeping the facet size fixed and varying the step size, the optimal parameter is identified as the one with the lowest pseudo-strain in a theoretically zero-strain field.

Another important factor that affects the accuracy of the strain measurement is whether a 3D or 2D DIC systems are used. Out-of-plane motion of the test specimen can occur in 2D DIC, in contrast to 3D DIC [117, 120]. Strain measurements are more sensitive to noise compared to displacements. The accuracy and precision of the displacement are on the order of 0.01 to 0.04 pixels [122]. Regarding strain, the reported accuracy in the literature varies between a few tens to hundreds of microstrains [23] and up to thousands of microstrains [15, 20].

Strain gauges outperform DIC in terms of accuracy for zero-strain readings, with readings smaller than 4 µstrain, compared to DIC where the noise for zero-strain readings is smaller than 10 µstrain [15]. The DIC strain measurements can be improved by improving the sample preparation, choosing suitable facet and step sizes, employing a high-resolution camera suitable for the target measurement, and applying suitable filtering parameters. In some cases, the DIC measurements outperform the strain gauges measurements; the accuracy of strain gauges suffers due to increased loading, particularly in cases of non-linear deformation or strain concentration in localized regions, such as on samples with complex geometries like the curvilinear surfaces of human femurs or vertebrae [23]. Strain gauges measurement can be inaccurate for soft materials, including bone, due to their contribution to the load-bearing capacity, leading to a systematic underestimation of the actual strain distribution [112]. DIC measurements on femoral samples were higher than the strain gauges measurements with an average difference of 83 µstrain, this is due to the attachment of the strain gauges to the femur, where bone is stiffened, and its deformation is restricted [109].

Regarding precision, the DIC method has some limitations, as mentioned earlier, where various factors can influence surface strain measurements, leading to peak values of up to 70 µstrain at zero-strain readings [15]. Furthermore, the precision of DIC did not deteriorate with increasing strain levels but remained at the same level of the zero-strain. Strain gauges exhibit higher precision because measurements can be repeated with low random error, a feature not guaranteed with DIC. This can be tested by repeatedly loading and reloading the same sample within the elastic limit for small strain levels. In contrast, DIC faces challenges when a sample is loaded and reloaded within the elastic limit, as the surface of the sample with speckle patterns deforms, making it difficult to reproduce the same results on the same sample. However, DIC can measure strain with relative accuracy in locations such as the femoral neck, where the average root-mean-square error and the standard deviation were 127 µstrain and 239 µstrain, respectively [87].

The evaluation of strain measurements on samples that exhibit strain gradients

or inhomogeneous strain fields is more challenging. This is because the true value of the strain cannot be easily verified with another measurement method. Due to limitations in camera resolution, residual noise is always present even when using optimized experimental setups. Various authors have investigated the accuracy and precision of DIC systems and suggested methods to reduce the noise, either by improving the sample preparation, measurement parameters, correlation algorithms or by filtering. Filters can be applied to the captured images [30, 31, 13] and/or the displacement fields [17, 32, 19, 33, 34, 35], or the computed strain fields [13, 133]. Filtering offers the possibility to reduce this noise. However, filters must be carefully chosen as they predominantly affect areas of strain gradients. In the next section, filtering strategies that can be applied to DIC measurements are explained.

3.3 Filtering approaches

Filtering has proved to be an effective method for reducing noise in DIC measurements. Filters vary in their degree of attenuation and whether they are applied locally or globally. However, filtering has a significant limitation when it comes to smoothing gradients, which is crucial for measuring linear gradients or inhomogeneous strain fields, such as those expected in bone. In the case of homogeneous deformation observed on the surface of engineering materials, where there are no changes in the specimen's dimensions, noise can be reduced by applying a simple average filter to the DIC field. In contrast, when dealing with inhomogeneous deformation, such as in irregular bone specimens with areas of high-strain gradients, average filters can be applied to smooth the gradient. Although a localized filter is preferred to minimize information loss, it often leads to noisier results [70]. Hence, finding an optimal filtering parameter capable of reducing noise in DIC strain fields, regardless of the applied load, strain window size, or strain field type, is essential.

In this section, an overview of the different types of filters applied to DIC strain measurements or DIC images is presented.

Simple mean filter. Mean or average filters are used to calculate the statistical

average of a filter mask. The mask is applied to each measurement point (or a pixel) in a measurement field (or image), and each measurement point is replaced with the average value of neighbouring measurement points in the mask, including the measurement point itself. The average filter is a built-in filter in the DIC commercial software, which is applied to the strain or displacement fields. Depending on how the DIC measurement points are organized in the field, the shape of the filter can vary. For the DIC data obtained in this thesis work, the DIC data are represented by a hexagonal grid, so the shape of the filter is also hexagonal. The points in the filter mask are usually weighted equally. Along the boundary, the strain points can be extrapolated by reflecting the boundary rows and columns, depending on the size of the filter. Figure 3.11 shows a filter $h(x, y)$ with size $s = 1$, where all points that are adjacent to the measurement point in a strain distribution $f(x, y)$ will be averaged together and saved in a new filtered strain distribution $g(x, y)$. The size of the filter can vary, and three sizes; s =1, 2, and 3 are shown in Figure 3.11.

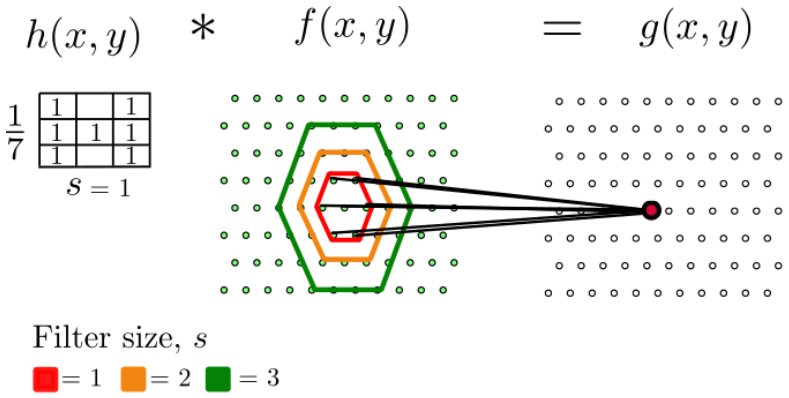

Figure 3.11: Simple mean filter $h(x, y)$ applied to a strain field $f(x, y)$ where the arrangement of the measurement points is a hexagonal grid. The filtered strain distribution is saved in $g(x, y)$. Figure adapted from [133].

If the size of the filter is large, the loss of information is even higher [134]. This filter results in a loss of information, especially when smoothing an image with impulsive noise. Sztefek et al. [58] applied three iterations of a 3 × 3 facet average filter to strain distribution across the surface of a mouse tibia loaded up to 12 N under compression. This filter smoothed the strain field and resulted in a reduction in the standard deviation of the error from 0.05% to 0.03% [58].

Gaussian mean filter in the spatial domain. In the spatial domain, like the mean filter, Gaussian mean filters replace the value of each measurement point in a field plane $f(x, y)$ with the mean value of its neighbours, including the point itself [135] (see Figure 3.12). The shape of the filter $h(x, y)$ weights the pixels based on their distance from the measured point.

$$h(x, y) = \frac{1}{2\pi\sigma^2} \exp^{-\frac{x^2+y^2}{2\sigma^2}} \tag{3.26}$$

where (x, y) are the coordinates of a measurement point in a 2D strain distribution, and σ is the standard deviation of a Gaussian function. The filtering is applied via convolution $g(x, y) = f(x, y) * h(x, y)$.

$$f(x, y) * h(x, y) = \frac{1}{MN} \sum_{m=0}^{M-1} \sum_{n=0}^{N-1} f(m, n)h(x - m, y - n) \tag{3.27}$$

where M and N are the dimensions of the image $f(x, y)$.

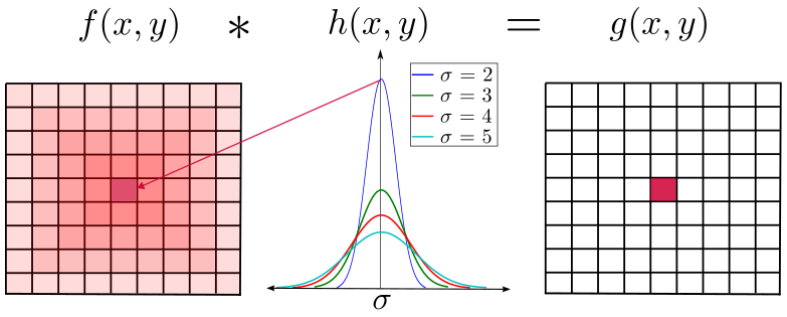

Figure 3.12: the Gaussian mean filter $h(x, y)$ weights the points based on their distance from the measured point, applied to a strain field $f(x, y)$. The filtered strain distribution is saved in $g(x, y)$. Figure adapted from [133].

For the attenuation of strain noise, Rajan et al. [18] applied Gaussian-weighted filtering to DIC strain measurements; however, the strain gradients were compromised. Schreier et al. [136] demonstrated that a 3×3 binomial filter is effective. In contrast, Zhou et al. [137] applied a pre-filtering step to the obtained images prior to the correlation, and the results show that the systematic error reduced

but the random error increased, especially for images with a speckle pattern that contained substantial high-frequency components.

Filtering in the frequency domain.

Filtering in the frequency domain is usually done by transforming a measurement point's distribution from the spatial domain (x, y) into the frequency domain (u, v). This transformation is done via discrete Fourier transform (DFT). High, low, or band frequencies can be filtered. The filtered distribution can be transformed back into the spatial domain with the inverse Fourier transform (IFT) method. The frequency in the Fourier transform can be associated with a pattern of variation intensity in a measurement field. At the origin of the transform, a low frequency corresponds to slowly varying components in an image. At a point further away from the origin of the transform, a higher frequency corresponds to faster and faster grey level changes in the images. High-frequency components are usually the edge of an object in an image, as well as abrupt changes in the grey level such as noise. Low-pass filters allow only low frequencies to pass through and attenuate high frequencies. They are known as smoothing filters as well. Conversely, high-pass filters allow only high frequencies to pass and attenuate low frequencies. They are known as sharpening filters, as the edges become more pronounced in the filtered image or field. Band reject filters attenuate frequencies within the range of a certain frequency and allow frequencies below a certain threshold and above another threshold to pass through. Bandpass filters only allow frequencies within a certain band to pass through and attenuate the frequencies below a threshold, and allow frequencies above another threshold to pass through. Since the noise in the DIC measurement field is represented by a high-frequency component [135, 13], low-pass filters are discussed in detail. More information about other filtering strategies can be found in [135].

The basic filtering steps used in the frequency domain are illustrated in Figure 3.13:

(a) The DIC measurement distribution $f(x, y)$ of $M \times N$ size is transformed from the spatial domain into the frequency domain, $F(u, v)$, using a discrete

Fourier transform (DFT) equation which is given by:

$$F(u,v) = \frac{1}{MN} \sum_{x=0}^{M-1} \sum_{y=0}^{N-1} f(x,y) \exp^{-j2\pi(\frac{ux}{M}+\frac{vy}{N})} \tag{3.28}$$

where u and v are the frequency variables, and x and y are the spatial variables. The Fourier amplitude spectrum or magnitude is given by:

$$F(u,v) = \sqrt{[R^2(u,v) + I^2(u,v)]} \tag{3.29}$$

where R and I are the real and imaginary parts of $F(u,v)$, respectively.

(b) Before the application of the filter, $f(x,y)$ is commonly multiplied by $(-1)^{x+y}$, to locate the low-frequency peaks at the centre of the $M \times N$ area, shifting the $F(u,v)$ to frequency coordinates $(M/2, N/2)$.

(c) A filter $H(u,v)$ with a certain cut-off frequency D_0 is multiplied by the centred spectrum $F(u,v)$. This multiplication is defined on an element-by-element basis.

$$G(u,v) = H(u,v) \cdot F(u,v) \tag{3.30}$$

(d) Using the inverse Fourier transform (IFT), $G(u,v)$ is transformed back into the spatial domain $g(x,y)$, and the real part of this inversion is shifted again by $(-1)^{x+y}$. The IFT is given by:

$$f(x,y) = \frac{1}{MN} \sum_{u=0}^{M-1} \sum_{v=0}^{N-1} F(u,v) \exp^{j2\pi(\frac{ux}{M}+\frac{vy}{N})} \tag{3.31}$$

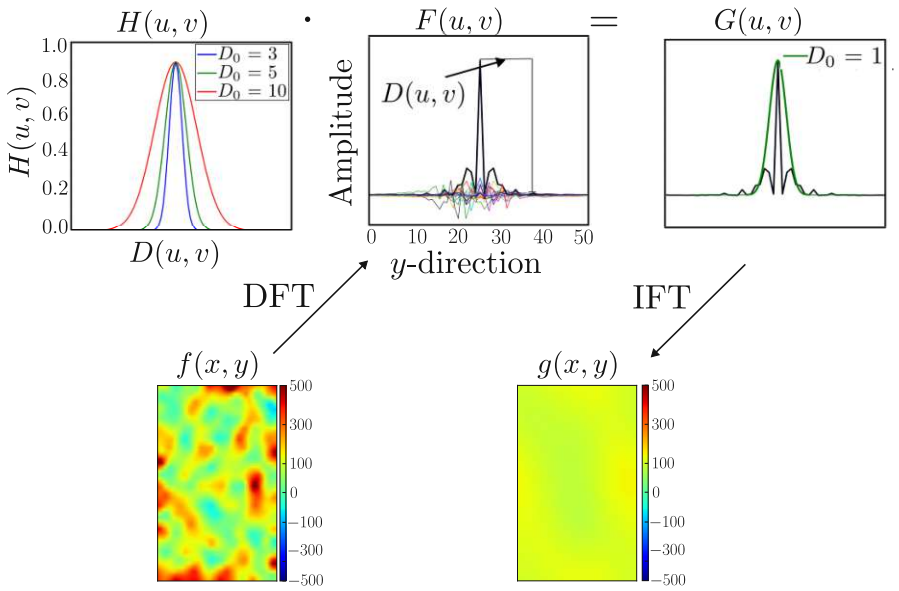

Figure 3.13: An illustration of a Gaussian low-pass filter where the measurement points are converted from the spatial domain $f(x, y)$ into the frequency domain $F(u, v)$. A low-pass filter $H(u, v)$ with a certain cut-off frequency D_0 is multiplied with the transformed measurement point $F(u, v)$ resulting in a filtered field in the frequency domain $G(u, v)$, which is finally inversely transformed into the spatial domain resulting in $g(x, y)$. In this thesis work, filtering was done on the measurement points, and the full-fields are shown for visualization purposes only. Figure adapted from [133].

Sharp transitions of grey values appear as high-frequency content in the Fourier transform, which usually comes from sharp edges or noise. Smoothing the high-frequency (sharp) features can be achieved by applying a low-pass filters. In this section, a brief overview of the low-pass (ideal, Butterworth and Gaussian) filters is given.

Butterworth LPF. Like the ideal LPF, this filter removes high-frequency noise from an image and preserves low-frequency components, but creates a smooth transition. The filter function $H(u, v)$ of order n is given by:

$$H(u,v) = \frac{1}{1 + \left[\frac{D(u,v)}{D_0}\right]^{2n}} \tag{3.32}$$

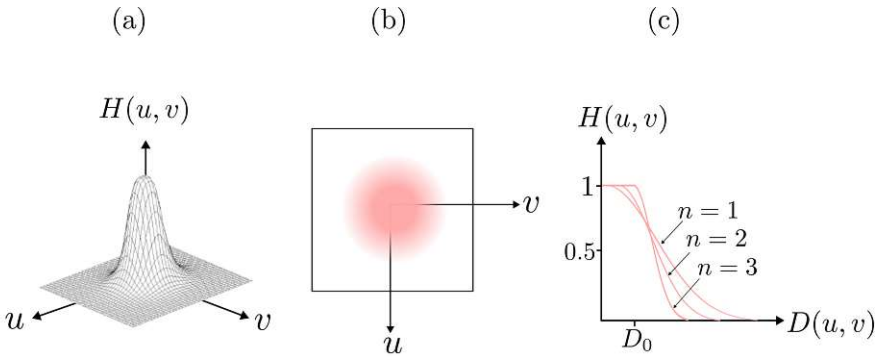

Figure 3.14: An illustration of a Butterworth LPF. (a) Perspective plot of a Butterworth LPF transfer function. (b) Filter displayed as an image. (c) Filter radial cross-section for different orders n. Figure adapted from Gonzales, 1992 [135].

Butterworth LPF does not have a sharp discontinuity. It smooths the transition in blurring as a function of increasing cut-ff frequency (see Figure 3.14). The function is reduced to 50% of its maximum value when $D(u, v) = D_0$. A Butterworth LPF of the order 1 or 2 does not suffer from ringing artefacts due to the smooth transition between the low and high frequencies; however, ringing can become an issue at higher orders [135]. As the order of the Butterworth LPF increases, it becomes closer to an ideal LPF, and thus takes on its characteristics.

Applying a Butterworth filter to DIC-captured images is recommended for error reduction due to its flexibility of pass-band selection and the maximal preservation of the allowed frequencies. It reduced the systematic error more efficiently than the Gaussian spatial filter when applied to the same images [137].

Gaussian LPF. The filter function $H(u, v)$ is defined by the following equation:

$$H(u, v) = \exp^{\frac{-D^2(u,v)}{2{D_0}^2}} \tag{3.33}$$

where, in this case, D_0 is the cut-off frequency of the filter that controls the shape of the Gaussian (see Figure 3.15) function. When $D(u, v) = D_0$, the filter is reduced to 0.667 of its maximum value. Like the Butterworth LPF, the Gaussian LPF has no ringing effect.

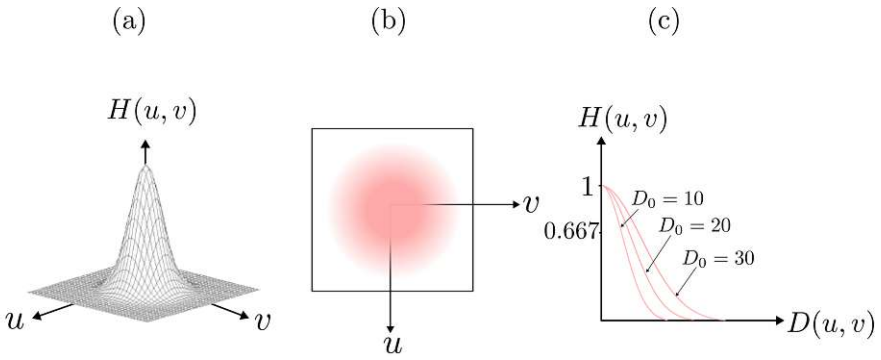

Figure 3.15: An illustration of a Gaussian LPF. (a) Perspective plot of a Gaussian LPF transfer function. (b) Filter displayed as an image. (c) Filter radial cross-section for different values of D_0. Figure adapted from Gonzales, 1992 [135].

Baldoni et al. [13] reduced the noise by 70% without excessive loss of information when a Gaussian low-pass filtering step was applied to the strain distributions. In contrast, applying a Gaussian LPF to the DIC captured images prior to displacement and strain calculation have proved to be ineffective. For high-frequency speckle patterns, Zhou et al. [137] applied a pre-filtering step to the images prior to the correlation, and the low-pass filters (binomial, Gaussian and Butterworth) slightly increased the random error, because the desired image gradients were attenuated. Likewise, Pan et al. [138] applied a 5×5 pixel Gaussian low-pass filter prior to correlation analysis to smooth the speckle images, which resulted in a reduction in the bias error in measured displacements. It is worth mentioning that filtering the DIC images prior to displacement and strain computation was found to be effective when the speckle patterns are well-defined in their shape, size and spacing [37].

Bandpass filter. This filter allows frequencies with certain range to pass through and attenuates all other frequencies. The benefit of this filter is that it can be used to denoise images and, at the same time, reduce low-frequency artefacts such an uneven illumination. Bandpass filters can be used to find image features such as blobs and edges. As in an ideal LPF, in an ideal bandpass filter, the frequencies within the given range are passed through without attenuation and frequencies outside the given range are completely removed (see Figure 3.16). With a Butterworth bandpass filter, frequencies at the centre of the frequency band are

unattenuated and frequencies at the edge of the band are attenuated by a fraction of the maximum value. As mentioned earlier, using the Butterworth filter does not result in sharp discontinuities between frequencies that are passed and filtered. The Gaussian bandpass filter function $H(u, v)$ is defined as:

$$H(u,v) = \exp^{\frac{-1}{2}\left[\frac{D^2(u,v)-D_0^2}{D(u,v)W}\right]^2} \tag{3.34}$$

where D_0 is the centre of the frequency band, and W is the width of the frequency band, $D = D(u, v)$ is the distance between a point (u, v) in the frequency domain and the centre of the frequency rectangle.

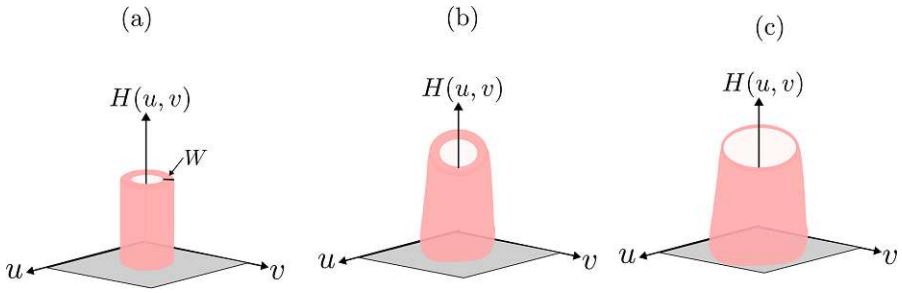

Figure 3.16: An illustration of (a) an ideal, (b) a Butterworth and (c) a Gaussian bandpass filter. Figure adapted from Gonzales, 1992 [135].

The opposite to a Gaussian bandpass filter is a Gaussian band reject filter, which can be given by:

$$H(u,v) = 1 - \exp^{\frac{-1}{2}\left[\frac{D^2(u,v)-D_0^2}{D(u,v)W}\right]^2} \tag{3.35}$$

One application of this filter in DIC is to eliminate the influence of the black-body radiation from high-temperature objects on the intensity of captured images, which is necessary to be able to compare the deformed DIC images at high temperature with the undeformed DIC image at room temperature. [139].

Gaussian notch filter. This filter is a special kind of band reject filter, it rejects only selective frequencies within a specified neighbourhood of a certain centre frequency. It is useful for filtering a specific noise and can be thought of as a

combination of LPF and HPF, where low and high frequencies both pass through, while one specific frequency is blocked. This filter can be applied to the DIC image, as it can effectively improve image quality due to its efficacy in removing periodic noise. To apply this filter, the coordinates of the centre of the area to be filtered (u_0, v_0) must be identified, and the filter function is defined as following:

$$H(u,v) = 1 - \exp^{\frac{-1}{2}\left[\frac{D_1(u,v)D_2(u,v)}{D_0^2}\right]} \tag{3.36}$$

where D_0 is the cut-off frequency of the Gaussian term, and D_1 and D_2 represent the distance from the centre of the spectrum of the points (u_0, v_0) or the width of the notch. If, $u_0 = v_0 = 1$ then, the notch-reject filter becomes a high-pass filter, and the notch-pass filter becomes a low-pass filter. Notch filters have been used to eliminate noise in DIC images, but the effect was counterintuitive as it increased the noise [13].

The next Chapter shows a systematic study exploring the possibility to find an optimal filtering parameter for simulated noisy constant strain fields, and linear and quadratic gradient strain fields.

CHAPTER 4

Optimal filtering parameters for noise reduction in DIC strain fields

4.1 Related publications and declaration of contributions

Results of the presented work (text, tables, figures) were *published* in the 'Journal of Applied Mechanics' in 2020, entitled 'Robust filtering options for higher-order strain fields generated by digital image correlation', and co-authored by A. Reisinger and D. H. Pahr.

Authors contribution The first author and the author of this thesis, *Nedaa Amraish*, wrote the manuscript, performed the experiments, data analysis and interpretation. *A. Reisinger* contributed to the methodology and reviewed the manuscript. *D. H. Pahr* supervised the work of Nedaa Amraish, contributed to the conceptualization, methodology, reviewed and edited the manuscript, and supported the interpretation of the results.

As mentioned in Chapter 3, filtering of the strain fields plays an important role in noise reduction, but it is a trade-off between losing information and removing noise. In this Chapter, a systematic study exploring the possibility to find an optimal filtering parameter for simulated noisy constant and gradient strain fields is presented.

4.2 Introduction

DIC was introduced as an alternative method for measuring strains in the 1980s [1]. It has the potential to measure surface strain optically by capturing images of the sample during deformation and thereby overcoming limitations such as attaching strain gauges to the sample or the size of measured area. For tracking the displacement on the surface of the sample using a DIC system, the surface of test samples has to be sprayed with random speckle patterns. The surface is divided into facets of pixels, each facet has unique pixel patterns, and the centres of these facets are known as measurement points. The displacement and strain are calculated for the measurement points of each facet between the deformed and non-deformed images [1, 140, 58].

Unlike strain gauges, DIC has advantages in measuring surface strains on samples with irregular shape and different sizes with a relatively easy sample preparation procedure, but the accuracy of strain gauges is one order of magnitude higher than that of DIC, especially for DIC systems with a moderate lens resolution or for testing on irregular geometries such as a whole bone tissue [23, 14, 15]. The root-mean-square error (RMSE), which is the square root of the mean of the square of all the error, for the strain gauge rosette (1 μstrain) was significantly different compared to DIC on vertebrae, where the error exceeded 25 μstrain [23]. In another study by Acciaioli et al., the intra- and inter-specimen repeatability of strain gauge measurements was 5 and 2.5 times better than DIC [15]. Nevertheless, for soft materials, strain gauges induce perturbation in the results due to their contribution to the load-bearing capacity, leading to a systematic underestimation of the actual strain distribution [112]. DIC has been used recently to measure strains on the

surface of engineered materials as well as biological tissues, however, DIC has limitations, because the results are influenced by different parameters that lead to unavoidable noise, and need optimization.

Previous work showed that noise in the calculated DIC strain fields is non-negligible if the measuring parameters were not optimized [10, 122, 70, 18, 124, 11, 123, 12]. Noise sources that can be controlled and optimized are related to the operator in the case of speckle patterns preparation, hardware parameters such as camera resolution, and software parameters such as the size of the strain window, facet and step size. Optimal parameters are not known a priori and can change according to the sample size, strain window and the expected strain concentration. Larger facets and strain window sizes reduce the noise for homogeneously deformed regions, whereas for inhomogeneous strain fields, the higher the strain gradients are, the smaller the optimal facet and strain window sizes [121, 70, 18]. Additionally, hardware parameters such as vibrations in the DIC system or in the testing machine can be reduced, but cannot be eliminated permanently. Even with optimized parameters, noise can still be present in the DIC strain and displacement fields and can become critical in regions with high stress concentration [32].

Numerous literature showed that the accuracy of a DIC algorithm depends on the way in which the algorithm is employed to identify the facets for the matching process between the deformed and non-deformed images. [1, 17, 126, 127, 128]. For displacement calculation, DIC algorithm can follow a local DIC approach, where the reference facet centred at each measurement point is traced along the deformed images, or a global DIC approach, where the position of all the measurement points are traced simultaneously [126, 127]. Most commercial DIC software follows a local DIC approach for displacement calculation, which is prone to more uncertainties in the displacement computation compared to a global DIC approach [126] for small facet size. Wang and Pan showed that local DIC outperforms its global counterpart when facet size is no less than 11 pixels [127]. Additionally, since the strain fields are derived quantities from the displacement, the noise in the original displacement measurements gets amplified in the strain fields, which in some cases, does not allow for accurate strain computation [16, 17, 18, 19], especially where measurement

errors are high in the case of discontinuous displacement fields [141, 32, 19].

Different approaches have been followed in the literature to filter the noise, either by filtering, the displacement fields [17, 32, 19, 33, 34] or the strain fields [13], or by filtering the DIC images prior to correlation computation [30, 31, 37, 13]. While all the above-mentioned filtering approaches are important, for practical reasons, this chapter is dedicated to data processing and noise filtering of strain fields computed by a commercial DIC system, without introducing other methods for strain computation.

Filtering of the strain fields plays an important role in noise reduction, but it is a trade-off between losing information and removing noise. Baldoni et al. explored different filtering strategies to reduce the noise, while minimizing the loss of information in the DIC strain fields. In the first strategy, they filtered DIC images using a median adaptive LPF and notch filters; these methods increased the noise rather than reducing it. In the second strategy, they applied a Gaussian LPF on a linear strain field. Only when an optimal cut-off frequency was selected for each stage—load level—the noise was reduced without excessive loss of information [13]. There are two limitations to this approach. First, the cut-off frequency changes for each stage, which means each captured strain field at each load level needs to be filtered with a different cut-off frequency. Ideally, an optimal cut-off frequency is advantageous; that is, independent of the load level, strain field size and the degree of strain concentration, which is explored in this chapter. Second, in their study, Baldoni et al. computed the residual noise as the root-mean-square error (RMSE) of the filtered DIC strain in the unstrained condition, however, we propose to compute the residual noise for each stage (load level) and not against the zero-load stage.

While the focus in the literature is on filtering the displacement field or improving the correlation algorithm, few studies focus on filtering the strain fields. This chapter follows a systematic approach to find optimal filter parameters for filtering strain fields exported directly from a commercial DIC software (ARAMIS v6.3.1; GOM, Braunschweig, Germany). The primary objective of this study is to show how the noise can be reduced for different strain window sizes (number

of measurement points) and strain field types (linear, quadratic, constant), using three practical filters (simple mean, Gaussian mean, Gaussian LPF) and how the total error changes when filter parameters change. The secondary objective is to apply the filter parameters—independent of the load level—on experimental data from a DIC system and to demonstrate the practical applicability of the theoretical findings.

4.3 Materials and methods

4.3.1 Simulated strain fields

In order to test the viability of the filtering options and to compute optimal filter parameters, three simulated strain fields were created, showing linear, quadratic, and constant strain changes. These fields were created for three different strain windows with measurement points of 6×5 (smallest, DIC systems require minimum 5–6 facets to calculate strain), 12×11 (extensometer gauge region), and 26×17 (typical for biological samples). Figure 4.1 shows these strain measurement points ${}^{\mathrm{Ref}}\varepsilon_i$ (a), the simulated strain fields ${}^{\mathrm{Ref}}\varepsilon_i$ without noise (b1, b2 and b3). The advantage of using simulated fields is that the values of the measurement points and the measurement random error are known, and one can evaluate the residual noise and the loss of information precisely. All three functions were created using Python SciPy and plotted with Scipy plt.image function. First, the coordinates' system (x, y) for a 2D plane was created and the strain fields are computed simply from the analytical function. Second, values were assigned (mapped) to the measurement points. For the constant field, the measurement points at the respected (x, y) were assigned with one single value. For the linear and quadratic fields, the values were assigned using a linear and a quadratic equation, respectively. Linear and quadratic fields are ranging from 0–1000 µstrain and the constant fields show a value of 500 µstrain which corresponds to the elastic regime of many engineering materials. Each of these simulated strain measurement points was subjected to a random noise with standard deviation of 300 µstrains. The standard deviation value of the noise was obtained from experimental findings, as described in Section 4.3.2. The

noise was imposed on the simulated fields using a Gaussian random generator in Python SciPy, since the noisy data points are typical—normally distributed—DIC outcome and are referred to as ${}^{\text{sDIC}}\varepsilon_i$ (s for simulated, ε for strain). For a better visualization, these data points were interpolated using Python SciPy to give the strain fields ${}^{\text{sDIC}}\varepsilon$, as shown in Figure 4.1c1–c3.

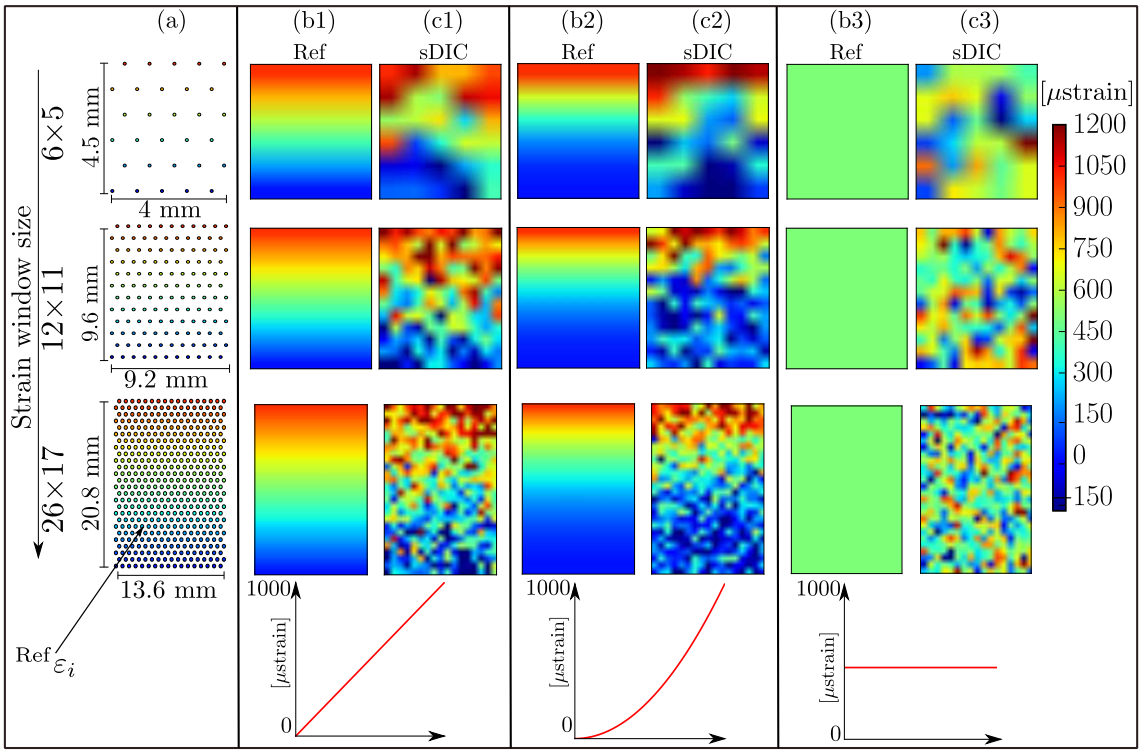

Figure 4.1: Simulated strain distribution: (**a**) Discrete strain distribution showing measured points at the facets centre for three strain windows with 6 × 5, 12 × 11 and 26 × 17 points which corresponds to a 4.5 × 4 mm^2, 9.6 × 9.2 mm^2, and 20.8 × 13.6 mm^2 area, respectively. (**b1**–**b3**) Two-dimensional representation of linear, quadratic and constant simulated strain fields respectively. (**c1**–**c3**) strain distributions with imposed Gaussian noise obtained from DIC measured data points.

4.3.2 Experimental strain fields

Ten steel samples (mild steel 1.0037) were prepared according to ASTM guidelines for metallic materials (E8) [142] for tensile tests, as in Figure 4.2. The Samples

were machined from a steel plate of 1 mm thickness using a numerically controlled machine (CNC Router BZT PFX 700, BZT Maschinenbau GmbH, Leopoldshöhe, Germany). Speckle patterns were applied to the steel samples' surface using a high precision airbrush (Profi-AirBrush, Wiesbaden, Germany). The airbrush settings were adjusted (air pressure of 200 kPa, 3 turns of the airbrush opening, and 9 cm distance between the airbrush and the sample) to obtain a speckle size of 3–5 pixels [10] with a random distribution (coverage 45–50%). The samples were mounted on a Zwick (Z030) machine (ZwickRoell GmbH, Ulm, Germany). ARAMIS 3D commercial system (ARAMIS 150/6M/Rev.02, GOM GmbH, Braunschweig, Germany) was set up with two CCD cameras. The cameras were positioned perpendicular to the sample at 35 cm distance, see Figure 4.3a. A universal extensometer (ZwickRoell GmbH, Germany) was attached to the samples in the gauge region (25 mm in length), from which the uniaxial global strain was obtained.

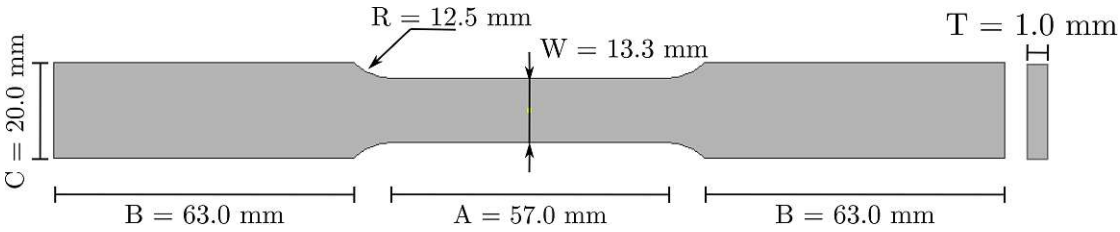

Figure 4.2: Detailed dimensions of an ASTM flat steel sample.

The noise-floor of the DIC measurement was evaluated by capturing 10 images of each sample, at 1 Hz and 8 ms exposure time, while the sample was mounted on the testing machine without any load applied (zero-strain). The strain window corresponding to the measurement area between the extensometer has 12×11 measurement points for a facet size of 19×19 pixels with a facet step of 16 pixels (50% overlapping); these parameters are recommended by ARAMIS for 6 Megapixel CCD cameras [119], see Figure 4.3b in red as the region of interest (ROI). This pre-test was used to obtain reasonable noise levels for the simulated noise. The maximum noise at zero-load was less than 800 µstrain, the average noise ranged from 140–210 µstrain and the standard deviation ranged from 200–270 µstrain for the 10 captured images (a value of 300 µstrain was taken as a worst case scenario and imposed on the simulated strain fields). The histograms of the strain measured were similar to Figure 4.3c. Finally, the steel samples were subjected to a uniaxial tensile

load along the vertical direction with cross-head movement of 5 mm.min^{-1} until fracture. A universal extensometer (ZwickRoell GmbH, Germany) was attached to the samples in the gauge region (25 mm in length), from which the uniaxial global strain was obtained and referred to as reference strain ($^{\text{Ref}}\varepsilon_i$). The strain fields were subsequently exported from the ARAMIS Professional software (ARAMIS v6.3.1; GOM) as .csv file containing the node number, $x-$, $y-$, $z-$coordinates, and the measured strain values for plotting and post-processing with Python SciPy.

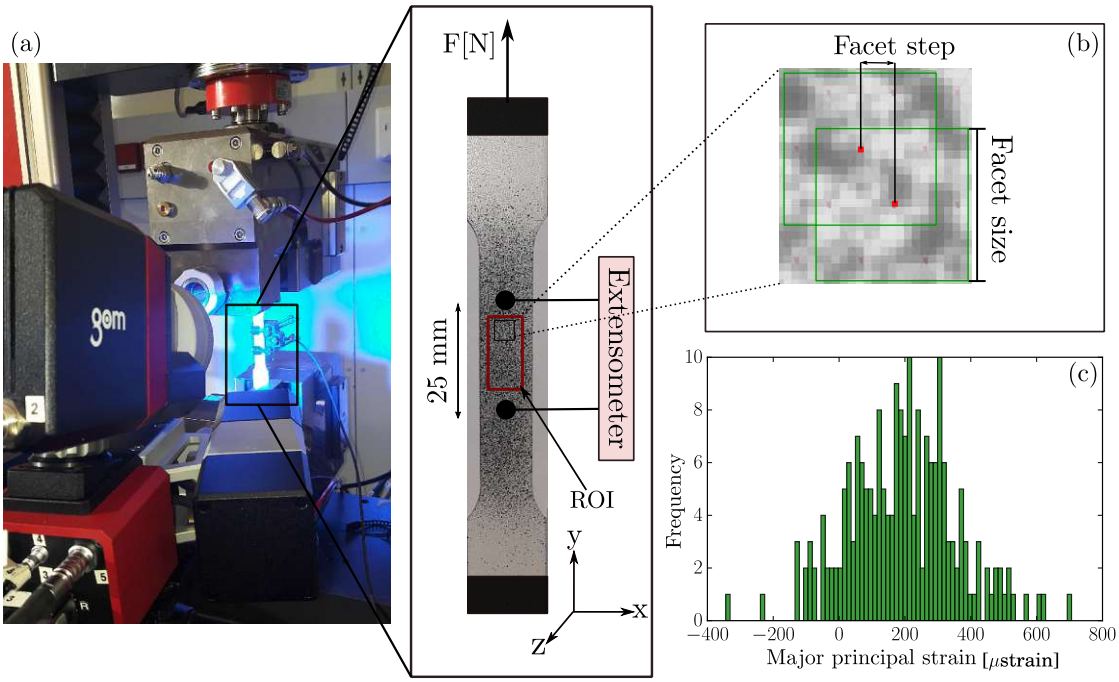

Figure 4.3: (**a**) Tensile test setup. Steel samples were mounted on Z030 machine, an extensometer was attached to the sample and ARAMIS DIC system was capturing images of the test. ROI is the region of interest for DIC measurement points. (**b**) Facets and grid sizes. (**c**) Histogram of a strain field distribution at zero-strain for a facet size of 19 × 19 pixels and a facet step of 16 pixels.

4.4 Filtering approach

Filtering approaches were explained in detailed in section 3.3. Here a brief review of the three filters applied in this chapter is presented. In order to find an optimal

filtering parameter that can reduce the noise in the DIC strain fields regardless of the load applied or the size of the strain window, a systematic approach was followed. In this approach, three filters and three strain window sizes were selected. This approach was applied to three simulated strain fields showing constant, linear and quadratic strain fields. More details on the different strain fields and windows can be found in section 4.3.1.

The three filtering approaches that were applied to the strain fields are (1) simple mean filter which is also used in the DIC commercial software (ARAMIS v6.3.1; GOM), (2) Gaussian mean filter in the spatial domain, which is used in Python SciPy. (3) A self-written script that implements Gaussian LPF in the frequency domain. In the following section, the difference between these filters is explained, as depicted in Figure 4.4. All three filters are in-house implementations.

The three filters have a similar working principle since the simple mean and Gaussian mean filtering perform convolution in the spatial domain and differ only in two aspects; (a) the shape of the filter is ideal or Gaussian distributed, and (b) the shape of the kernel (hexagonal or square). Gaussian mean and Gaussian LPF are well alike, since convolution in the spatial domain is equivalent to multiplication in the frequency domain and vice versa [135]. Despite the similar working principle of these filters, differences in the results are observed.

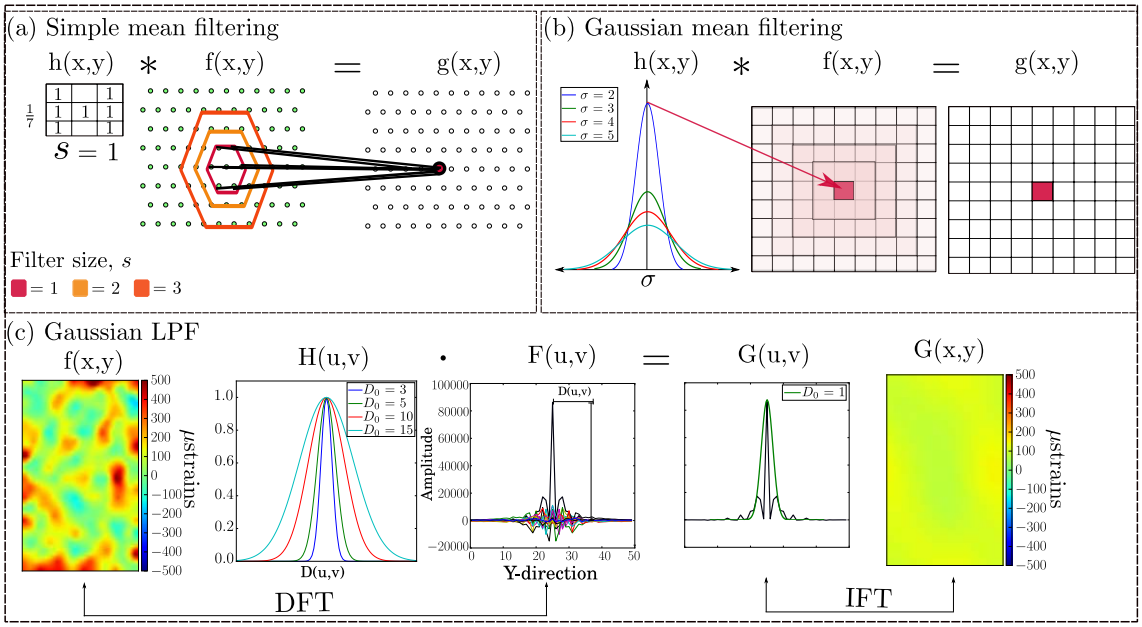

Figure 4.4: Overview of the three filter approaches. (**a**) Simple mean filter, all measurement points at a specific distance are averaged together. (**b**) Gaussian mean filter, each measurement point is replaced with the mean value of its neighbours. (**c**) Gaussian low-pass filtering (LPF), by converting the measurement points into the frequency domain, an LPF can reduce the noise by eliminating high-frequency components. Filtering is done on the measurement points, and fields are shown for visualization purposes only.

4.4.1 Simple mean filter

This filter follows the implementation of an ARAMIS average filter and is implemented in Python 2.7. According to ARAMIS/GOM guidelines [128], if the size (s) of the filter $h(x, y)$ is 1, all points that are adjacent to the measurement point in a strain distribution $f(x, y)$ will be averaged together and saved in a new filtered strain distribution $g(x, y)$, see Figure 4.4a for $s = 1, 2, 3$. Since DIC data are represented by a hexagonal grid, the shape of the filter is also hexagonal, and all points are weighted equally. At the boundary, the strain points were extrapolated by reflecting the last three rows and columns.

4.4.2 Gaussian mean filter in the spatial domain

Gaussian mean filtering replaces the value of each pixel in an image plane $f(x, y)$ with the mean value of its neighbours, including the pixel itself [135], see Figure 4.4b. The shape of the filter $h(x, y)$ weighs the pixels based on their distance to the measured point.

$$h(x, y) = \frac{1}{2\pi\sigma^2} \exp^{-\frac{x^2+y^2}{2\sigma^2}} \tag{4.1}$$

where (x, y) are the coordinates of a measurement point in a 2D strain distribution, and σ is the standard deviation of a Gaussian function. The filtering is applied via convolution $g(x, y) = h(x, y) * f(x, y)$. During optimization, a Gaussian mean filter was applied with $\sigma =$ 0.1 to 10 with 0.1 increments using a built-in function in Python.

4.4.3 Gaussian LPF in the frequency domain

Filtering in the frequency domain is recommended since the noise is represented by a high-frequency component [13]. In this study, a Gaussian LPF [135], $H(u, v)$, was applied:

$$H(u, v) = \exp^{-\frac{D^2_{(u,v)}}{2{D_0}^2}} \tag{4.2}$$

where $D_{(u,v)}$ is the distance of the point (u, v) from the centre of the spectrum, and D_0 is the cut-off frequency of the filter that controls the shape of the Gaussian.

4.5 Error reduction of full-field strain evaluation

The filtering efficiency is measured by two terms of error; the loss of information and the residual noise. The loss of information is the amount of true signal lost when the reference strains at measurement points (${}^{\mathrm{Ref}}\varepsilon_i$) were filtered (${}^{\mathrm{Ref}'}\varepsilon_i$) Equation (4.3). The residual noise is the distance between each reference point (${}^{\mathrm{Ref}}\varepsilon_i$) and filtered noisy point (${}^{\mathrm{sDIC}'}\varepsilon_i$) for each stage (see Equation (4.4) and Figure 4.5). The total error is the square-root of the sum of the quadratic of both

error terms, Equation (4.5) [13]. The reference strain is either null in the case of zero-strain or the simulated strain field without noise imposed, or is the global strain determined from the extensometer in case of the loaded steel samples. The error was calculated as the RMSE with the following equations.

$$\mathrm{RMSE}_{\text{loss of info}} = \sqrt{\frac{1}{n}\Sigma_{i=1}^{n}\left({}^{\mathrm{Ref}}\varepsilon_i - {}^{\mathrm{Ref'}}\varepsilon_i\right)^2} \tag{4.3}$$

$$\mathrm{RMSE}_{\text{residual noise}} = \sqrt{\frac{1}{n}\Sigma_{i=1}^{n}\left({}^{\mathrm{Ref}}\varepsilon_i - {}^{\mathrm{sDIC'}}\varepsilon_i\right)^2} \tag{4.4}$$

$$\text{Total error} = \sqrt{\mathrm{RMSE}^2_{\text{loss of info}} + \mathrm{RMSE}^2_{\text{residual noise}}} \tag{4.5}$$

where n is the number of local strain measurement points (i), e.g., computed by ARAMIS, ${}^{\mathrm{Ref}}\varepsilon_i$ is the value of the reference strain, ${}^{\mathrm{Ref'}}\varepsilon_i$ is the value of the filtered reference strain, and ${}^{\mathrm{sDIC'}}\varepsilon_i$ is the value of the filtered noisy point. Smaller RMSE means better denoising. The error reduction is described by how good the noise elimination is and was calculated as following:

$$\text{Error reduction} = \frac{\text{Imposed noise} - \text{Total error}}{\text{Imposed noise}} \times 100\% \tag{4.6}$$

where the imposed noise is 300 μstrains for simulated cases. Ideally, the total error is zero and the error reduction is at its maximum. The error reduction increases with decreasing total error.

The optimal specific filter parameters s^*, σ^*, D_0^* were found as the filter parameter that had the minimum total error for each strain window size. The overall optimal filter parameters $\bar{s^*}, \bar{\sigma^*}, \bar{D_0^*}$ were calculated as the mean of the optimal specific filter values s^*, σ^*, D_0^* from the linear and quadratic fields, as per the following equation:

$$\bar{\sigma^*} = \frac{\Sigma_{j=1}^{3}{}^{\mathrm{linear}}\sigma^* + \Sigma_{j=1}^{3}{}^{\mathrm{quadratic}}\sigma^*}{6} \tag{4.7}$$

where j is the number of strain windows. Parameters obtained from constant strain fields are neglected because finding an optimal filter in such cases is not meaningful

for higher-order strain fields.

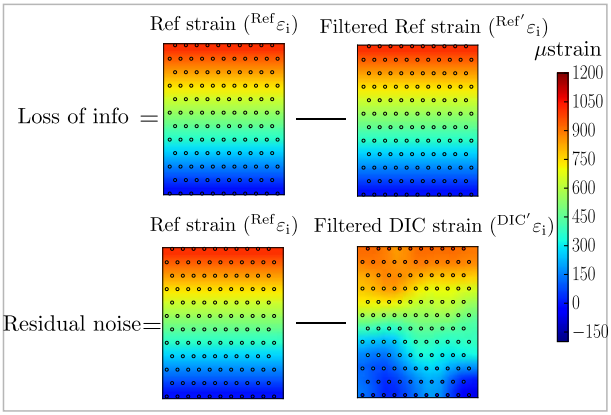

Figure 4.5: Overview of the RMSE calculations. Fields are only shown for visualization; calculations are done by using the measurement points. The loss of information is defined as the difference between the reference field and the filtered reference field (top row). The residual noise is defined as the difference between the reference field and the filtered noisy field.

4.6 Results

4.6.1 Simulated strain fields

Figures 4.6–4.8 show the influence of filtering on the loss of information, residual noise and total error, respectively. The loss of information increases with changing the filter size for both the simple means and the Gauss mean filtering, while it decreases for Gauss LPF, as depicted in Figure 4.6c,c1. The residual noise increases for the simple mean filtering for the smallest window size, and it increases sharply for Gauss mean filtering and mildly for Gauss LPF, as depicted in Figure 4.7b–c1. The optimal filtering parameters were found based on the total error curve, as depicted in Figure 4.8; the opaque pink bar shows the range of the optimal filtering parameters, which was determined where the total error had a minimum for each strain window and field type. Figure 4.9 shows the corresponding linear and quadratic strain fields with the specific filtering parameters for each strain

window and the overall optimal filtering parameter.

The simple mean filter shows a considerable influence of the size s for different strain window sizes and types (Figure 4.8a,a1). Graphically, this is also visible in Figure 4.9a. A good compromise is found with $\bar{s}^* = 2$, with an error reduction of 38, 69 and 73% for linear fields and 32, 66 and 74% for the quadratic fields for the different sizes of the strain windows.

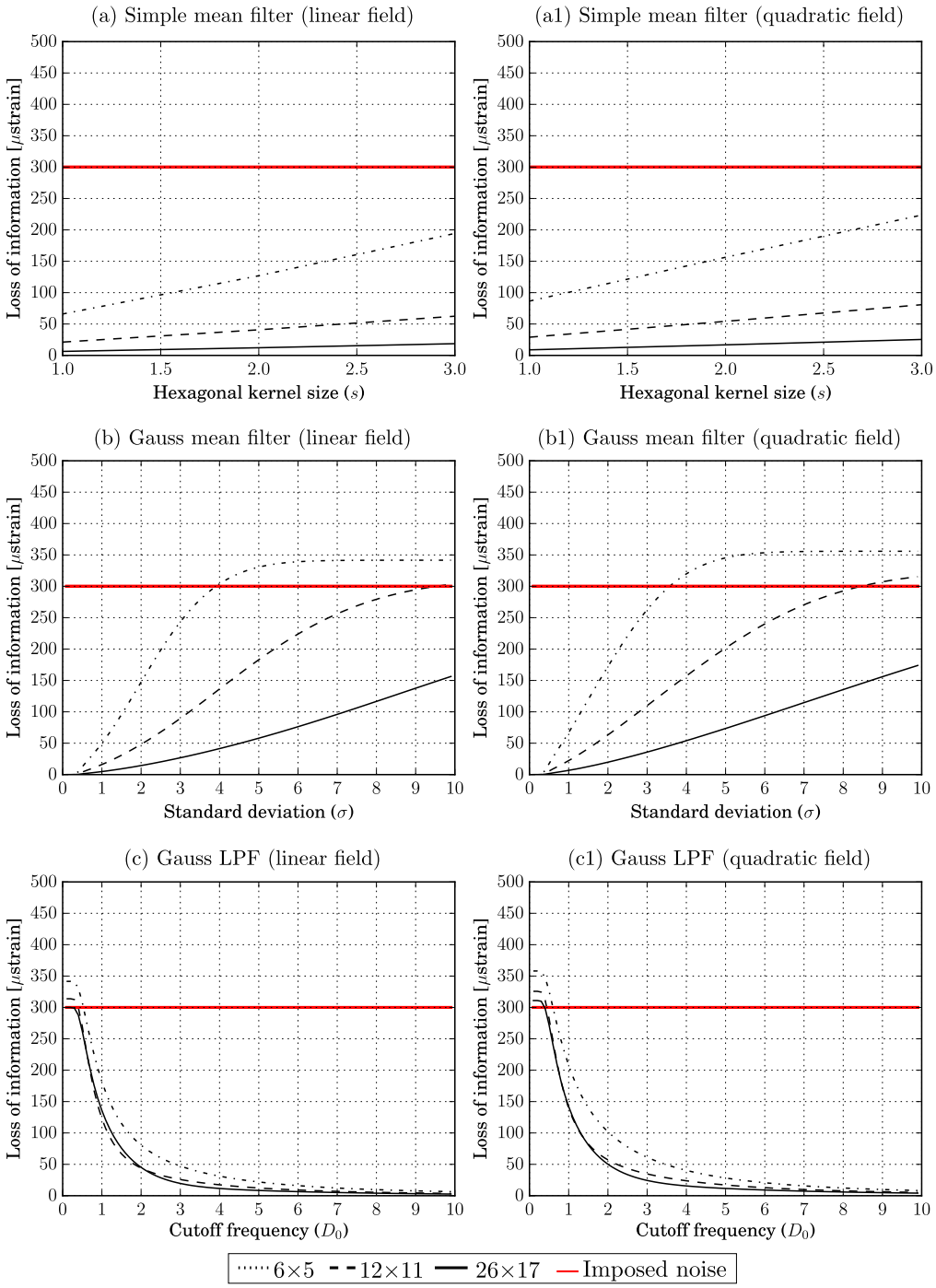

Figure 4.6: Curves of loss of information for different strain window sizes for linear and quadratic strain fields. The unit of the kernel size (s), standard deviation (σ), and cut-off frequency (D_0) is measurement points.

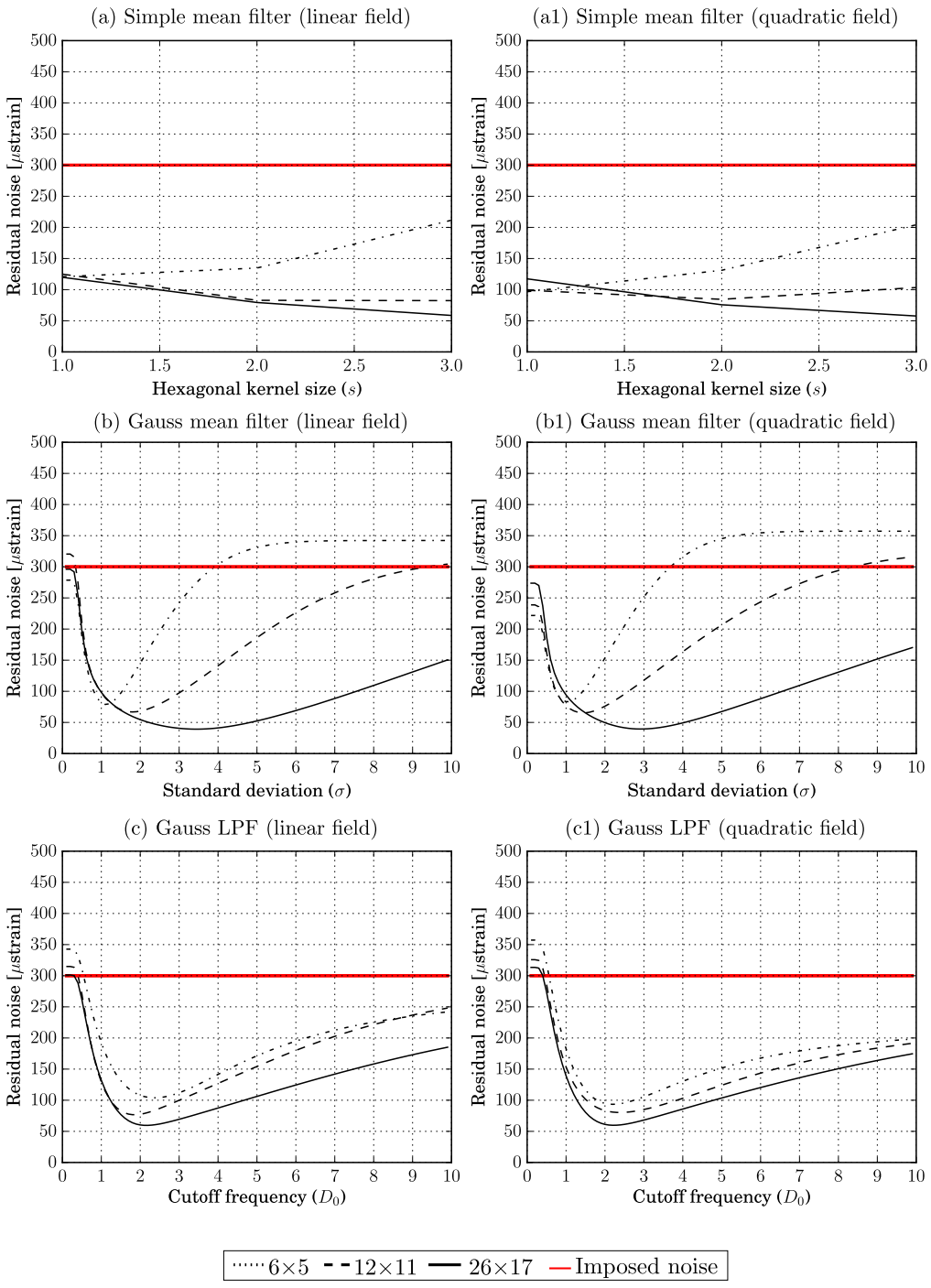

Figure 4.7: Curves of residual noise for different strain window sizes for linear and quadratic strain fields. The unit of the kernel size (s), standard deviation (σ), and cut-off frequency (D_0) is measurement points.

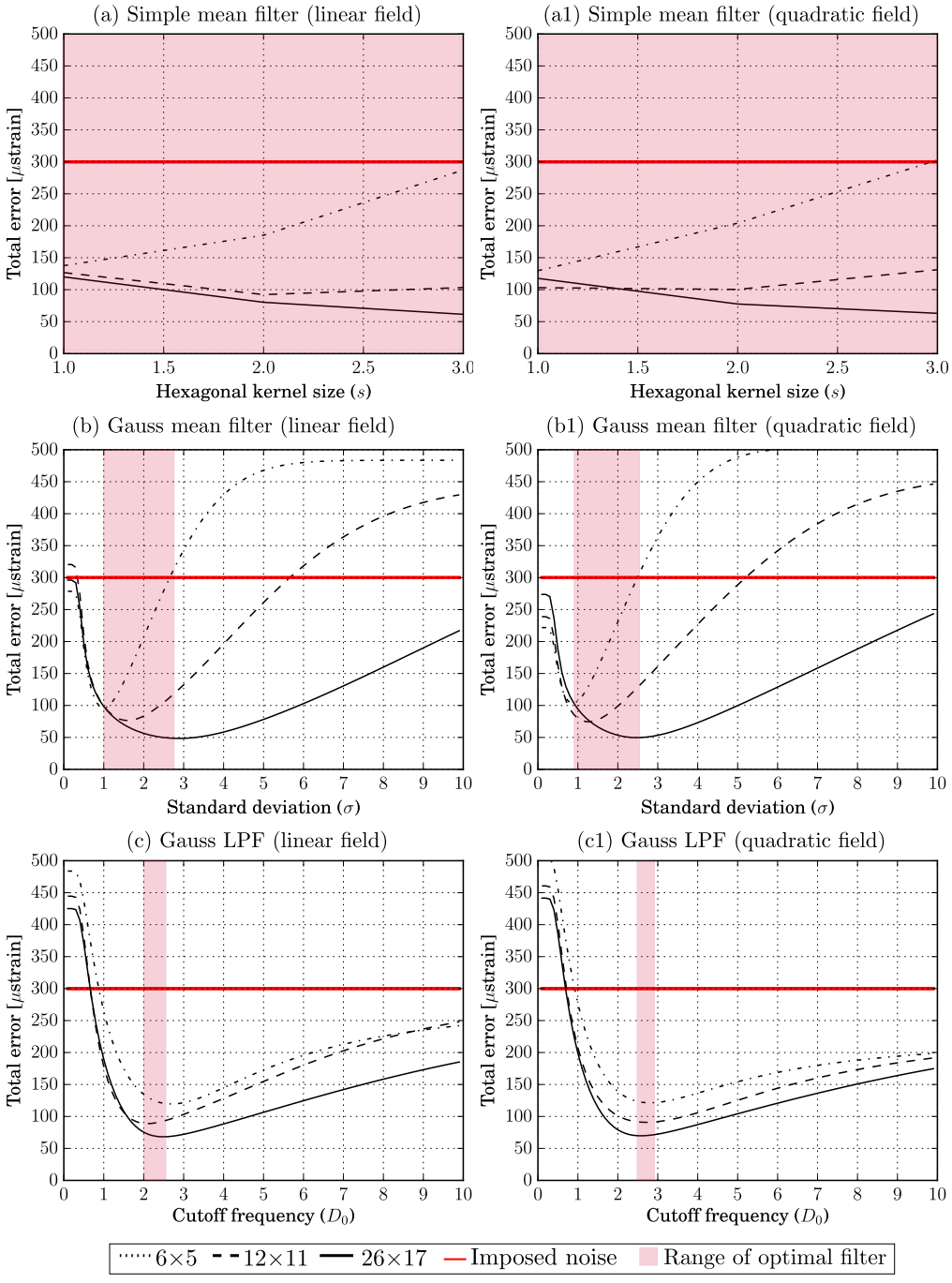

Figure 4.8: Curves of total error for different strain window sizes for linear and quadratic strain fields. The opaque pink bar shows the range of the optimal filtering parameters.The unit of the kernel size (s), standard deviation (σ), and cut-off frequency (D_0) is measurement points.

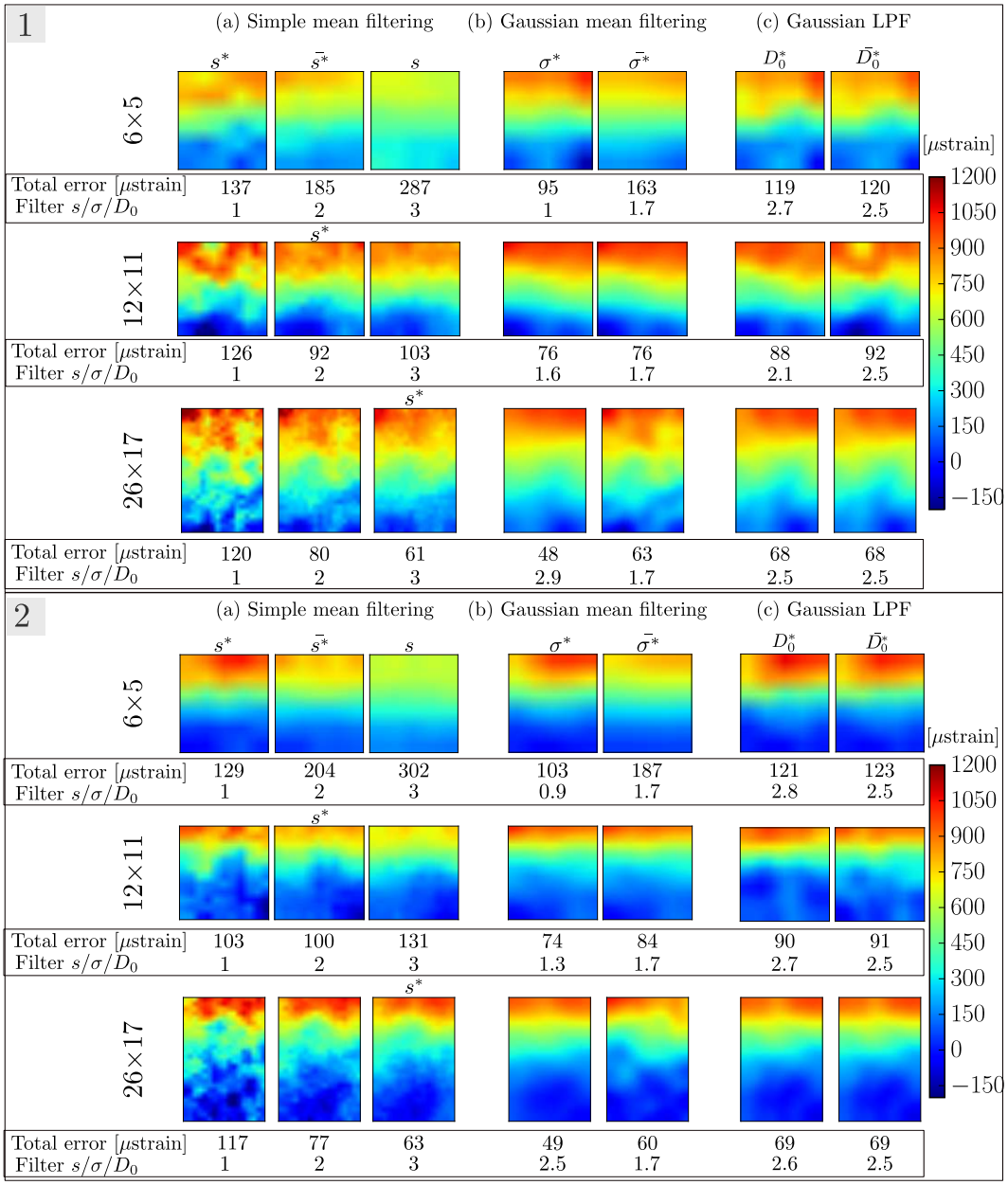

Figure 4.9: Two-dimensional visualization of (1) linear and (2) quadratic strain fields (**a**) Simple mean filter for $s = 1$, 2, and 3, (**b**) Gaussian mean filter with σ^* for each strain window and $\bar{\sigma}^* = 1.7$, (**c**) Gaussian LPF with D_0^* for each strain window and $\bar{D_0}^* = 2.5$.

The range of the specific filter parameter σ^* for Gaussian mean filtering was from 1 to 2.9 for the linear fields and from 0.9 to 2.5 for the quadratic fields as

depicted in Figure 4.8b,b1 with overall filtering parameter $\bar{\sigma}^* = 1.7$. The corresponding strain fields (Figure 4.9b), for σ^* and $\bar{\sigma}^*$ show less error compared to simple mean filtering and Gaussian LPF, except for the 6×5 quadratic field when $\bar{\sigma}^* = 1.7$ was applied. Applying $\bar{\sigma}^* = 1.7$, Gaussian mean filtering reconstructed the linear fields with error reduction of 45, 74 and 79%, and the quadratic fields with error reduction of 37, 72 and 80% for the different sizes of the strain windows.

Gaussian LPF had D_0 between 2.1 and 2.7 for linear fields and between 2.6 and 2.8 for the quadratic fields; see Figure 4.8c,c1 with overall filtering parameter $\bar{D}_0^* = 2.5$. Applying $\bar{D}_0^* = 2.5$, Gaussian LPF reconstructed the linear fields with error reduction of 60%, 69% and 77%, and the quadratic fields with error reduction of 59%, 69% and 77% for the different sizes of the strain windows. Figure 4.9 shows a 2D visualization of the filtered strain fields.

The application of $\bar{s}^* = 2$, $\bar{\sigma}^* = 1.7$, and $\bar{D}_0^* = 2.5$ to the constant simulated strain fields are summarized in Figure 4.10, where the error reduction for different strain window sizes is shown. Regardless of the size of the strain windows, Gaussian mean filtering performs best (error reduction 73–81%) whereas for a window size of 6×5 and 12×11, Gaussian LPF performs at least with error reduction of 55%. For a window size of 26×17, all filters achieved a similar level of error reduction.

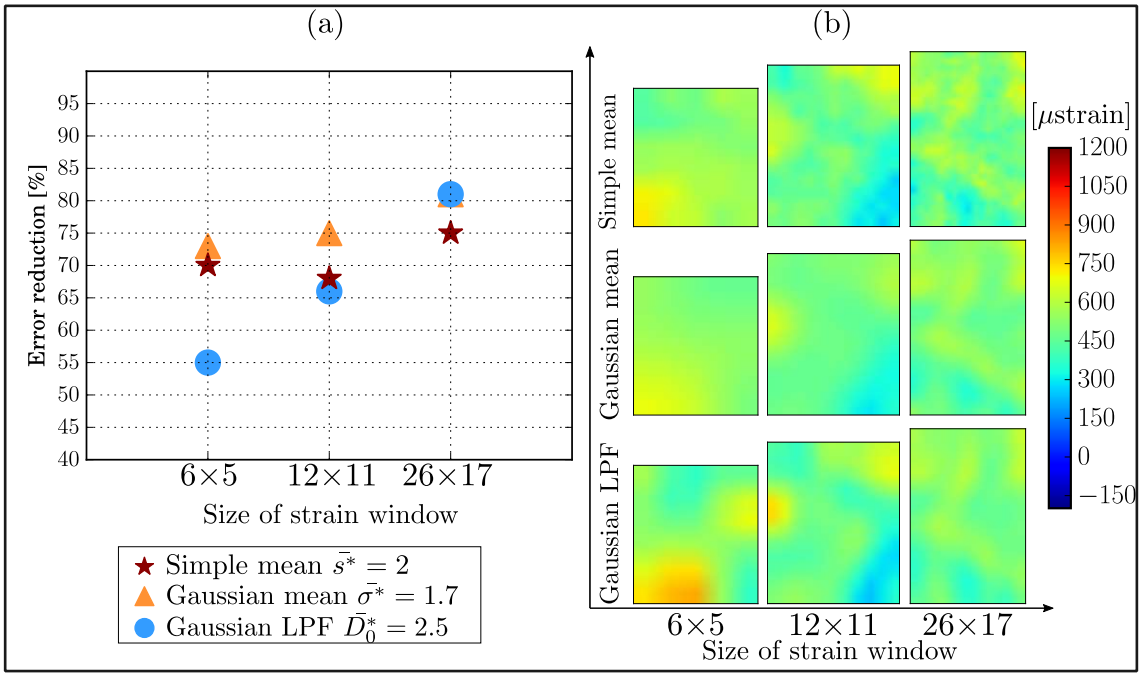

Figure 4.10: Error reduction achieved for simulated constant strain fields (a) Percentage of error reduced for the different sizes of the strain windows and the filters, (b) Two-dimensional visualization of the filtered constant strain fields.

An overview of error reduction achieved for a selected strain window of 12×11 points is summarized in Table 4.1.

Table 4.1: Achieved error reduction for simulated strain fields and filtering approaches for a 12×11 strain window.

Filter/Field	**Quadratic**	**Linear**	**Constant**
Simple mean ($\bar{s}^* = 2$)	66%	69%	67%
Gaussian mean ($\bar{\sigma}^* = 1.7$)	72%	74%	75%
Gaussian LPF ($\bar{D}_0^* = 2.5$)	69%	69%	66%

4.6.2 Experimental strain fields

For samples deforming under tensile load, the size of the strain window was about 12×11 measurement points and the noise had an RMSE amplitude of $234.23 \pm$

60.06 to 302.50 ± 45.64 µstrain independent of the load level. The reference strain measurements, DIC strain measurements and its standard deviation for the four load levels are presented in Table 4.2.

The overall optimal filters ($\bar{s}^* = 2$, $\bar{\sigma}^* = 1.7$, $\bar{D}_0^* = 2.5$) were applied on the strain windows from the steel samples. The total error and the error reduction level are depicted in Figure 4.11a at four loading steps 500, 1500, 2000 and 3000 N load, Figure 4.11b shows the corresponding 2D interpolated strain fields overlaid with the discrete measurement points. The total error was reduced by 50% when applying the three overall optimal parameters, without any remarkable difference with regard to the load level.

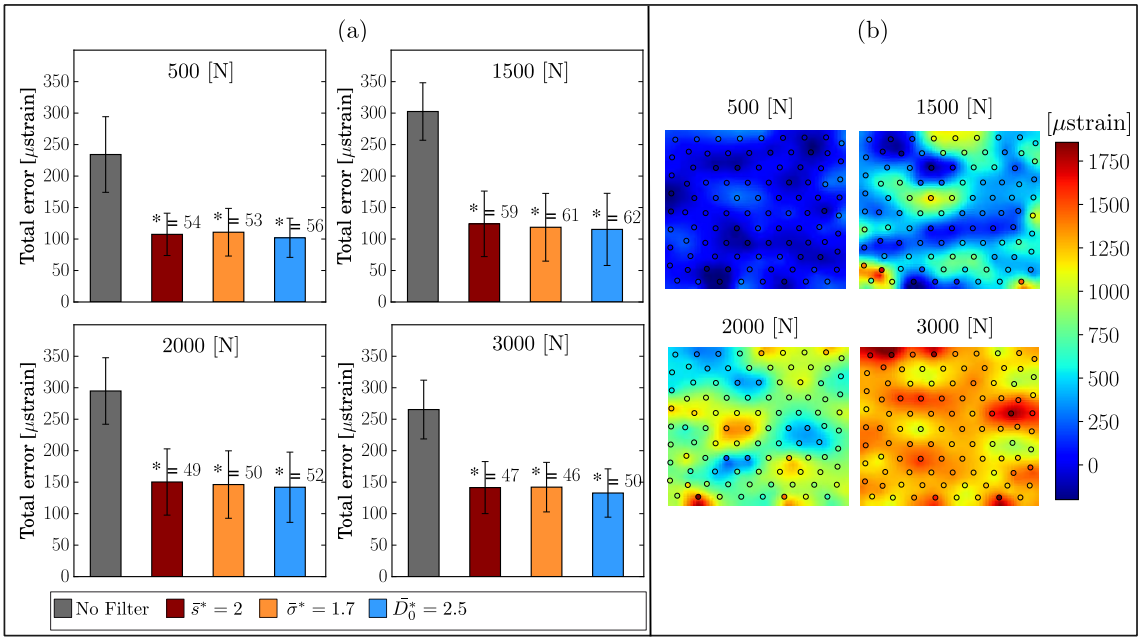

Figure 4.11: (**a**) Total error and accuracy of filtering a 12 × 11 stain window of steel samples. (**b**) Two-dimensional interpolated strain fields overlaid with the discrete measurement points. Both presented at 500, 1500, 2000, and 3000 N load steps. No Filter is the raw DIC measurement points.

Table 4.2: Reference strain (measured by the extensometer) vs. DIC strain and standard deviation measured on the surface of steel samples under tensile load. Strain values are in µstrains.

Load [N]	Reference	Average Strain ± Std
500	288.42	267.64 ± 217.76
1500	689.11	610.85 ± 281.87
2000	1068.57	997.15 ± 266.51
3000	1448.31	1394.57 ± 234.39

4.7 Discussion

The goal of this study was to examine three practical filtering approaches, to compare their effectiveness on three simulated strain fields (linear, quadratic, and constant) where the 'True' reference strain is known, to find optimal filter parameters with minimum compromising between residual noise and loss of information, and to apply such filters to experimental strain fields. A simple mean with $\bar{s}^* = 2$, a Gaussian mean with $\bar{\sigma}^* = 1.7$, and a Gaussian LPF with $\bar{D}_0^* = 2.5$ were identified as the overall optimal filter parameters for the examined strain window size and strain field type. These filters give at least an error reduction above 32%, 37% and 59% for simulated fields and an error reduction above 47%, 46% and 50% for experimental fields.

On the one hand, the Gaussian mean filtering is outstanding in terms of error reduction for constant strain windows (Figure 4.10). On the other hand, for linear and quadratic strain windows (Figure 4.8), the shape of the total error curve shows high gradients around the minimum point, which implies a sharper increase in the total error when deviating from the specific optimal σ^*. The increase in total error (Figure 4.9) from when σ^* to $\bar{\sigma}^*$ was applied is around 75 µstrain for the smallest (6×5) strain window size, and about 12 µstrain for the other strain window sizes. The same can be seen for the loss of information and residual noise Figure 4.6b,b1 and Figure 4.7b,b1, respectively.

The Gaussian LPF behaved based on the shape of the strain window rather

than the size. For homogeneous/constant strain field, the noise can be filtered using a $D_0 < 0.5$, by letting only the smallest frequency pass and blocking all higher frequency components, as this might work well for homogeneous/constant fields. This does not work for linear and quadratic fields and will result in a corrupted strain distribution, as confirmed as well by Baldoni et al. [13] with total error, in our case, higher than the original noise (Figure 4.8c,c1). As well, when applying filtering on the speckled DIC image prior to the correlation calculation, Butterworth LPF produced the lowest random error [31]. The Gaussian LPF was the only filter where the loss of information was reduced with increased cut-off frequency. This is because the reference strain—in case of the simulated fields—is noiseless, and when increasing the cut-off frequency, the whole signal passed, allowing the filtered field to be identical to the original field. However, for the residual noise, with increasing the cut-off frequency, the noise remaining in the filtered field is increasing mildly, as depicted in Figure 4.7c,c1.

These three overall optimal parameters that reduced the noise in both the simulated and the experimental fields can be used, for comparable strain window sizes, when no prior information is available on the strain field. Simple mean filtering is handy since it is a built-in function that usually comes with commercial DIC systems, but for the smallest strain window 6×5 points (Figure 4.9, top, left)—if the optimal filter size was not used—a serious compromise of the results can occur, with noise reduction from 300 to 287 μstrains. If the overall optimal parameter was used, the noise reduction is limited to 38% and 32% for the linear and quadratic fields, respectively.

It was demonstrated here how the size of the strain window influences the noise reduction, better denoising is achieved for bigger strain window sizes [143, 121, 144], which is expected, since for bigger stain windows, more facets can be calculated and the signal-to-noise ratio is higher than for smaller strain windows. This can be seen clearly in the total error curves in Figure 4.8, where the minimum and maximum total error were reached for the 26×17 and 5×6 strain windows, respectively. Filtering, either on the displacement field, the strain fields or the speckled images, helps to reduce noise in DIC fields [17, 18, 31, 13], but the optimization of other

factors that influence the noise is necessary, such as facet and step size. For facet size; a bigger facet size results in better identification of the facets and is favoured for the correlation algorithm [129, 121, 145]. Other studies showed that the error can be largely reduced by increasing the facet size [146, 15]. However, since we seek to improve DIC measurements for inhomogeneous specimens or for specimens with geometry that allow strain concentration, choosing a bigger facet size is not ideal and would lead to hide the strain concentrations. For our case, with a fixed dimension of the strain fields between the extensometer, more data points can be measured with smaller facet size and/or step, but at the cost of more noise which was confirmed by other studies [70, 127, 15, 130]. When the facet size was set to be 13×13 pixels with 11×11 pixels facet step, the RMSE doubled from 300 to 600 µstrains with maximum apparent strain exceeding 1000 µstrains, thus, when inhomogeneous strain concentration is expected, a good compromise is needed between a larger facet size to suppress the noise and a smaller one to capture the strain concentration.

As a general DIC filtering guideline, filters available by the DIC commercial software or by a computational software such as Python can be useful in reducing the noise in DIC fields. However, as demonstrated above, the selection of the filter parameter should be based on an optimization process to ensure the minimum loss of information and the preservation of the strain gradient. The concept of the total error as a combination of the loss of information and residual noise is a powerful tool to see the influence of each filter on the DIC measured data points. When applying filters provided by a commercial DIC software, it is important to keep in mind the relation between the filter parameter and the size of the strain field.

The limitations of this study are that specific-simulated strain fields were tested, and the experimental results represent only homogeneous strain fields. In future, it has to be proven that the presented approach works also for real measured higher-order strain fields. Only strain window sizes up to 26×17 points (20.8×13.6 mm) are considered, since smaller strain windows sizes are influenced by higher noise. One length scale of the noise was investigated in this study, which was obtained from the experimental findings. Additionally, filtering was applied directly on strain field measurement points obtained from the software i.e. no filtering on displace-

ment fields, no investigation on different strain computation methods, or different correlation algorithms, such as global and local DIC approaches, were investigated in this study. Finally, optimal filtering parameters presented here might not be optimal for other applications with different DIC systems or at different length scales.

4.8 Conclusion

DIC offers a method for capturing full-field deformation on the surface of the samples, regardless of their size, shape or material. With appropriate analysis parameters, DIC can capture the strain on the surface of tested samples. The present study has illustrated that strain computed by DIC commercial software (ARAMIS v6.3.1; GOM) is comparable to strains obtained from a high precision extensometer attached to the same sample. The DIC noise was stable over the different load levels in the elastic deformation region of the material.

However, DIC measurement cannot be taken for granted without checking the noise-floor; thus, preliminary tests at zero-strain can give an idea on the noise-floor of the measurement due to software or hardware parameters. Few studies focus on filtering the strain fields, in this study a procedure to select an optimal filter parameters has been presented. The results found in this study show that optimal filtering can have a positive effect on reducing the noise, but at the cost of losing information, especially for simple mean and Gauss mean filters. Optimal Gauss LPF proved to be effective in reducing the noise without excessive loss of information. This effect can only be shown by using simulated strain fields where a noiseless reference strain field is known. When filtering DIC measurement on sample with irregular shape or inhomogeneous material such as bone, practical filtering guidelines as given in this study can be very helpful.

CHAPTER 5

Linear gradient strain fields can be measured using DIC

5.1 Related publications and declaration of contributions

Results of the presented work (text, tables, figures) were *published* in the 'Journal Scientific Reports' in 2021, entitled 'A novel specimen shape for measurement of linear strain fields by means of digital image correlation', and co-authored by A. Reisinger and D. H. Pahr.

Authors contribution The first author and the author of this thesis, *Nedaa Amraish*, wrote the manuscript, performed the experiments, data analysis and interpretation. *A. Reisinger* reviewed the manuscript. *D. H. Pahr* supervised the work of Nedaa Amraish, conceptualized the geometry of the novel sample, and provided the data for the normalized strain gradient computation on the femur's neck, reviewed and edited the manuscript and supported the interpretation of the results.

After identifying optimal filtering parameters that successfully reduced the noise in

simulated noisy strain fields, an experimental study is presented here measuring linear gradient strain fields using DIC on a macroscopic scale of engineering and biological materials.

5.2 Introduction

DIC measures full-field strain on the surface of specimens by capturing images during mechanical testing. Due to its main advantage in measuring full-field surface strains on specimens with irregular shape and different sizes, 2D and 3D DIC systems have been used to characterize a wide range of materials under different experimental setups [2, 3, 4, 5]. Despite the advantages of using DIC systems to capture full-field strain distributions, noise in DIC strain measurements is non-negligible [10, 11, 12, 13, 14]. DIC measuring parameters, like facet and step sizes, can be optimized to reduce the noise of the full-field data. However, in case of measuring on a surface where inhomogeneous strain fields are expected, the typical optimized DIC parameters might have a counter effect because the risk of losing information is higher, specially at locations of higher strain gradients [121, 70, 25]. Additionally, different filtering techniques can be applied to reduce the noise in DIC measurements, which, if not carefully applied, can have an effect of over smoothing leading to loss in information [18, 13], filtering can be powerful when the true strain distribution is known a priori.

For homogeneous strain fields, such as fields expected on regular aluminium [30, 13, 15] or steel [55, 133] specimens with constant cross-section, DIC measurements can be verified using strain gauges or extensometers. However, for inhomogeneous strain fields, such as strains found on complex structures [68, 66, 69, 147, 91, 70] or biological tissues like, the human femur [87, 6, 14], bone from different animal models [148, 58, 21, 86], the vertebrae [82, 83, 84, 85, 52], or soft tissues [149, 116], verifying the full-field DIC strain measurements can become challenging.

Various studies examined the accuracy of DIC strain measurements and showed that the strain on the measured surfaces can be overestimated [87, 21, 14, 15].

The precision of DIC measurements is acceptable when specimens are deforming in the linear-elastic region, but after yielding, the standard deviation increases vastly [150, 71]. Two options could be employed for investigating the accuracy of DIC strain measurements, either by verifying the measurement at the position of measurement device [20, 6, 23, 21, 22], or by means of FE models for the full-field strain distribution [13, 14, 25]. Despite the high accuracy of strain gauges and extensometers, their measurement is limited to a single point, and can be compared to DIC measurements only by averaging the full-field data over the strain gauge area [23, 15, 24], which is only advantageous for homogeneous strain fields. In contrast, FE models can give accurate prediction of the full-field strain measurements, but it is important to know the geometry, material behaviour and boundary conditions. With knowledge of these parameters FE models are a suitable way to evaluate strain inhomogeneity [25, 26, 27]. For example, Liu et al. [25], investigated experimentally the strain concentration on hydrogel specimens in the presence of large strain gradients, they found a very good agreement between the FE results and the measured DIC full-field strain, however, 2D DIC was employed which is less useful for objects with curvatures, like the human femur.

Inhomogeneous strain fields were measured on the surface of biological tissues [6, 21, 151, 73]. For example, on the neck of the human femur, the normalized strain gradient changes by about 7% per mm on average (more in the next section). DIC measurements is advantageous not only for measuring inhomogeneous strain fields, but also for measuring strain gradients [7, 8, 9]. Various studies reported DIC full-field strains without reporting the accuracy of the measurement or validating it against another method, Tsirigotis et al. [80] found that the surface strain, on bovine cancellous bone under compression load, showed steep strain gradients. Likewise, Palanca et al. [29] and Grassi et al. [28] measured full-field surface strain on the superior neck of human femurs. However, the strain results were not validated against another measurement method, and Tsirigotis et al. [80] used 2D DIC. Many DIC strain measurements on different bone models were verified using strain gauges only, and were used to verify FE models [91, 152, 20, 153, 21]. Despite the numerous studies on the accuracy of DIC measurements, only one study, Baldoni et al. [13], verified linear experimental full-field DIC strain measurement, the verification was

against the theoretical solution and not against another measurement technique, and the strain gradient was not analysed.

Other studies focused on testing the accuracy of DIC numerically. For instance, Wang et al. [70], tested the accuracy of 2D DIC for inhomogeneous strains of numerically deformed images, they found that the uncertainty of DIC increases around the strain concentration regions, here the reference images were also captured by one camera only (2D DIC), and numerically deforming the images excludes the errors originated from the experiment's environment. A verification of 3D DIC measurements for linear strain fields and strain gradients experimentally is still missing. To verify inhomogeneous strain fields measured by DIC, the strain gradients on the specimen's surface must be known. Inhomogeneous strain fields such as linear or quadratic strain fields are good candidates since the analytical (theoretical) solution can be calculated beforehand. This study is focusing only on linear strain fields.

The objective of this study is to design a novel specimen shape where a well-defined linear gradient field can be measured and to investigate the accuracy of DIC full-field strain measurement globally and locally. This is the first study to systematically evaluate and validate inhomogeneous DIC strain measurements on surfaces where strain gradients are expected on biological and engineering materials. Measurements are done with a 3D DIC system and the noise in the DIC strain fields is reduced by applying Gauss low-pass filtering with optimal cut-off frequency. strain gauges are used to measure the experimental strain at pre-defined positions, which was compared to the DIC strain measurement locally. Summarizing, this work aims at verifying whether DIC measurements can capture gradient fields and local normalized strain gradients at specific positions in case of bone and for comparison purposes on typical engineering materials (aluminium and polymer).

5.3 Materials and methods

5.3.1 Normalized strain gradient

To explore the capability of a DIC system to measure linear strain fields on the surface of the test specimens, it is necessary to design a specimen shape where the strain on the surface of the specimen changes linearly during deformation. Different options are available to design such a specimen, either by changing the width or the thickness of the test specimen. In this study, it is intended to measure strain gradient magnitudes similar to that found on a surface of a proximal human femur. For this purpose, a load and size independent measured value - a normalized strain gradient - is defined. This is based on a normalized strain $\varepsilon_{\text{norm}}$ which is the difference between the strain at two points divided by their average quantity (Equation (5.1)). The gradient is obtained by dividing this normalized strain by the distance of these two points (Equation (5.2)).

$$\varepsilon_{\text{norm}} = \frac{|\varepsilon_{\mathbf{p1}} - \varepsilon_{\mathbf{p2}}|}{\frac{\varepsilon_{\mathbf{p1}} + \varepsilon_{\mathbf{p2}}}{2}} \tag{5.1}$$

$$\varepsilon_{\text{norm grad}} = \frac{\varepsilon_{\text{norm}}}{d}[\frac{1}{\text{mm}}] \tag{5.2}$$

where $\varepsilon_{\mathbf{p1}}$ and $\varepsilon_{\mathbf{p2}}$ in this work are equivalent strains ε_{eq} which are measured at two locations **p1** and **p2** on the femur, and d is the distance between the two points, see Figure 5.1 shows a strain energy density (SED) map of a proximal femoral under physiological load [154].

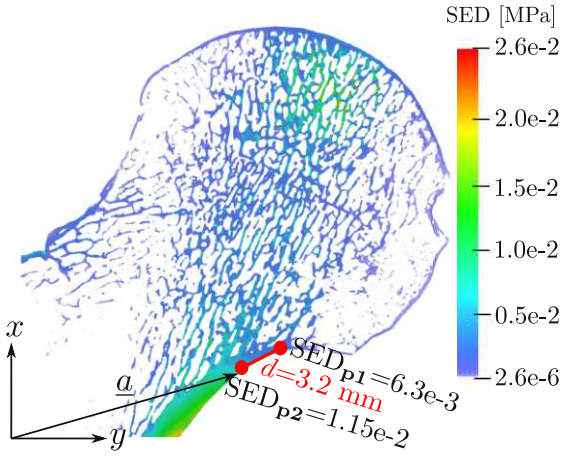

Figure 5.1: Strain energy density map from which the equivalent strain was computed and was employed for the computation of the normalized strain gradient.

The equivalent strain ε_{eq} is obtained from the local SED and elastic modulus (10 GPa) as follows:

$$\varepsilon_{\text{eq}} = \sqrt{\frac{2SED}{E}} \tag{5.3}$$

For the human femur, the normalized strain gradient is about 3.5 and 7.2% per mm on average in the head and neck regions, respectively, see Table 5.1. This work aims to design a specimen shape which under deformation gives a linear strain field, and where two normalized strain gradients of around 3.5 and 7% per mm (regardless of the load applied) can be found on the surface.

Table 5.1: Normalized strain gradient computed from the equivalent strain, all strain values are in µstrain.

$\varepsilon_{\mathbf{p1}}$	$\varepsilon_{\mathbf{p2}}$	$\lvert\varepsilon_{\mathbf{p1}} - \varepsilon_{\mathbf{p2}}\rvert$	$\frac{\varepsilon_{\mathbf{p1}}+\varepsilon_{\mathbf{p2}}}{2}$	**d[mm]**	$[\frac{\%}{\text{mm}}]$
1288	860	428	1074	3.27	12.16
1483	1311	171	1397	3.05	4.03
1655	1378	276	1516.5	3.26	5.60
1342	1039	302	1190.5	3.50	7.26
Average normalized strain gradient - neck region					7.26 $[\frac{\%}{\text{mm}}]$
948	989	41	968.5	3.27	1.30
748	848	100	798	3.05	4.12
860	761	98	810.5	3.26	3.73
1010	848	161	929	3.5	4.96
Average normalized strain gradient - head region					3.53 $[\frac{\%}{\text{mm}}]$

5.3.2 Analytical strain and specimen shape

A linear field in a tensile specimen can be generated by a specific specimen shape. In the following derivations, we calculate the specimen shape. The exact strain distributions for comparison with DIC are determined by means of FE.

In the following uniaxiality is assumed, $w(x)$ is the width (shape) of the specimen, and $\varepsilon(x)$ is the strain along x, see Figure 5.2(a and b). A one-dimensional linear strain field can be written as:

$$\varepsilon(x) = a + bx \tag{5.4}$$

where a is a point on the specimen where the strain shows the far field value, b is the slope of the linear strain and x is a position along the specimen's axis, see Figure 5.2. Solving for a and b at the positions 0 and L gives:

$$\text{at } x = 0: \qquad \varepsilon(0) = a \tag{5.5}$$

$$\text{at } x = L: \qquad \varepsilon(L) = \varepsilon(0) + b \cdot L = \varepsilon(0) \cdot k \tag{5.6}$$

where the maximum strain $\varepsilon(L)$ can be linked to the far field strain $\varepsilon(0)$ by a concentration factor k. Solving for the slope of the linear equation, b:

$$b = \frac{\varepsilon(0)}{L} \cdot (k-1) \tag{5.7}$$

the strain at any point between a and L can be calculated via inserting a and b in Equation (5.4):

$$\varepsilon(x) = \varepsilon(0) + \frac{\varepsilon(0)}{L} \cdot (k-1) \cdot x = \varepsilon(0)\left(1 + (k-1) \cdot \frac{x}{L}\right) \tag{5.8}$$

Due to the asymmetric specimen shape as shown in Figure 5.2, two different strain gradients can be realized. For example, if $\varepsilon(0)$, L and k are prescribed, the strain function and the normalized strain gradient (Equation (5.2)) along the specimen's length can be computed. The normalized strain gradient changes between 4.4 and 22% per mm, and between 3 and 14% per mm for specimen's length of 18 and 27 mm, respectively. Two positions were selected relatively close to the middle of the specimen for the normalized strain gradients investigation. These are the nearest values to the two normalized strain gradients found on the surface of the human femur (3.5 and 7.3% per mm), which are 3.6 and 6.9% per mm for a specimen's length of 18 and 27 mm, respectively.

The unknown width of the specimen $w(x)$ follows from the equilibrium i.e. the force experienced along the specimen's length is constant at one loading stage:

$$F(0) = F(x) \tag{5.9}$$

therefore, the equation can be rewritten in terms of stress ($\sigma(x) = E \cdot \varepsilon(x)$) and cross-sectional area ($A = 2w(0) \cdot t$):

$$E \cdot \varepsilon(0) \cdot 2w(0) \cdot t = E \cdot \varepsilon(x) \cdot 2w(x) \cdot t \tag{5.10}$$

where t is the thickness of the specimen (which is constant), $w(0)$ is the half-width of the specimen and equals 12.5 mm, see Figure 5.2(a). Equation (5.10) can be

rewritten as:

$$w(x) = \frac{\varepsilon(0) \cdot w(0)}{\varepsilon(x)} \tag{5.11}$$

solving for $w(x)$:

$$w(x) = \frac{\varepsilon(0) \cdot w(0)}{\varepsilon(0)\left(\frac{L+(k-1)\cdot x}{L}\right)} = \frac{w(0)}{1+(k-1)\cdot\frac{x}{L}} \tag{5.12}$$

Figure 5.2(a) shows the specimen's geometry for k=5 by plotting $w(x)$ from Equation (5.12) for two lengths, in red and blue, in Figure 5.2(a). The size limitation in this work was on the one hand the specimen width of 25 mm for bone and on the other hand the specimen width of 5 mm in SG2 ROI for the application of SG2. The overall length of the specimen was 193 mm for aluminium and polymer specimens and was 73 mm for bovine bone specimens. The length of the Region of Interest (ROI) is 53 mm and is divided into three regions (L1, L2 and L3). L1 is 18 mm long (high-gradient ROI, showing 6.9% per mm normalized strain gradient), L2 is 8 mm long (constant strain, no gradient), and L3 is 27 mm long (low-gradient ROI, showing 3.6% per mm normalized strain gradient). In these three regions, three strain gauges are applied at specific locations. Three ROIs are investigated in this study: the high- and low-gradient ROIs and the strain gauges ROIs. Figure 5.2(b) shows the linear strain (in red and blue) along the shape of the specimen.

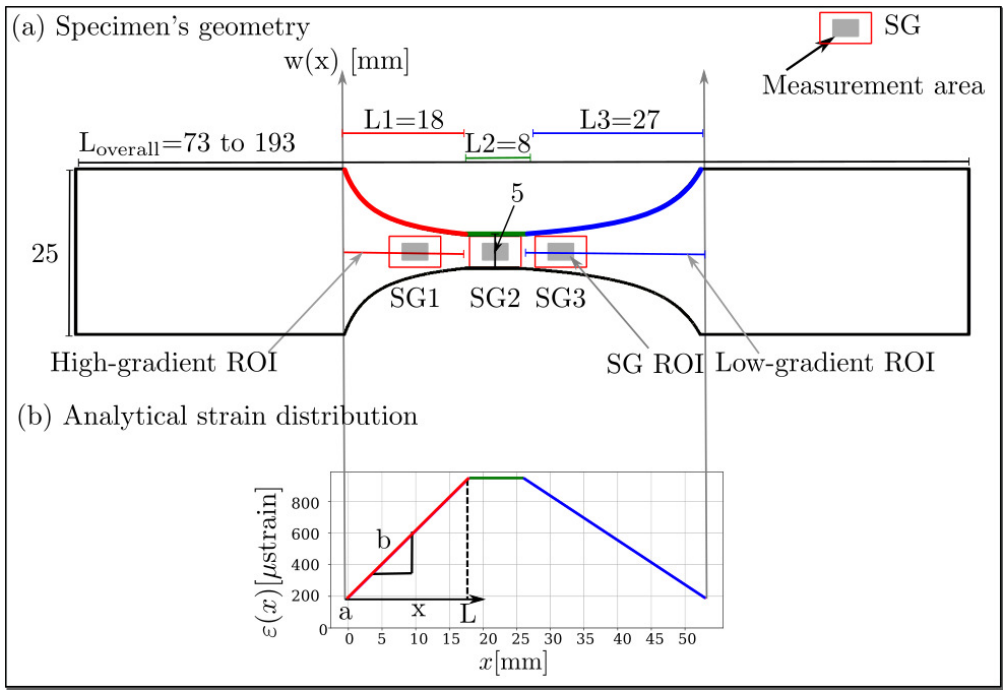

Figure 5.2: (a) Specimen's geometry derived from Equation (5.12), $w(x)$ shows how the curvature of the specimen changes; in red and blue the high- and low-gradient ROIs are shown, respectively. L1 is the high-gradient ROI and where SG1 is placed. L2 is a neutral ROI connecting the high-gradient ROI with the low-gradient ROI, L2 shows constant strain and where SG2 is placed. L3 is the low-gradient ROI and where SG3 is placed. (b) The theoretical strain distribution along the specimen's length. The high- and low-strain gradients are shown in red (steeper curve) and blue, respectively. Constant strain (in green) connects both gradient regions.

5.3.3 strain gauges strain

Strains were recorded with one-element, 120-ohm rectangular strain gauge (K-CLY4-0030-1-120-3-020, HBM, Darmstadt, Germany). The strain in the loading direction was recorded (acquisition frequency 5 Hz) using a QuantumX data acquisition (HBM, Darmstadt, Germany).

The positions of the three strain gauges are depicted in Figure 5.2. SG2 was applied at L2 where the strain is constant. This strain was used to calibrate the FE models, as described below for the FE model. SG1 and SG3 were applied where

the normalized strain gradient is 6.9 and 3.6% per mm, which as explained above can be found on the surface of the femoral neck and head, respectively.

5.3.4 Numerical strain (FE model)

The analytical strain field from Equation (5.8) does not consider the Poisson effect. To check the analytical model and verify the accuracy of the DIC measured strains, FE models were generated to provide accurate strains. The FE models were created for each specimen using an open source Calculix solver (PrePoMax, v0.6.0). The specimens' geometry are as shown in Figure 5.2(a). The specimens were meshed with tetrahedral (C3D10) second-order elements of the size 0.8 mm, see Figure 5.3. To scale the FE strain to the strain measured by SG2, 1 mm displacement (u_x) was imposed on the specimen, simulating a uniaxial tensile test in the x-direction. The obtained FE strain was scaled so that the FE strain is equal to the strain in SG2. This is possible because of the linear elastic system.

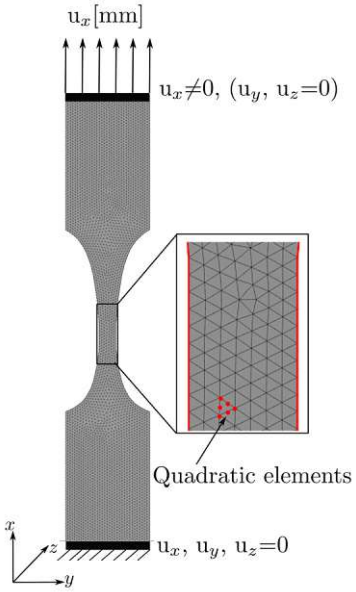

Figure 5.3: FE model including boundary conditions and mesh. The displacement was applied on the top of the specimen, while the bottom was constrained to mimic the experimental conditions. No material parameters (Elastic modulus) were assigned to the specimens because only strains were calculated and the FE simulation is displacement control. A poisson's ratio of 0.3 was assigned for all specimens.

5.3.5 DIC strain measurements

DIC computes full-field strain on the surface of the specimen. More information is available here [133] on how DIC computes strain. For this study, the surface strain was computed with a facet (subset) size of 19×19 pixels and a facet step of 16 pixels (50% overlapping), these parameters are recommended by the manufacturer for 6 Megapixel CCD cameras. The strain in the loading direction were exported from the ARAMIS Professional software (v6.3.1; GOM GmbH, Germany) along the node number (> 600 measurement points) and $x-$, $y-$, $z-$coordinates, for plotting and post-processing with Python SciPy.

5.3.6 Sample preparation

The specimen shape was produced in aluminium (ALMG3 (AW-5754)) (n=5), polymer (Polyacetal POM-Copolymer) (n=5) and Bovine bone (n=5). Aluminium and polymer specimens were manufactured by means of a numerical controlled machine (CNC Router BZT PFX 700, BZT Maschinenbau GmbH, Leopoldshöhe, Germany) from aluminium and polymer plates of 1.5 mm and 4 mm thickness, respectively.

For bovine bone, two fresh compact femurs of bovines (18-24 months old) were obtained from the local butcher. The mid-diaphysis of the femur was cut, and the hollow cylinder of the femur shaft was then cut into rough rectangular beams using a hand saw. After that, the beams were embedded into an epoxy mould which was then fixed into a CNC machine to obtain the shape of the specimen. Finally, using a low-speed diamond band saw (Exakt 300 CL Band System, EXAKT Advanced Technologies GmbH, Norderstedt, Germany), longitudinal specimens were sliced (thickness of 2 mm), see Figure 5.4(a). During the whole preparation steps and until testing, the bone specimens were kept wet with phosphate buffered-saline (PBS) solution, and when not used, the specimens were preserved in a -20 °C freezer.

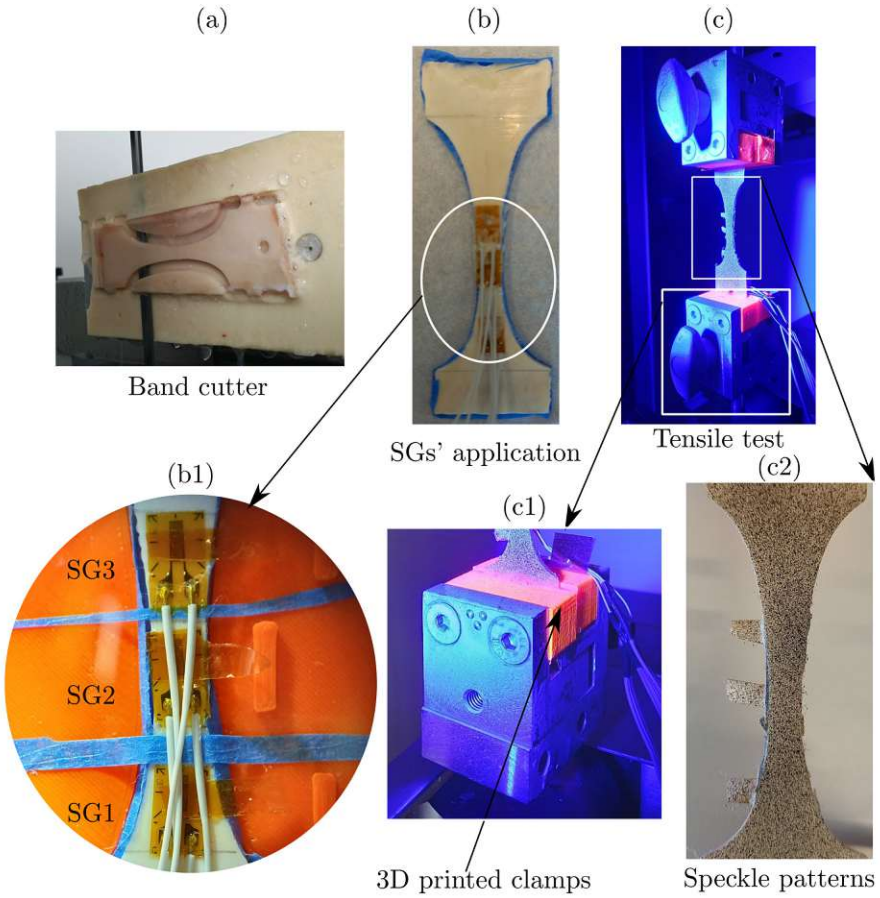

Figure 5.4: Preparation steps of the bovine bone specimens. (a) Bone specimens were sliced using a slow band saw, (b) SG1, SG2 and SG3 were applied on the specimen's back, (c) mechanical test setup, (c1) the bone specimen was fixed to external clamps, and (c2) speckle patterns were applied on the specimen's front.

Three strain gauges were applied on one face of the test specimens as in Figure 5.4(b), while the other face was covered with paper tape to protect it against any glue resins during the strain gauges' application. First, using a light microscope, the position of the strain gauge was precisely marked on the surface of the specimen. Second, two components glue (Methyl methacrylate, HBM, Darmstadt, Germany) were mixed and applied on the bone surface, and then each strain gauge was carefully applied. A similar procedure was followed for the aluminium and polymer specimens; only another glue (Cyanoacrylate, HBM, Darmstadt, Germany) was applied to fix the strain gauges on the specimens' surface as recommended by the

manufacturer of the strain gauges.

The bone specimen was then fixed to external clamps by glueing the specimen to 3D printed parts using two components glue for 5 minutes (Fiber-reinforced composite, Waldenbuch, Germany) as in Figure 5.4(c1). Finally, the strain gauges cables were welded to an adaptor (full-bridge) which was connected to a QuantumX DAQ device (HBM, Darmstadt, Germany) for data acquisition. Before the starting of the mechanical load, the specimens were clamped to the tensile testing machine and were exposed to the blue light for the DIC system, see Figure 5.4(c).

5.3.7 Mechanical tests

The test specimens were mounted on a Zwick (Z030) machine (ZwickRoell GmbH, Germany) with force cell up to 30 kN. 3D DIC system (ARAMIS 150/6M/Rev.02, GOM, Braunschweig, Germany) was set up with two CCD cameras. The cameras were positioned perpendicular to the specimen at 35 cm distance. The strain gauges cables were welded to an adaptor (full-bridge) which was connected to a QuantumX DAQ device (HBM, Darmstadt, Germany) for data acquisition. Finally, the specimens were subjected to a uniaxial tensile load along the vertical direction (displacement control) with cross-head movement of 0.5 $mm.min^{-1}$ till fracture. The acquisition rate was synchronized between the strain gauges and the DIC system at 5 Hz.

5.4 Data evaluation

In this study, the strain measurements were defined over three ROIs: high- and low-gradient ROI, and strain gauges ROIs, see Figure 5.5. The scaled full-field strain obtained from the FE model is considered as the reference strain. At the high- and low-gradient ROIs, the accuracy of the DIC strain measurements and the analytical strain computation are evaluated by means of the RMSE. At the strain gauges ROIs, the two experimental strains from DIC and the strain gauges

are compared statistically, and the normalized strain gradients (6.9 and 3.6% per mm) are computed and compared to the reference obtained from FE.

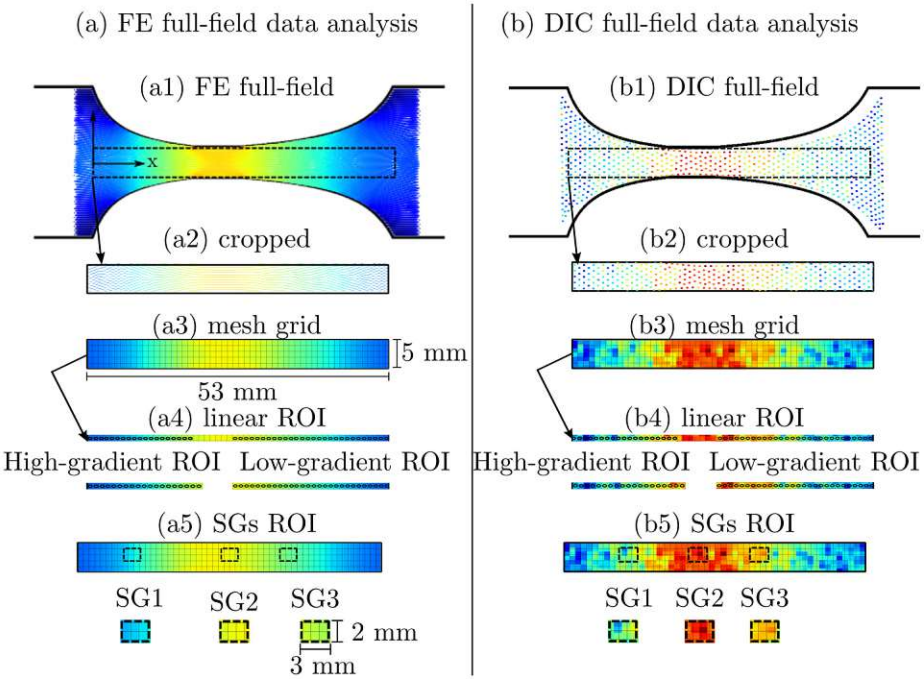

Figure 5.5: RMSE computational method. (a and b) FE and DIC full-field data analysis respectively, (a1 and b1) the full-field surface strain from FE and DIC, (a2 and b2) cropping of the linear regions excluding the boundary nodes, (a3 and b3) a 53 mm × 5 mm mesh grid for aligning the measurement points into a regular grid, (a4 and b4) the high- and low-gradient ROIs from the middle line along the specimen's length were extracted, (a5 and b5) strain gauges ROIs were cropped at SG1 and SG3.

Figure 5.5 shows the computational method of the RMSE:

- The full-field strain (Figure 5.5(a1 and b1)) obtained from both FE and DIC, respectively. They were cropped horizontally and vertically based on the x- and y- coordinates.
- The cropped fields were interpolated into a regular mesh grid of (53 mm × 5 mm) points, see Figure 5.5(a3 and b3) to be able to compare values.
- The middle line of the interpolated fields was exported into a 1D matrix, see Figure 5.5(a4 and b4) for line plots along the centre of the specimen.

- The positions of the three strain gauges were cropped from the (53 mm × 5 mm) mesh grid for strain gauge's size of 3 mm × 2 mm, see Figure 5.5(a5 and b5) to compare values inside the strain gauge's region.

- The RMSE was calculated for the high- and low-gradient ROIs.

The RMSE equation is:

$$\mathrm{RMSE}_{\mathrm{Method}} = \sqrt{\frac{1}{n}\Sigma_{i=1}^{n}\left({}^{\mathrm{FE}}\varepsilon_i - {}^{\mathrm{Method}}\varepsilon_i\right)^2} \tag{5.13}$$

where $\mathrm{RMSE}_{\mathrm{Method}}$ refers to the RMSE computed for each method, i.e. $\mathrm{RMSE}_{\mathrm{DIC}}$ is the RMSE of the DIC strain measurements compared to FE strains, n is the number of strain measurement points (i) in a ROI, ${}^{\mathrm{FE}}\varepsilon_i$ is the value of the reference strain (FE), ε_i is the value of the analytical or DIC strains.

The RMSE was evaluated at two deformation stages, hereinafter referred as (Stage_1 and Stage_2). Stage_1 is at approximately 500 µstrain, a low strain level similar to the noise level of the DIC measurement. Stage_2 is at approximately 1750 µstrain level which is found during normal ambulation and is comparable for bone deformation under physiological load [155]. Because the exact values of 500 and 1750 µstrain were not found in all the measurements of SG2 for all the test specimens, the nearest measurement points to 500 or 1750 µstrain were selected which were about 496 and 1698 µstrain, respectively. The nearest point had a difference of less than 3% to 500 or 1750 µstrain.

To answer the question of how well the local strain gradient can be captured with DIC compared to FE, the two normalized strain gradients (6.9 and 3.6% per mm) are computed as in Equation (5.2). Basically, along the specimen's axis, first the normalized strain (Equation (5.1)) is computed by dividing the difference in strain measurement between two measurement points by their average quantity. Then, the normalized strain gradient is computed by dividing the normalized strain by the distance between the two measurement points, 2 mm.

5.4.1 Noise reduction

Gaussian LPF with cut-off frequency of 2.5, which was found as the optimal cut-off frequency in our previous study [133], was applied to the DIC full-field strain measurements to reduce the noise in the DIC strain measurements. The same cut-off frequency was applied on all stages, independent of the load applied.

5.5 Results

5.5.1 Mechanical testing

The stress-strain curves of all tested specimens (five of each material), with strain obtained from SG2 (constant strain) are shown in Figure 5.6. The two vertical dashed lines show the deformation stages ($Stage_1$ and $Stage_2$) at which the results were evaluated.

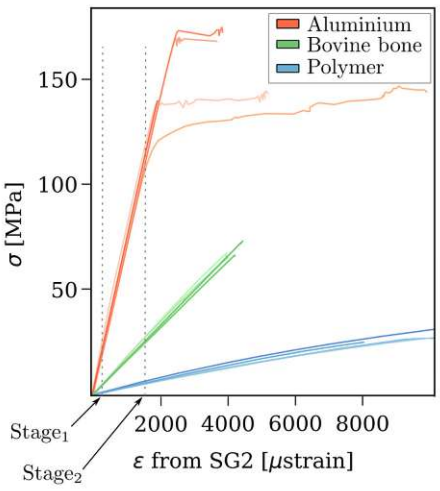

Figure 5.6: Stress-strain curve of all tested specimens. Aluminium in red, bovine bone in green and polymer in blue. The error evaluation was done at two deformation stages, approximately at 500 µstrain and 1750 µstrain. Five specimens were tested from each material.

From the stress-strain curve, the elastic modulus was computed for the tested materials and it was on average 71.37±2.03, 3.24±0.25, and 16.92±0.61 GPa for aluminum, polymer, and bovine bone, respectively, see Table 5.2 lists the elastic modulus for all specimens. For bovine bone, results of the elastic modulus are in agreement with values found in the literature for cortical bone [156, 157, 158]). For aluminium and polymer specimens, the measured values are in agreement with the manufacturer.

Table 5.2: Elastic modulus obtained from SG2 for each of the tested specimens.

Specimen #	**Aluminium**	**Polymer**	**Bovine bone**
	Elastic Modulus [GPa]		
1	68.57	3.12	17.69
2	73.99	3.60	16.44
3	71.02	2.98	17.51
4	70.74	3.10	16.54
5	72.52	3.41	16.45

5.5.2 RMSE for the high- and low-gradient ROIs.

The RMSE was evaluated for the high- and low-gradient ROIs, as shown in Figure 5.5(c1 and c2). Figure 5.7 shows the two ROIs plotted along the specimen's length at two deformation stages (Stage_1 and Stage_2). For aluminium and polymer, there is a good agreement between the FE strain, the analytical strain and the filtered DIC strain. For bovine bone, the DIC strain overestimated the strain in the high-gradient ROI at both deformation stages, in contrast to the low-gradient ROI where DIC strain underestimated the strain in comparison to FE strain. In all curves, the LPF successfully reduced the noise (the fluctuations) in the DIC strain measurements.

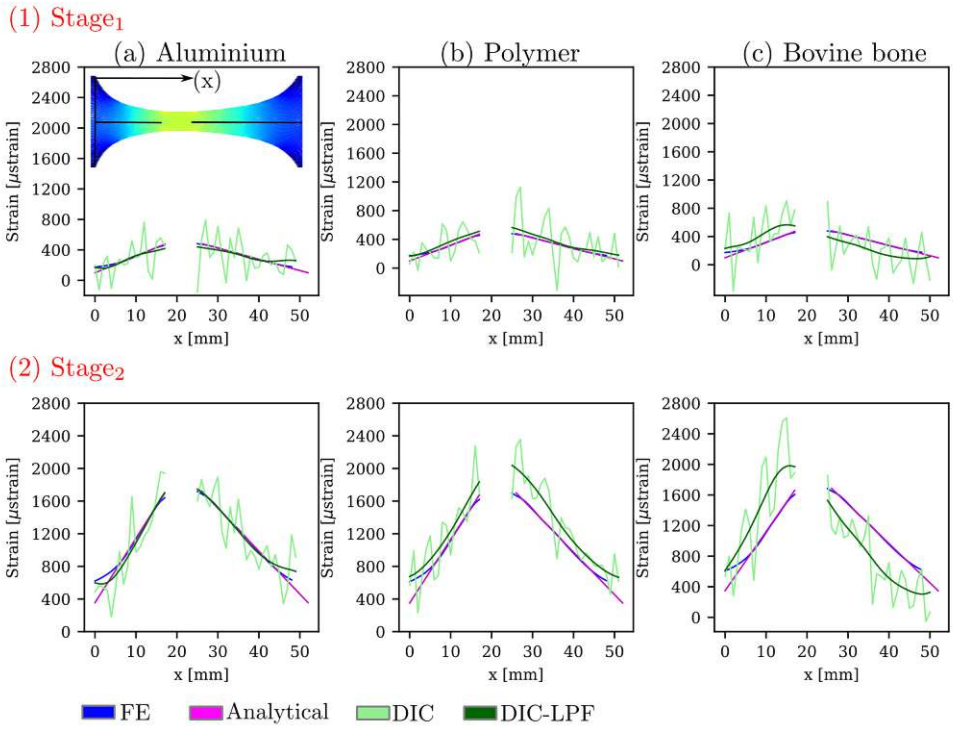

Figure 5.7: Full-Field linear strains at the two deformation stages, for (a) aluminium, (b) polymer, and (c) bovine bone. The strain is plotted along the specimen's ROI (53 mm), the strain was obtained from the high- and low-gradient ROIs, as in Figure 5.6(a4 and b4). The FE, analytical, DIC and DIC filtered strain are plotted in blue, magenta, light-green and dark green, respectively. DIC-LPF refers to the DIC strain fields after Gaussian LPF was applied.

Figure 5.8 depicts the RMSE for the linear strain gradients ROIs at Stage_1 and Stage_2 for the three tested materials. The $\text{RMSE}_{\text{analytical}}$ deviated by less than 60 μstrain from the reference FE strain for all the tested materials. The RMSE_{DIC} was about 400 μstrain when compared with the FE strain. Filtering of the DIC fields had a positive effect on the RMSE where it was reduced on average by 63% at Stage_1 and by 34% at Stage_2.

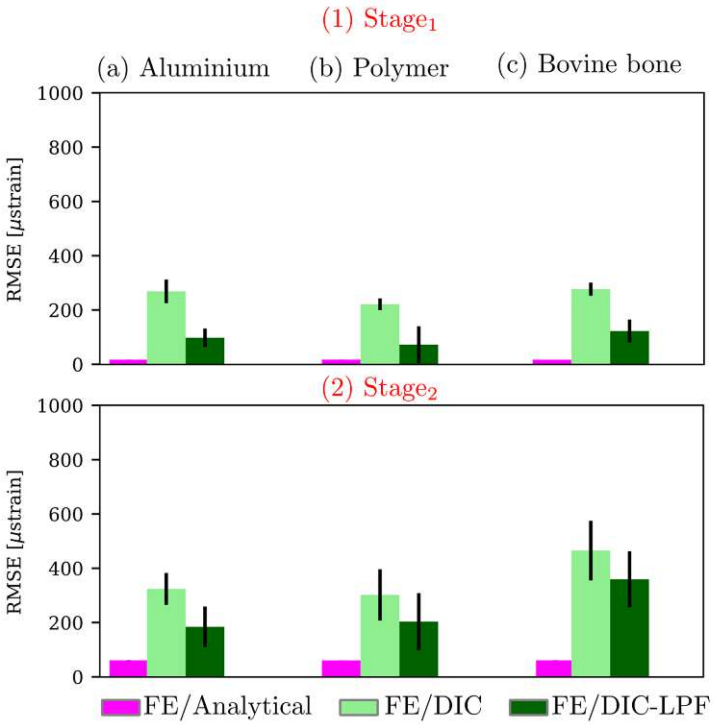

Figure 5.8: RMSE for the linear strain gradients ROIs at the two deformation stages for the three tested materials.

Two-dimensional visualization of the full-field strains from FE and DIC are depicted in Figure 5.9 for (a) one polymer and (b) one bovine bone specimens (The results of all the tested specimens are shown in Appendix Figure 5.10). Linear changes in the strain field cannot be recognized at Stage$_1$. On the contrary, at Stage$_2$, the linear strain field can be recognized, but corrupted with noise, which was then reduced when Gaussian LPF was applied. It is worth noting that the DIC strain fields shown in Figure 5.9 are the raw data from the ARAMIS software without the application of any filtering, neither when the surface component was created, nor when the strain was calculated. The DIC-LPF fields are the DIC fields after the application of the Gaussian LPF using an in-house algorithm.

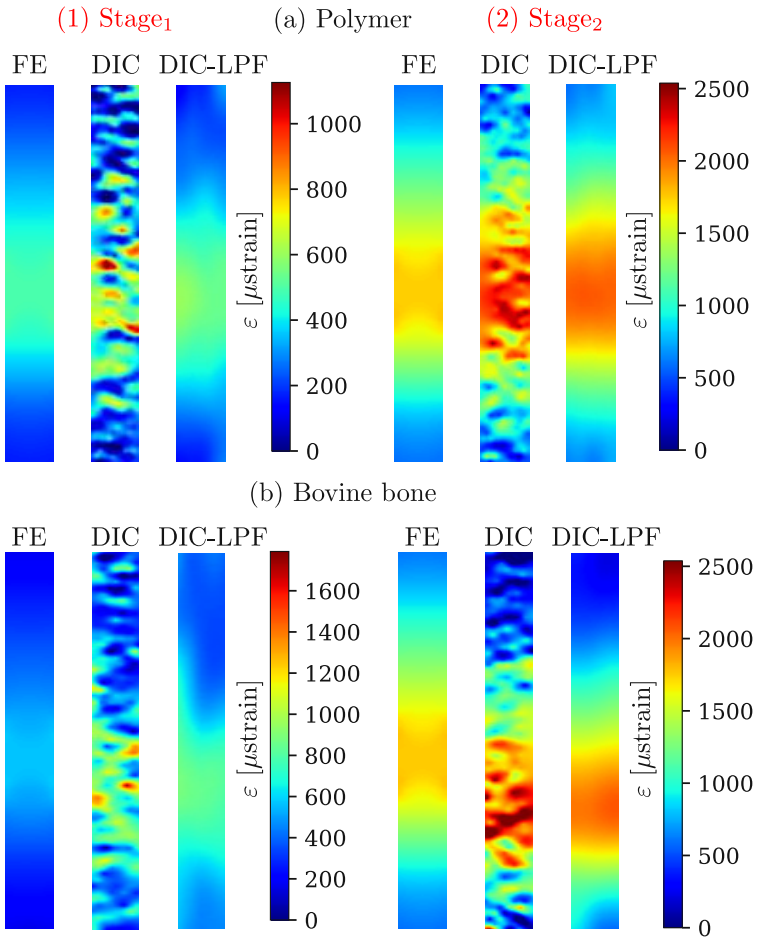

Figure 5.9: Two-dimensional visualization of the DIC full-field strain measurements of one polymer and one bovine bone specimens. At both deformation stages; the reference strain from the FE model for this specific specimen, the DIC strains (original and filtered) are shown.

Full-field FE reference strain and DIC (original and filtered) full-field strain measurements are shown in Figure 5.10.

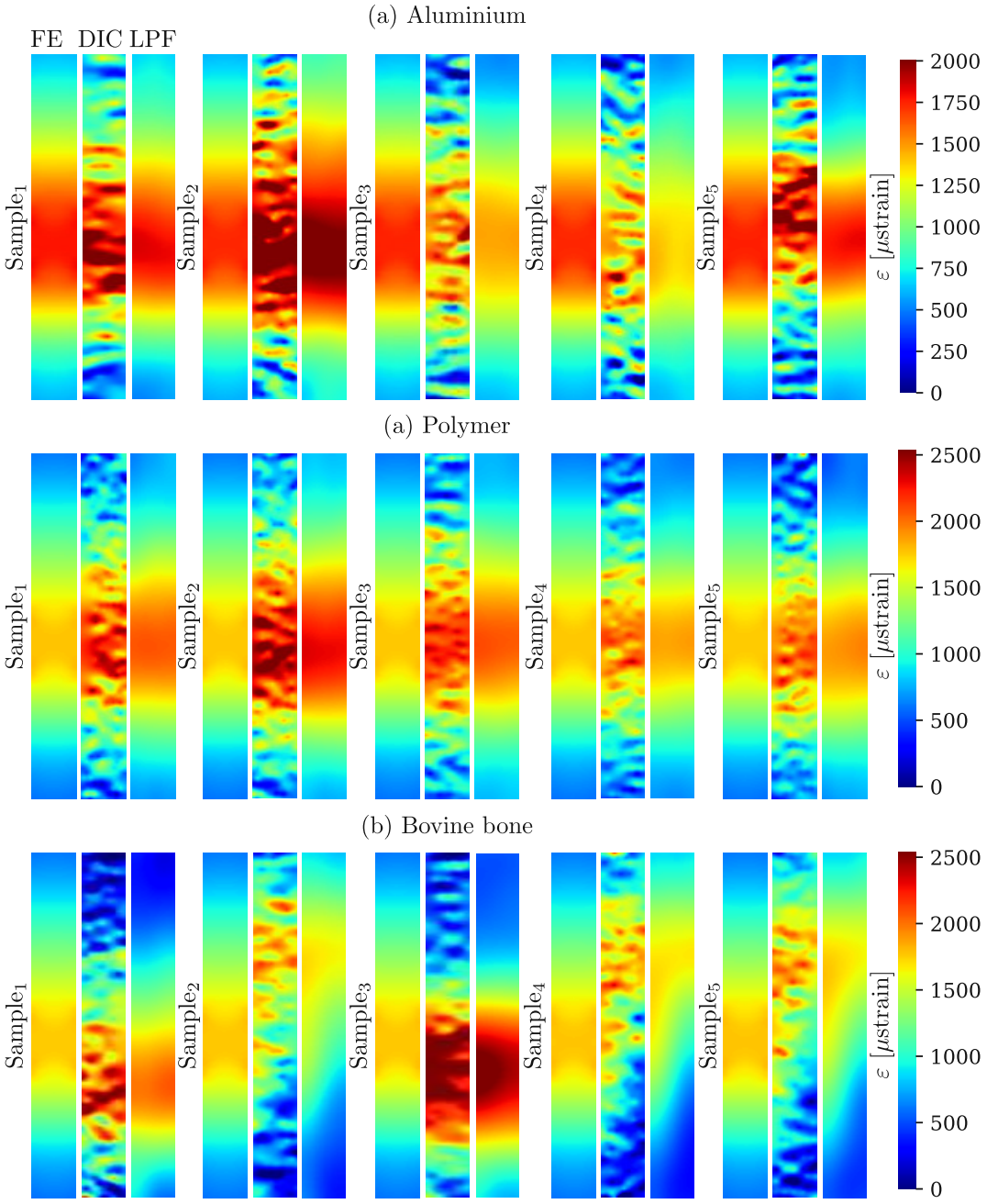

Figure 5.10: 2D visualization of the DIC full-field strain measurements of all tested specimens. At Stage_2; the reference strain from the FE model, the DIC strains (original and filtered) are shown.

5.5.3 Normalized strain gradient at strain gauges ROIs.

At the positions of the strain gauges, the corresponding FE and DIC strains were cropped as shown in Figure 5.5(a5 and b5). Figure 5.11 shows the normalized strain gradient at the positions of SG1 (6.9% per mm) and SG3 (3.6% per mm).

At SG1 (high-gradient), the DIC normalized strain gradient fails severely (with maximum difference to 6.9% per mm exceeding 90%) at Stage_1 and fails moderately (with maximum difference to the reference of 25%) at Stage_2. After applying the Gaussian LPF (depicted in dark green), the normalized strain gradients were successfully retrieved for most of the cases (maximum difference is 20% for aluminium and bovine bone).

In contrast, at SG3 (low-gradient), the average DIC normalized strain gradient and the standard deviation were closer to the reference strain for Stage_1 and Stage_2, except for bovine bone at Stage_1. As well, Gaussian LPF improved the detection of the normalized strain gradients (with maximum difference to the reference of 12%).

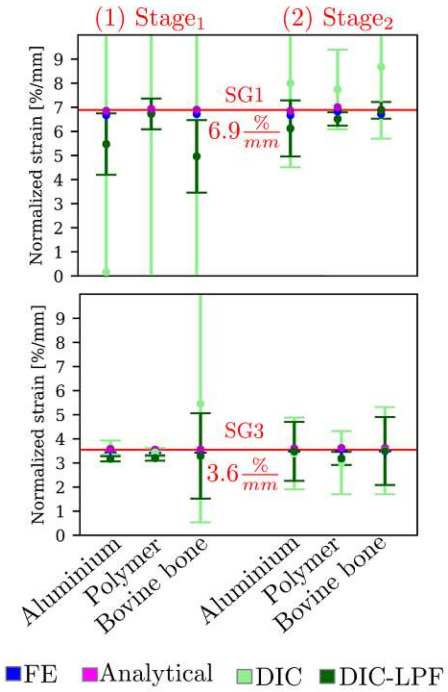

Figure 5.11: The normalized strain gradients at SG1 (6.9% per mm) and SG3 (3.6% per mm) is plotted for two deformation stages for aluminium, polymer, and bovine bone. The normalized strain gradient was calculated according to Equation (5.2).

Finally, the two experimental strain measurements obtained from DIC and strain gauges were compared. Table 5.3 lists the average strain obtained from DIC (at the strain gauge's position) and the strain gauge's recorded strain at Stage$_1$ and Stage$_2$. The average of the standard deviations exceeded 50% for DIC measurements at Stage$_1$ where the signal-to-noise ratio is lowest. One aluminium sample had a very low reading of SG1 at Stage$_1$ which resulted in a high standard deviation. A paired-specimens t-test ($\alpha = 0.05$) was conducted to compare the strain recorded by the strain gauges and their average corresponding area from DIC. For the majority of the measurements, no significant difference was found between the strain gauges and the DIC measurements (Statistical summary of the Shapiro-wilk and the t-test can be found in Appendix Table 5.4 and 5.5,). Additionally, the precision of the DIC strain measurement did not change largely and remained between 190 µstrain and 360 µstrain for the different deformation stages.

Table 5.3: Average strain measurements ± standard deviation for the DIC and strain gauges at the three strain gauges' positions. All listed values are in µstrain. The standard deviation for the DIC measurements is the average of the different standard deviations for the measured specimens. * indicates a significance difference in the mean.

SG	Stage	Aluminium		Polymer		Bovine bone	
		SG	DIC	SG	DIC	SG	DIC
SG1		217±215	314±193	358±32	260±143	440±115	298±229
SG2	$Stage_1$	494±7	484±270	497±5	496±172	489±3	544±302
SG3		369±62	459±280	416±54	376±214	472±69	429±203
SG1		979±398	1055±252	1224±106	1212±236	1329±399	1058±362
SG2	$Stage_2$	1748±16	1764±224	1743±6	2157±186*	1745±5	1774±276
SG3		1306±147	1503±247	1438±162	1594±227	1775±88	1513±187

Statistical summary of the normality shapiro-wilk test and paired t-test for $Stage_1$ and $Stage_2$ are listed in Supplementary Table 5.4 and 5.5, respectively. In the majority of the cases the specimens were normally distributed and no significant difference in the means were found between the DIC averaged strain and the strain gauges readings.

Table 5.4: Statistical analysis of strain gauges and DIC data at $Stage_1$. The p value is listed for both the Shapiro-Wilk test and the t-test for normality and different means, respectively.

Material	**SG**	**Shapiro-Wilk test**		**t-test**
		SG	**DIC**	
Aluminium	SG1	0.392	0.107	0.480
	SG2	0.593	0.971	0.912
	SG3	0.311	0.99	0.307
Polymer	SG1	0.479	0.203	0.116
	SG2	0.842	0.172	0.981
	SG3	0.308	0.324	0.595
Bovine bone	SG1	0.133	0.635	0.448
	SG2	0.982	0.99	0.446
	SG3	0.131	0.970	0.602

Table 5.5: Statistical analysis of strain gauges and DIC data at $Stage_2$. The p value is listed for both the Shapiro-Wilk test and the t-test for normality and different means, respectively. * indicates a significant difference.

Material	**SG**	**Shapiro-Wilk test**		**t-test**
		SG	**DIC**	
Aluminium	SG1	0.970	0.148	0.771
	SG2	0.234	0.344	0.925
	SG3	0.278	0.993	0.264
Polymer	SG1	0.084	0.205	0.812
	SG2	0.691	0.621	0.006*
	SG3	0.618	0.987	0.264
Bovine bone	SG1	0.043*	0.467	0.509
	SG2	0.213	0.375	0.906
	SG3	0.967	0.110	0.212

5.6 Discussion

The main goals of this study were to examine the capability of a 3D DIC system to measure a linear strain field on the surface of a newly designed gradient test specimen, with and without filtering.

Two strain measurement (strain gauges and DIC) and two strain computational (analytical and FE) methods were employed in this study. The RMSE was evaluated for the high- and low-gradient ROIs at two deformation stages, and the gradient was verified by a newly defined normalized strain gradient measure.

Due to the noise in the DIC strain measurement, the DIC strain deviated ($RMSE_{DIC}$ < 500 μstrain) from the FE strain - the gold standard in this study - for both the high- and low-gradient ROIs. Gaussian LPF successfully reduced the noise in the DIC full-field strain measurements for all the tested materials. However, the overall reduction in noise can be seen as reduction of the fluctuations of each field rather than reducing the overall measurement values. At $Stage_1$ and $Stage_2$, the $RMSE_{DIC}$ was reduced on average by 63% and 34%, respectively. In total, filtering reduced the RMSE to less than 200 μstrain which is in line with values reported in the literature [91, 130, 13, 85].

The main interest in this work is to examine the capability of DIC to measure strain gradients. For this, two engineering materials, stiffer (aluminium) and softer (polymer) than bone, were chosen for this investigation. At the location of high normalized strain gradient (6.9% per mm), only with applying Gaussian LPF the normalized strain gradient was retrieved. In contrast, at the location of low normalized strain gradient (3.6% per mm), the normalized strain gradient was measured accurately for all cases except for bovine bone, which was then improved when the LPF was applied. The normalized strain gradient is an indicator for how good can the DIC strain measurements measure local variation in the strain fields. In the examined cases, the accuracy of such a value was demonstrated to be higher for low strain concentrations. This can be helpful for measuring strain

concentration on the surface of the human femur. However, one should be aware that to decide whether such a value is accurately measured or not, a reference value or an idea of the strain concentration must be known.

Taking a closer look at these analyses, one could look at the DIC full-field strain measurements (see Figure 5.10). Linear strain fields were not recognized on the surface of all tested specimens. For engineering materials, the deviation from the reference FE was less evident than for the bovine bone specimens, where shifts in the linear strain fields were observed. These shifts can be attributed to the local variations of material and structural properties of bone i.e. the orthotropy of the material or the bone texture. During bone specimen preparation, pores (holes) were visible under the light microscope on the test surface. These holes, originated from blood vessels canals or trabecular bone, influenced the DIC measurements. It might be helpful to reduce the surface roughness by grinding the specimens, however, with grinding, pores might disappear or increase in size and new pores might appear. The inhomogeneity in the measured strain on bone surface was detected by Grassi et al. [28] who showed that DIC measured strain localization in proximity of cortical pores of the proximal femur. As well as Katz et al. [24] who showed that holes affected the strain pattern in the DIC measurements and that FE models should consider these holes. This inhomogeneity in the material besides the anisotropic nature of bone contributed to the variations in the DIC strain measurements. It would be useful for future studies to include pores in the FE analysis or create FE models based on geometries obtained from scanned specimens.

There was no significant difference in means between the averaged DIC strain measurement over the strain gauge's locations and the strain gauges strain for the majority of the cases. However, no significant difference does not necessarily mean accurate, no clear over- or underestimation were recognized of the DIC measurements. Similar results were found in the literature that validated DIC measurements with strain gauges or FE models [91, 87, 14, 15]. All these studies suggest that DIC strain measurement should be examined for accuracy. It is obvious that non-consistent errors were found in the DIC measurements, which empathizes the need for validation and optimization to maintain the error at minimum levels.

In summary, this study provided an unprecedented insight into the measurement accuracy of linear strain fields on the surface of different materials by means of DIC. A new innovative specimen shape with two gradients was presented which can be further developed and adapted for different strain gradients and tests with different DIC systems. With the normalized strain gradient, it was possible to measure and verify local strain concentrations, which are due to the specimen shape their magnitude were known a priori. This study showed that DIC systems can be optimized for inhomogeneous strain fields, such as strains found on the surface of many biological tissues and structures. The normalized strain gradient is essential to understand the range of strain changes per unit mm on the surface of bone. Finally, the common practice of averaging the strain measured on bone surface is not optimal, since many strain concentration locations get homogenized.

Limitations of this study are, only one facet and grid size were used as recommended by the DIC software, changing the facet and the grid size to smaller ones would definitely increase the density of the DIC measured points, but at the cost of more noise [70, 130, 127, 15]. Optimal filter parameter found in our previous study [133] was applied, however, other filter strategies might be useful to reduce the error in DIC strain measurements such as pre-filtering of the speckled images [30, 37]. Finally, the strain gradients values were evaluated for one human proximal femur at physiological load, it might be useful to evaluate strain concatenations beyond the physiological load.

5.7 Conclusion

The normalized strain gradient found on the proximal femur under physiological load was the basis for designing the specimens tested in this work. It was possible to capture such gradients with DIC. Gaussian low-pass filtering reduced the noise found in the DIC measurements and highly improved the detection of the normalized strain gradients. The outcome was better for 1) a lower normalized strain gradient, 2) higher strain level, 3) engineering materials. Beside this finding, the study

provides a new specimen design and methodological approach for investigating inhomogeneous full-field strains with DIC on engineering but also hard biological tissues like bone.

CHAPTER 6

High-resolution local trabecular strain within trabecular structure

6.1 Related publications and declaration of contributions

Results of the presented work (text, tables, figures) were *published* in the 'Journal of the Mechanical Behavior of Biomedical Materials' in 2024, entitled 'High-resolution local trabecular strain within trabecular structure under cyclic loading', and co-authored by D. H. Pahr.

Authors contribution The first author and the author of this thesis, *Nedaa Amraish*, conceptualized the methodology, wrote the manuscript, performed the experiments, data analysis and interpretation. *D. H. Pahr* supervised the work of Nedaa Amraish and supported the interpretation of the results.

In the previous chapter it was shown that DIC can with relative accuracy measure experimental linear gradient strain fields on engineering and biological samples at the macroscopic scale making it possible to explore the potential of DIC in

measuring strain states and fields at the microscopic scale. For this trabeculae within their trabecular structure are tested.

6.2 Introduction

Trabecular bone is the primary load-carrying component in the human skeleton [74]. Due to bone remodelling and diseases, this porous material loses density and connectivity, which leads to a reduction in strength [159, 160, 49, 161, 151]. With decreased volume, the strength gets decreased dramatically due to the relation between trabecular density and strength, which is governed by the power law [162]. Bone volume to total volume (BV/TV) and degree of anisotropy are among the most commonly quantified parameters in trabecular studies. Various studies examined the relation between bone material properties and bone density or BV/TV. For example, Stauber et al. [163] found that BV/TV is the best single predictor for Young's modulus and can explain 89% of the variance in Young's modulus. This strong correlation between bone material properties or strength and density was confirmed in other studies as well [164, 165, 166, 167, 168, 169, 170]. Despite the strong correlation, bone density is a poor predictor for patient-specific bone strength [159, 171, 172, 52] or for fracture sites [173, 174, 175, 52]. Individual trabeculae are usually divided into rods and plates in the trabecular network [40, 41]. Local morphometry factors such as trabecular thickness and trabecular separation contribute substantially to the mechanical properties of trabecular bone, showing the importance of local analysis of individual trabecula.

The reduction in BV/TV is simply a thinning of many trabeculae within a trabecular network. This thinning in the dimension of the trabecula leads to a higher slenderness ratio, which could cause the trabecula to fail under buckling if it reaches a critical value [176, 177, 178, 179]. Slenderness is the ratio between the length and the width or thickness of struts. It was confirmed that the slenderness of trabecular bone increases with age [180, 40, 181, 182]. Strain analysis is crucial to understanding the deformation of trabecular bone. Nonlinear Finite Element (FE) analyses showed that local yielding in the trabecular bone can occur even

at small apparent strains [183]. Not only does slenderness influence the strain response in trabeculae but also the orientation, since there are more longitudinal trabeculae than transverse trabeculae in a trabecular structure independent of the density [184], and longitudinal trabeculae are thinned more than the transverse trabeculae [185], which was confirmed as well by Fields et al. where they suggested that variation in vertebral strength is due primarily to variations in the bone volume fraction of longitudinal trabeculae [186].

Numerical methods, such as micro-FE, use high-resolution images of trabecular bone to create a 3D voxel grid from which mechanical properties can be computed. With this method, it is possible to obtain 3D stress and strain fields. However, a number of assumptions in the models influence the results, especially when voxels representing marrow are deleted [187], or when the whole trabecular structure gets assigned to elastic properties corresponding to a full-filled trabecular bone sample [188] or based on cortical bone [189, 161], or when different element types are used [189], making it difficult to accurately derive conclusions if no proper validation is done, which is challenging for trabecular bone at high local strains.

Two experimental methods were employed to measure local strain on trabecular bone. Digital image and volume correlation (DIC and DVC) are among the most used methods because of their contactless approach to measuring full-field strain. DVC allows for 3D full-field measurements, which is very beneficial to gaining in-depth measurements of the sample, while DIC can only deliver strain fields on the surface of the sample. Both methods rely on capturing images of samples under deformation. However, the accuracy and precision of both methods could be influenced, among other factors, by the resolution and the noise of the obtained images, the optimal way to reduce the noise of the image is by optimising the experimental setup such as light exposure, as it was confirmed that image filtering before strain computation has a counter effect of the accuracy of the strain fields [13]. Recently, Turunen et al. [46] used high resolution (voxel size of 3.6 $\times$ 3.6 $\times$ 3.6 μm^3) DVC images and confirmed that strain can be highly underestimated due to the resolution of the measurement device. As well, Fernandez et al. [190] applied DVC to trabecular bone with a pixel resolution of 6.5 µm, unfortunately, strain measurements were not obtained at the tissue level but at the whole trabecular

thickness. Despite the great advantages of DVC, x-ray radiation could influence the mechanical properties of bone specimens due to the required time to produce high-resolution images, which leads to dehydration of bone specimens. Frank et al. [76] found that dehydration of single trabecula results in increasing Young's modulus, yield stress, and failure stress by a factor of 2 and decreasing the failure strain by a factor of 3. Barth et al. [191, 192] reported that high exposures to synchrotron x-ray radiation caused a reduction in strength, ductility, and toughness of bone as a consequence of collagen matrix degradation.

On the other hand, DIC can obtain high-resolution images of bone in a considerably short time; the time of the mechanical test, but the results are limited to the surface of the specimen only. Acciaioli et al. [43] proved that it was possible to measure global 3D DIC strain on human cylindrical specimens (average length of 26 mm) obtained from distal femoral epiphyses. In this study, virtual DIC extensometer measurements were verified with a four-extensometer technique. However, in many studies (DVC and DIC) [170, 43, 79, 46], it was not possible to obtain full-field measurements of single trabecula within the trabecular network, except for Turunen et al. Various numerical studies [193, 194, 183, 172] showed local strain maps but lack experimental validation. Experimental studies at the tissue level [195, 196, 43, 79, 52] determined the material properties of trabecular bone, but lacked the determination of the local strain analysis. Moreover, experimental studies on single trabecula [49, 76] do not reflect the deformation of a single trabecula within the trabecular network.

Quantitative assessment of trabecular strain within the trabecular structure provides valuable insights for understanding the relationship between trabecular architecture and its response to external loads. The main objective of this study is to analyze the strain states (pure bending, tensile, compression, or a combination) of individual trabeculae within their trabecular structure. This involves assessing the longitudinal strain of the trabeculae at both the middle and near the edge regions. The second objective is to evaluate the local surface strain of trabeculae, enabling visualization of the heterogeneous strain distribution and allowing the computation of strain magnification between the globally applied strain and the locally resulting strain on the trabecular surface. Lastly, the third objective is to investigate the correlation

between longitudinal trabecular strain and the orientation and slenderness of the trabeculae.

6.3 Materials and methods

Trabecular bone specimens were cut from the distal femoral epiphyses of one bovine bone. First, a rough cut was performed to obtain bone slices parallel to the main axis of the femur. Second, using a low-speed diamond band saw (Exakt 300 CL Band System, EXAKT Advanced Technologies GmbH, Norderstedt, Germany), cubic specimens (n=4) were sliced (about $10 \times 10 \times 10$ mm^3), the exact dimensions of each specimen are listed in Tab. 6.1. Third, to clean and remove the bone marrow, the specimens were placed into an ultrasound device (Bandelin Sonorex, CarlRoth, Graz, Austria) at 30° C with water and a commercial soap (1:200) for about four hours. Bone specimens were kept wet with phosphate buffered-saline (PBS) solution during preparation and when not used, the specimens were preserved in a -20° C freezer.

Table 6.1: Width, length, and angle of each selected trabeculae of B1, B2, B3 and B4

Trabeculae	Width [mm]	Length [mm]	Angle[°]
B1 (10 × 10 mm^2)			
T1	0.14	0.62	29.39
T2	0.10	0.72	18.77
T3	0.21	1.5	12.43
T4	0.19	0.72	70.94
T5	0.20	0.94	1.11
T9	0.14	0.69	79.14
B2 (9.7 × 10 mm^2)			
T1	0.12	0.69	21.40
T2	0.12	0.82	0.00
T3	0.14	0.52	52.17
T5	0.16	0.62	2.82
T8	0.19	0.40	84.49
T12	0.24	0.66	66.32
B3 (11.9 × 10.5 mm^2)			
T2	0.21	0.60	25.25
T3	0.12	0.86	22.16
T4	0.16	1.1	19.95
T6	0.16	0.72	27.91
T8	0.12	0.41	27.59
T9	0.14	0.67	29.09
B4 (11 × 10.2 mm^2)			
T1	0.12	0.48	30.39
T3	0.22	0.61	34.44
T4	0.13	0.36	47.16
T5	0.09	0.45	5.91
T6	0.14	0.46	42.41
T8	0.14	0.71	80.65

An industrial camera (Mercury2 USB3.0, China) with a telecentric lens (LCM-TELECENTRIC-1X-WD110-1.1-NI, China) were used to capture images during the mechanical test, images were captured using a GigE software (Daheng Galaxy Viewer software), see Figure 6.2. The camera and lens specifications are listed in 6.2. Speckle patterns were applied on the surface of the specimens using a high precision airbrush (Profi-AirBrush, Germany) with the following settings; air

pressure of 450 kPa, 3 turns of the airbrush opening, and 15 cm distance between the airbrush and the specimen. The obtained images were evaluated using ARAMIS Professional software (v6.3.1; GOM GmbH, Germany). The optimal facet size was 25 × 25 pixels and the optimal step size was 15 pixels (distance between facets).

The noise was evaluated for the first stages at zero-load. To find the optimal facet and step size, different combinations of facet and step sizes were selected. Figure 6.1 shows that the least noise was measured for facet size of 25×25 pixels and step size of 15 pixels.

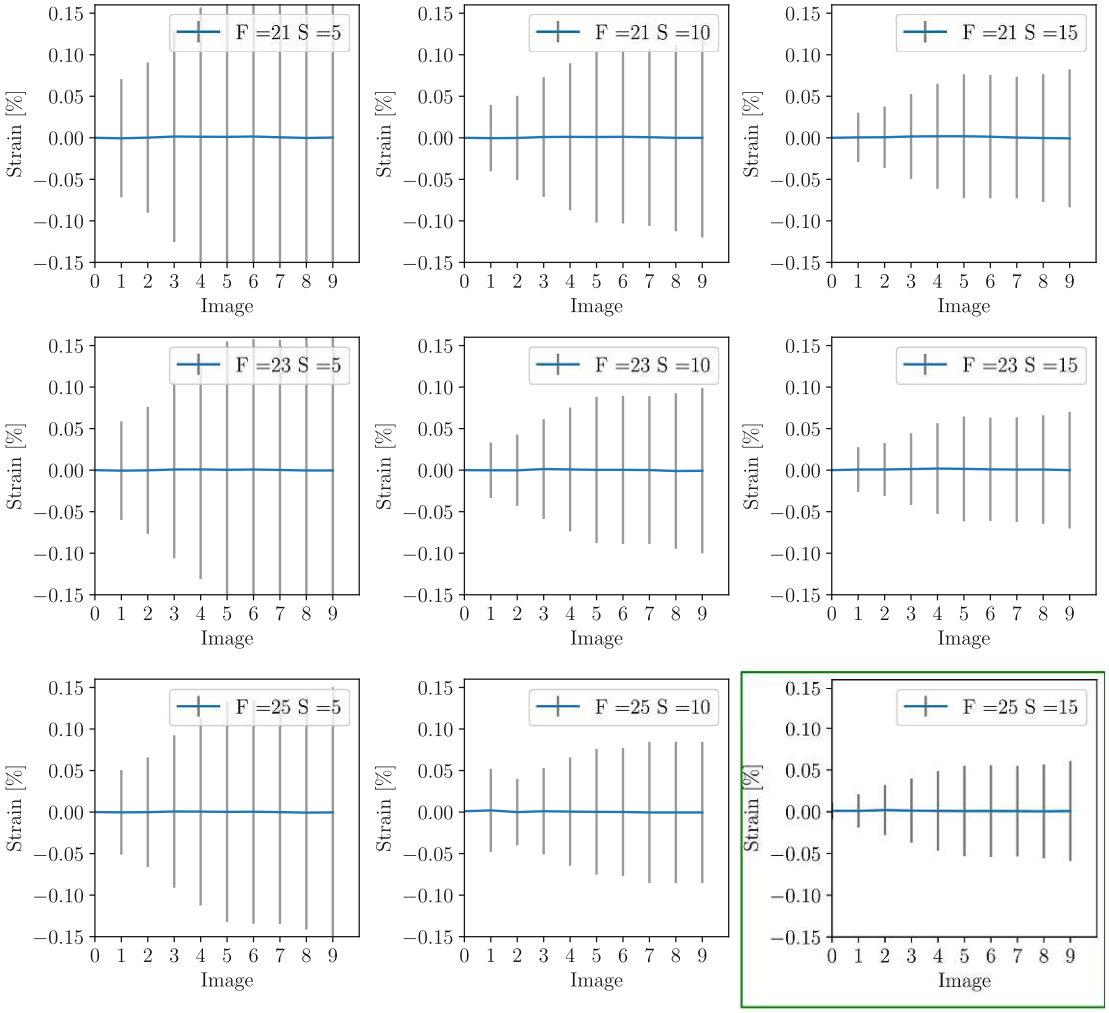

Figure 6.1: For different facet and step sizes, the zero-strain load was evaluated for one sample. Facet size of 25×25 pixels and step size of 15 pixels show the lowest noise.

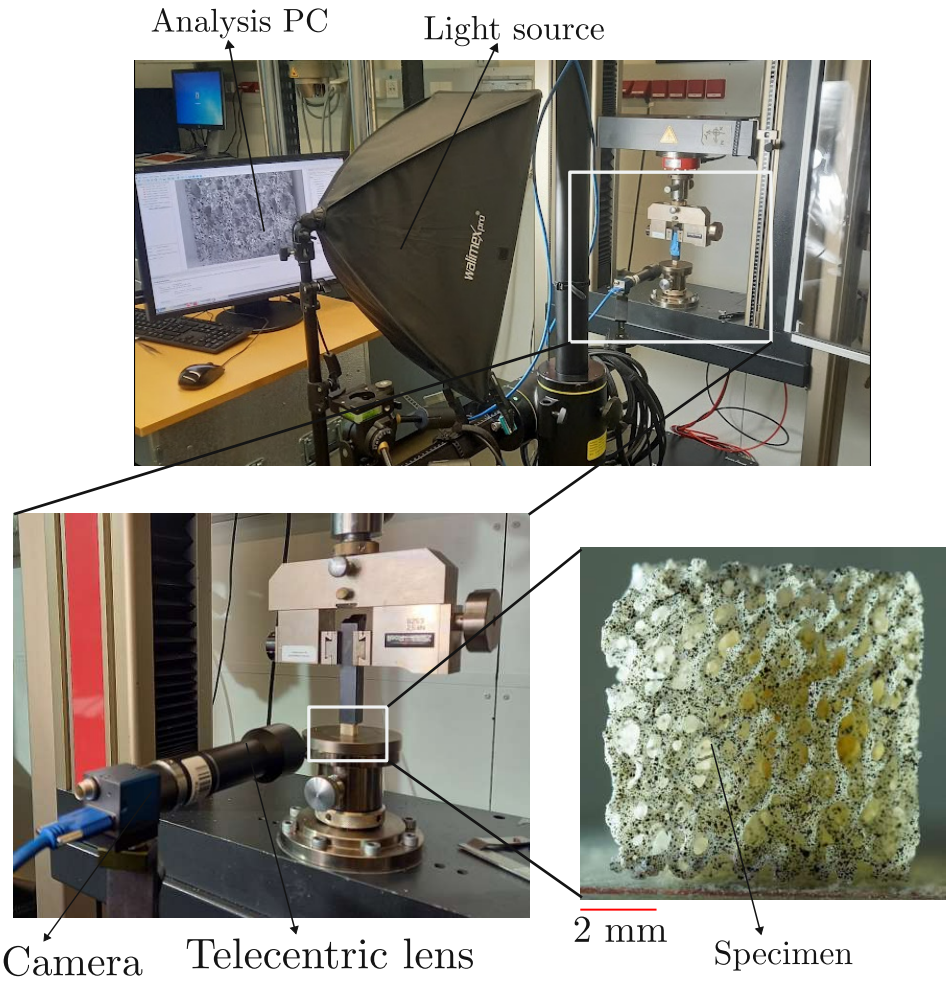

Figure 6.2: Mechanical testing setup. A camera with a telecentric lens was employed to capture images during specimen's deformation, the camera was connected to a computer for image visualization. The specimen was carefully placed and aliened perpendicular to the lens plane. A light source was used to illuminate the specimen. On the right, a speckled specimen ready for testing is shown.

Table 6.2: Specification of the telecentric lens system.

Specification	**Value**
Lens	LCM-TELECENTRIC-1X-WD110-1.1-NI
Camera type and sensor	MER2-2000-19U3M
Camera sensor	Sony IMX183
Shutter time	12 µs
Camera resolution	5496 × 3672 Pixels
Image resolution	2.4 μm
Scale factor	416 Pixel/mm
Working distance	110 mm
Magnification	x1
Aperture	F7
Analysis resolution	0.04 Pixel
Field of view	14.2×10.4 mm
Depth of field	± 0.3 mm

The specimens were subjected to a cyclic (ramp and hold) compression load using a Zwick Z030 machine (ZwickRoell GmbH, Germany). To test the accuracy of the measured strain, a sequence of at least five images was captured of each specimen at zero-strain. The cyclic compression test was applied by loading and unloading the specimen, where each phase was followed by a holding phase for five seconds for five cycles; by reaching the fifth cycle, the displacement of the loading plate was 0.7 mm. Figure 6.3 shows the testing protocol of one specimen. This loading protocol was chosen because the bone is subjected to repetitive cyclic loading during daily activities, and the results can be examined in the hold phases.

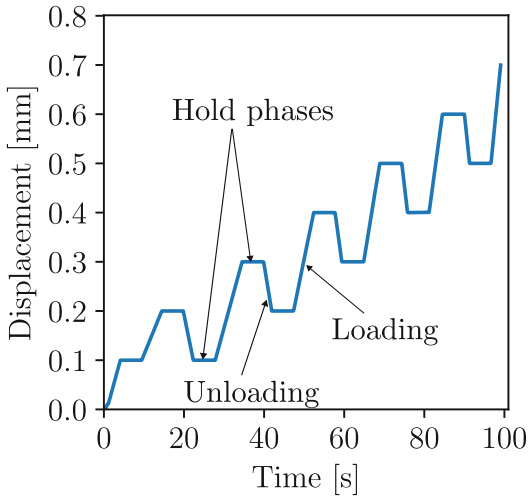

Figure 6.3: Mechanical test protocol: a cyclic ramp and hold compression test.

6.4 Data analysis

This study differentiated between three types of strain computations:

1. an average global sample strain $\overline{\varepsilon}_{\mathrm{G}}$, which is the engineering strain obtained from three virtual extensometers along the length of the sample.
2. three longitudinal trabecular strains; one in the middle $\varepsilon_{\mathrm{L1}}$ and two close to the edge of the trabeculae $\varepsilon_{\mathrm{L2}}$ and $\varepsilon_{\mathrm{L3}}$, which are computed as the length change of individual trabeculae divided by their original lengths.
3. a transformed local surface strain of trabeculae $\varepsilon_{y'}$, which is the facet-points strain transformed in the direction of the trabecular axis.

The first type of strain the average global sample strain was analyzed as following; for each specimen, three global sample strains were identified using virtual extensometers, as depicted in Figure 6.4, which shows three virtual extensometers (in black) created on the surface of one specimen. For each virtual extensometer, a facet and a direction (y-axis in this case) were defined in the reference stage. The facet must be a valid facet that could be traced along the deformation stages. If

the chosen facet was invalid because speckles could not be tracked (as shown in red in Figure 6.4), no extensometer could be created. The global sample strain ε_G was computed via the change in length of the virtual extensometer divided by its original length, engineering strain.

$$\varepsilon_G = \frac{dL}{L} \tag{6.1}$$

Since three virtual extensometers were created on the surface of each sample, the average of these three virtual extensometers, hereafter called average global sample strain $\overline{\varepsilon}_G$, was used for further analysis.

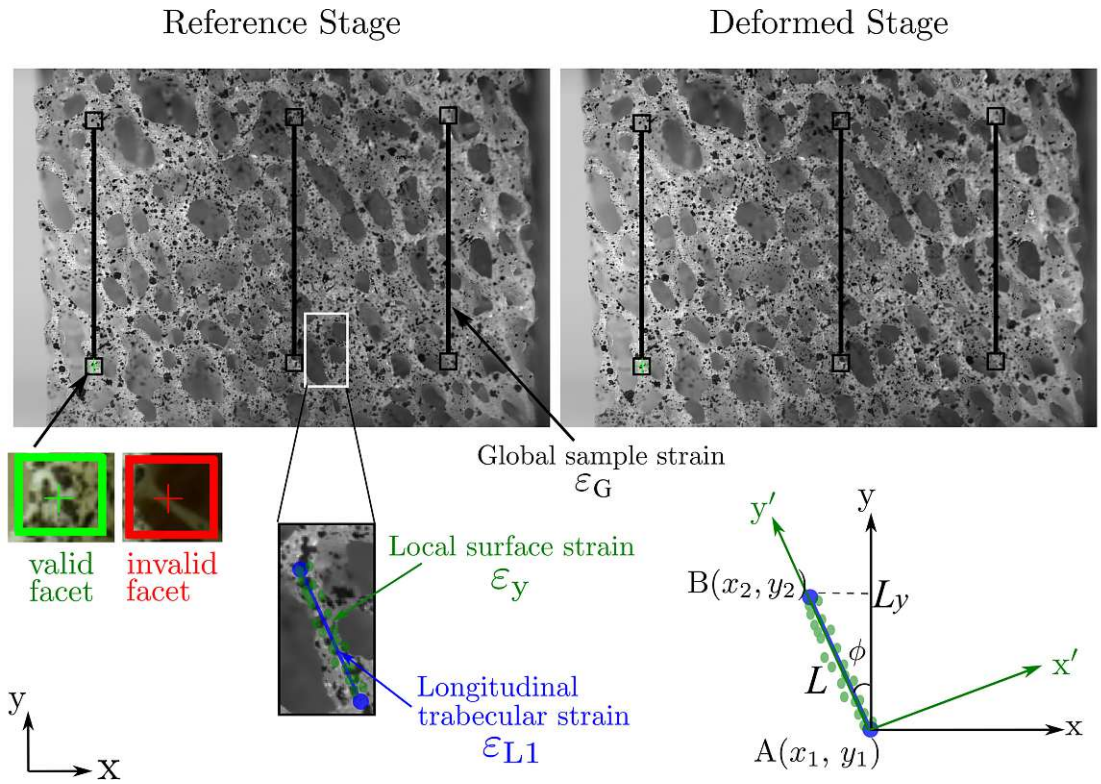

Figure 6.4: Strain analysis. The global sample strain ε_G (in black) was computed as the length change of the virtual extensometer divided by its original length. The longitudinal trabecular strain in the middle of the trabecula ε_{L1} was calculated as the length change of each trabecula divided by its original length (along $y^{'}$). Local surface strain of the trabecula ε_y is the facet-points strain of the surface in the $y-$direction, which was then transformed onto a new axis $y^{'}$ which is inclined from the original y-axes at an angle ϕ.

The second type of strain includes three longitudinal trabecular strains; one in the middle (in blue) ε_{L1} and two close to the edge of the trabeculae ε_{L2} (in red) and ε_{L3} (in green) as shown in Figure 6.5. ε_{L2} and ε_{L3} were used to investigate the bending states as they were created parallel and at an equal distance to the trabecula's length (blue in Figure 6.5).

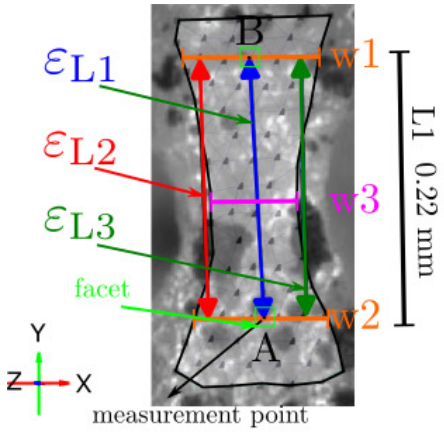

Figure 6.5: An example of how the trabecula's length and width were determined. First, after a surface component with facet size of 25 and step size of 15 was created covering the surface of the trabeculae, two distances (w1 and w2 in orange) were created at the extremities and close to the edge of each trabecula, these two distances were manually selected at the end of the gauge length of the trabecula and before the starting curvature. Second, a longitudinal distance was created (in blue) connecting the middle points of w1 and w2, which was used for computing the longitudinal trabecular strain ε_{L1}. And finally, a third horizontal normal distance w3 was created (in magenta). The width of the trabecula was calculated as the average of the three (w1, w2 and w3) normal distances. For the longitudinal trabecular strain close to the edge of the trabeculae, two additional longitudinal distances (in green and red) were created to investigate ε_{L2} and ε_{L3} close to the edge of the trabeculae.

In general, ε_{L1}, ε_{L2} and ε_{L3} were computed in the same manner. The length was determined by computing the trabecula's length L from the vector coordinates: $AB = (x_2 - x_1, y_2 - y_1)$ where $L = |AB|$, and the longitudinal trabecular strain was then computed as follows for each stage:

$$\varepsilon_L = \frac{L_{stage} - L}{L} \tag{6.2}$$

where L is the original length (in green, blue or red in Figure 6.5) at stage zero before loading and L_{stage} is the length after deformation.

The width of every single trabecula was determined at three locations; as shown in Figure 6.5 for w1, w2 and w3, the average of these three values $\overline{w}$ was taken as the

width of the trabecula. A detailed table of the dimensions of each trabecula can be found in 6.1. For each trabecula, the slenderness ratio λ was computed, which equals the length L of every single trabecula divided by its average width $\overline{w}$:

$$\lambda = \frac{L}{\overline{w}} \tag{6.3}$$

The third type of strain in this study is the transformed local surface strain of trabeculae. The local surface strains ε_y, ε_x, and ε_{xy} of the facet-points were computed in the global coordinate system [133]. Since trabeculae were inclined and deviated by an angle ϕ from the main loading axis (y-axis), a strain transformation was done as given in the following Eqn.:

$$\varepsilon_{y'} = \frac{\varepsilon_x + \varepsilon_y}{2} - \frac{\varepsilon_x - \varepsilon_y}{2}\cos(2\phi) - \varepsilon_{xy}\sin(2\phi) \tag{6.4}$$

$y^{'}$ is the longitudinal axis of the trabecula, $\varepsilon_{y'}$ is the local transformed (facet-point) strain, and ϕ is the angle at which a single trabecula deviated from the loading direction (y-axis), and it was computed by the inverse cosine of the ratio between the length of the trabecula in the y-direction L_y and the actual length of the trabecula L (see Figure 6.4).

$$\phi = \cos^{-1}\left(\frac{L_y}{L}\right) \tag{6.5}$$

The transformed local surface strain $\varepsilon_{y'}$ was averaged arithmetically over the length of the trabecula, between w1 and w2 as in Figure 6.5. This gives the average transformed local surface strain $\overline{\varepsilon}_{y'}$, which can be compared to the longitudinal trabecular strain $\varepsilon_{\mathrm{L1}}$.

For sensitivity analysis, five images were captured at zero-load, which were used to evaluate the sensitivity of the average global sample strain, the longitudinal trabecular strain, and the transformed local surface strain. Finally, a Gaussian filter was applied to smooth the strain signals with a standard deviation of the Gaussian function of 2.5 which was thoroughly investigated in our previous work [133, 197],

where further information on the influence of the filter size on the strain field can be found.

6.5 Results

6.5.1 Sensitivity of the DIC method

To assess the sensitivity of the DIC method, the strain deviation at zero-load was examined. The strain deviation for the average global sample strain $\overline{\varepsilon}_{\mathrm{G}}$ (in black) and the longitudinal trabecular strain $\varepsilon_{\mathrm{L1}}$ (in colours) is shown in Figure 6.6 for all test samples. The measured strain for both the longitudinal trabecular strain and the average global sample strain was less than 0.05%, with values of 0.03% and 0.01%, respectively.

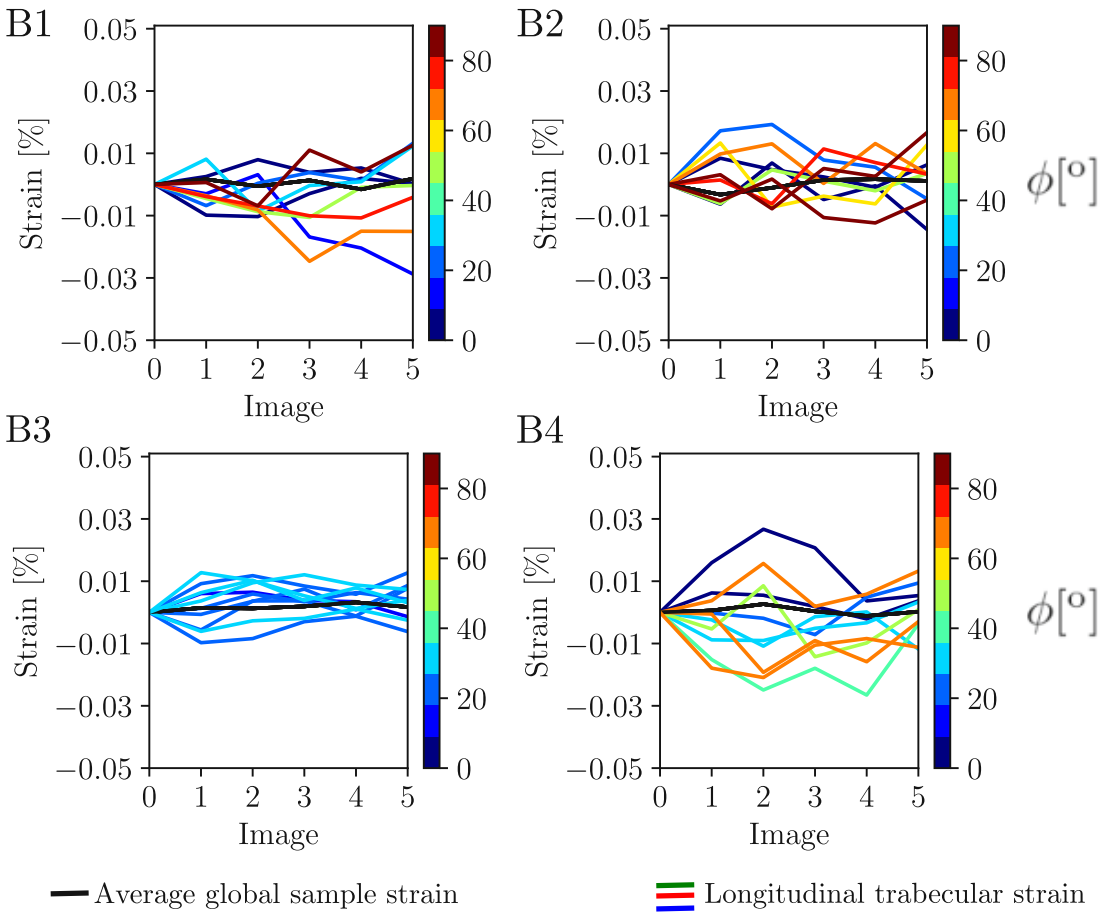

Figure 6.6: Strain sensitivity for the first five stages at zero-load. The longitudinal trabecular strain ε_{L1} (in colours) and the global sample strain (in solid black) for each specimen. Trabeculae are coloured, indicating the inclination angle ϕ [°] of the trabeculae from the main loading axis.

The longitudinal trabecular strain ε_{L1} was compared to the average transformed local surface strain $\overline{\varepsilon}_{y'}$ of the same trabecula. Figure 6.7(a) shows a very good agreement between both strains. However, this agreement was not observed for some trabeculae, as shown in Figure 6.7(b), due to non-aligned strains. Consequently, these trabeculae were excluded from the analysis. The number of measurement points along the width of the trabeculae ranged from 7 to 12 measurement points (facets).

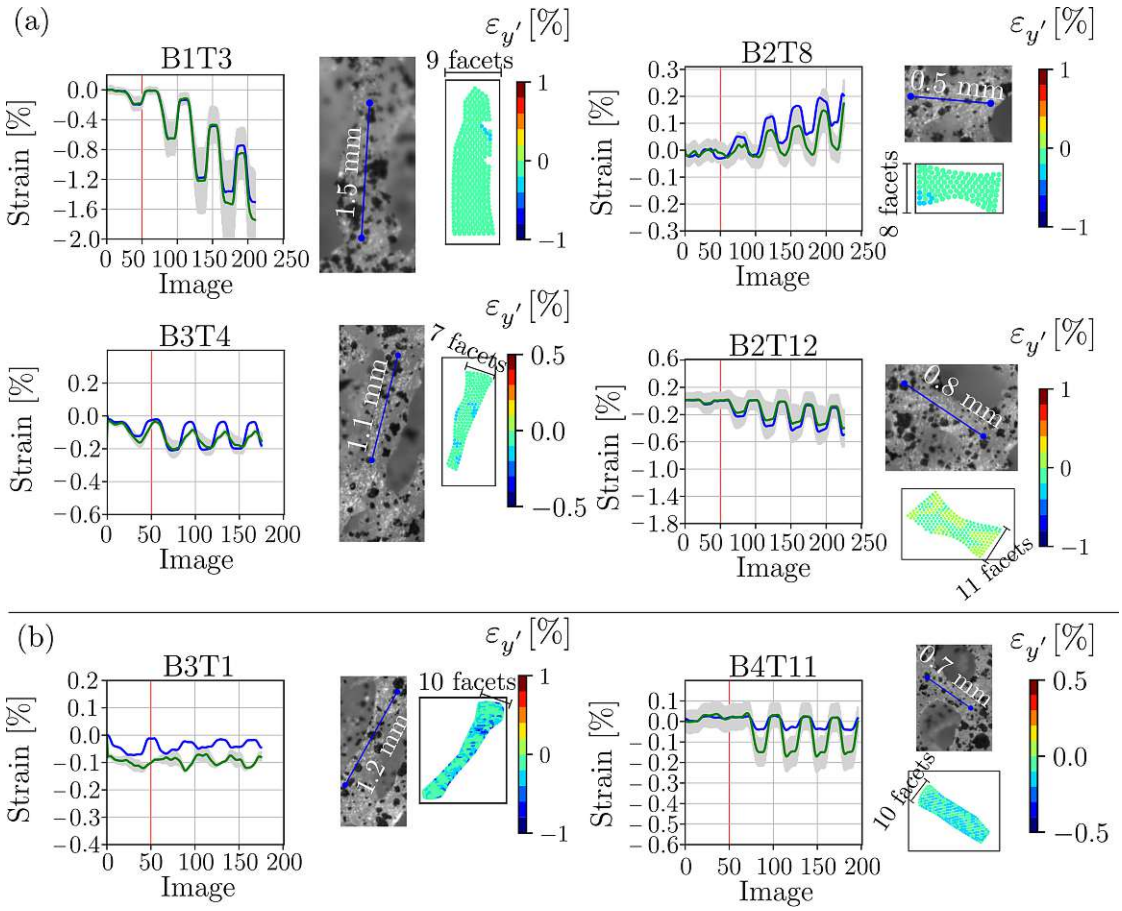

Figure 6.7: (a) Longitudinal trabecular strain ε_{L1} (in blue) and average transformed local strain $\overline{\varepsilon}_{y'}$ (in green). (b) non-matching strains for curved trabeculae. The colour bar on the side refers to the average transformed local (facet-points) strain $\varepsilon_{y'}$. Only trabeculae where the difference between both strain measurements is less then 20% were included in the analysis.

6.5.2 Longitudinal trabecular strains

Bending of trabeculae were investigated by measuring longitudinal trabecular strains ε_{L2} and ε_{L3} close to the edge of the surface of the trabecula which was compared to the longitudinal trabecular strains ε_{L1} along the middle of the trabecula. Figure 6.8 shows 8 trabeculae, each with three distances selected on its surface, where the blue distance is at an equidistant to the red and green distances. The differences between the left, right, and middle (in blue) longitudinal strains indicate bending inside

the trabeculae. The longitudinal strain plots show a pure compression (trabeculae a and b), and a bending (trabecula c, d, f, g, and h) state or mixed state of the trabecular strain. In case of a bending state, the strain magnification increases with increasing load and reaches, for the shown trabeculae, a maximum of 8-folds (trabecula d).

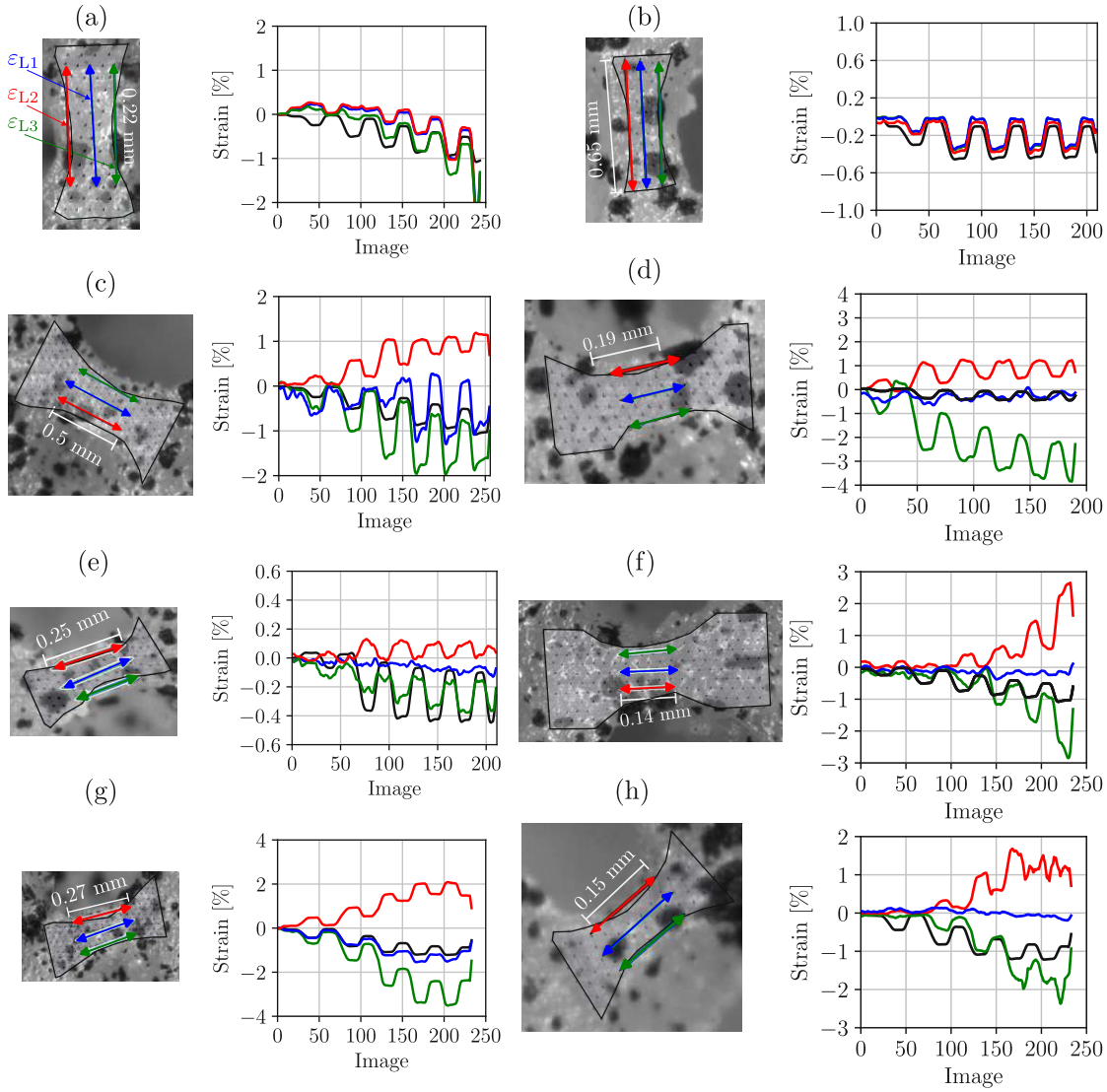

Figure 6.8: Longitudinal trabecular strain close to the edges of the trabeculae. Three distances in blue ε_{L1}, red ε_{L2}, and green ε_{L3} were created on the surface of the trabeculae. For each distance, a longitudinal trabecular strain was computed as per Eqn. 6.2, and plotted along the deformation stages.

6.5.3 Local transformed surface strain of trabeculae

Local full-field surface strain measurements were obtained for trabeculae on the surface of each of the four specimens. The figure below depicts selected trabeculae

of specimen B2 at two different loading steps (images 50 and 200 at 0.2 mm and 0.6 mm respectively). The local full-field strain, denoted as $\varepsilon_{y'}$ and was transformed according to Eqn.6.4, is superimposed on each specimen's surface. As the load increases, the heterogeneity of the deformation becomes more evident, with some trabeculae exhibiting tension and/or compression strain. Inclined trabeculae, such as B2T3, B2T8, and B2T12, displayed a bending state, while trabeculae aligned along the loading direction, as in B2T2 and B2T4, showed compression strain at the centre of the trabecula, which is thinner at this location in both cases. Finally, B2T1 displayed tensile strain. For full-field surface strain measurements of the other three specimens, please refer to6.5.3. The strain magnification increases with increasing load and reaches, for the shown trabeculae, a maximum of 8-folds (trabecula B2T2, B2T8, and B2T12), which is inline with strain values found in the literature, Morgan et al .[183].

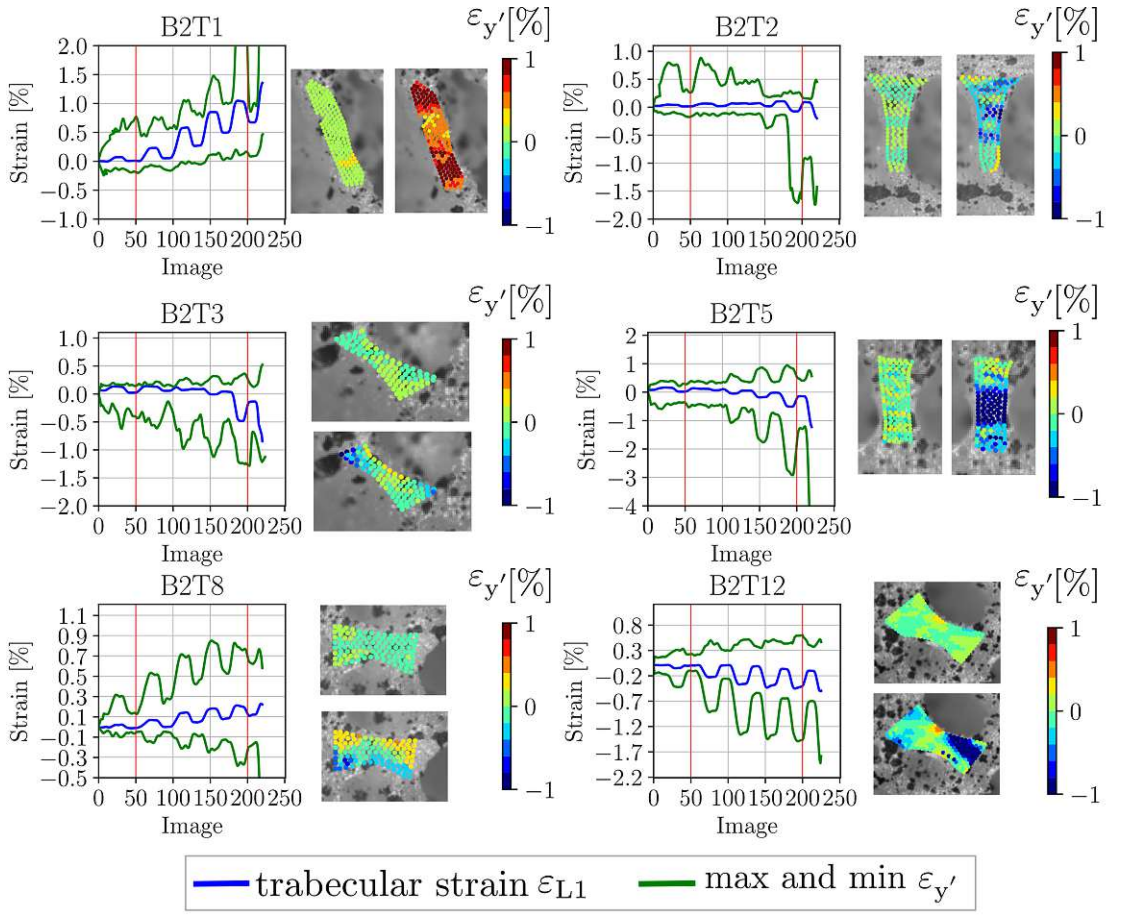

Figure 6.9: Local transformed full-field surface strain for six trabeculae in specimen B2. The blue line is the trabecular longitudinal strain ε_{L1}, and the green lines show the maximum and minimum of the local surface strain $\varepsilon_{y'}$ of the trabeculae. The local transformed full-field surface strain showed at least four and nine measurement points across the width of the trabeculae, for width of at least 0.12 mm and 0.24 mm, respectively.

Similar to specimen B2, in B1, increasing load caused trabeculae to bend, resulting in strain concentration that exceeded the longitudinal strain of the trabeculae. Trabeculae B1T1 and B1T3 exhibited a bending state, with blue areas indicating softer locations that underwent more deformation compared to the rest of the trabecula. Here too, the strain magnification increases with increasing load and reaches a maximum of 4-folds (trabecula B1T4).

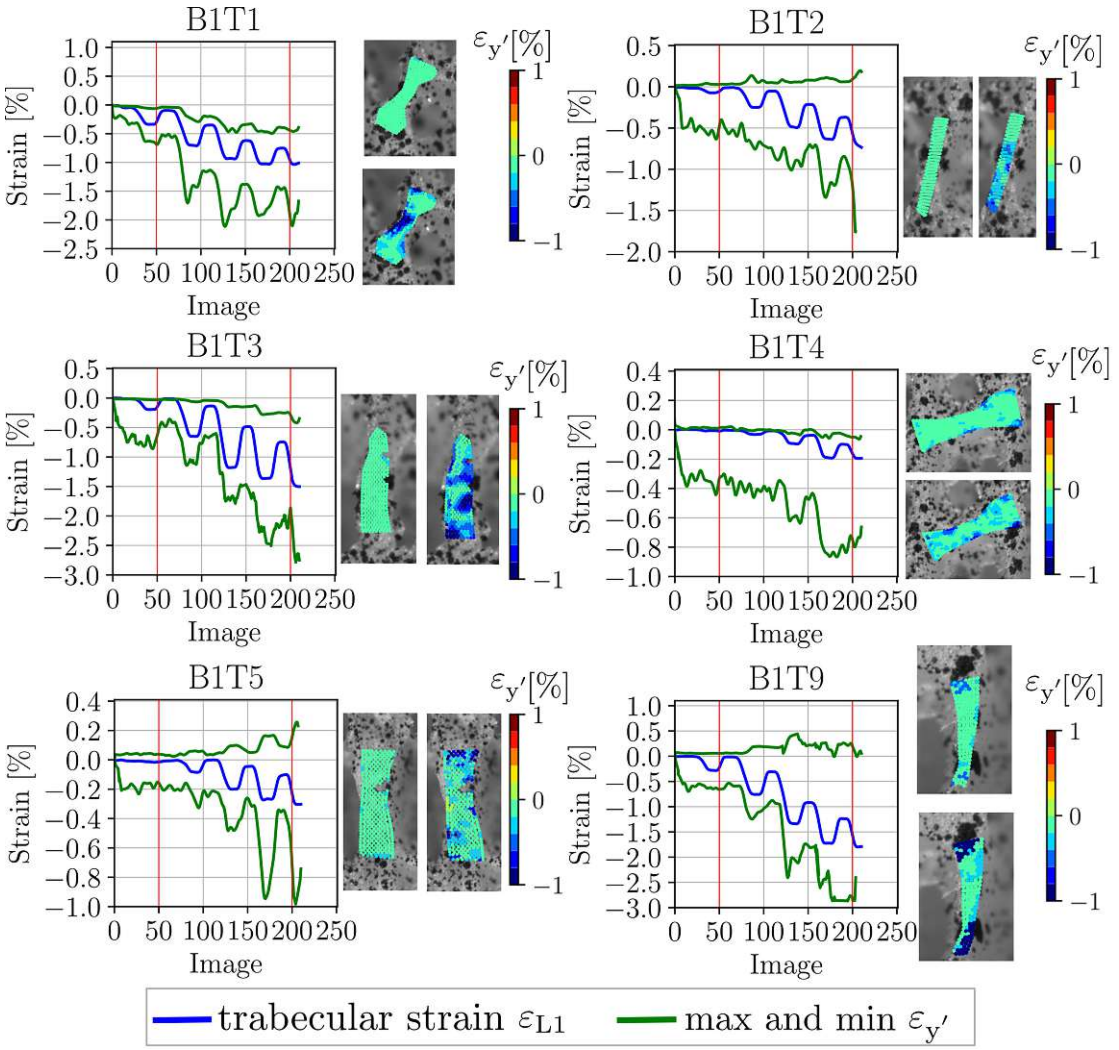

Figure 6.10: Local transformed full-field surface strain for six trabeculae in specimen B1. The blue line is the trabecular longitudinal strain ε_{L1}, and the green lines show the maximum and minimum of the local transformed surface strain $\varepsilon_{y'}$ of the trabeculae. The local transformed full-field surface strain showed at least four and nine measurement points across the width of the trabeculae, for width of at least 0.10 mm and 0.21 mm, respectively.

The figures below show the different selected trabeculae of the specimens B3 and B4. The full-field strain (transformed according to Eqn. 6.4) is superimposed on each of the trabecula's surface. The heterogeneity of the deformation can be seen, where some trabeculae show tension and/or compression strain.

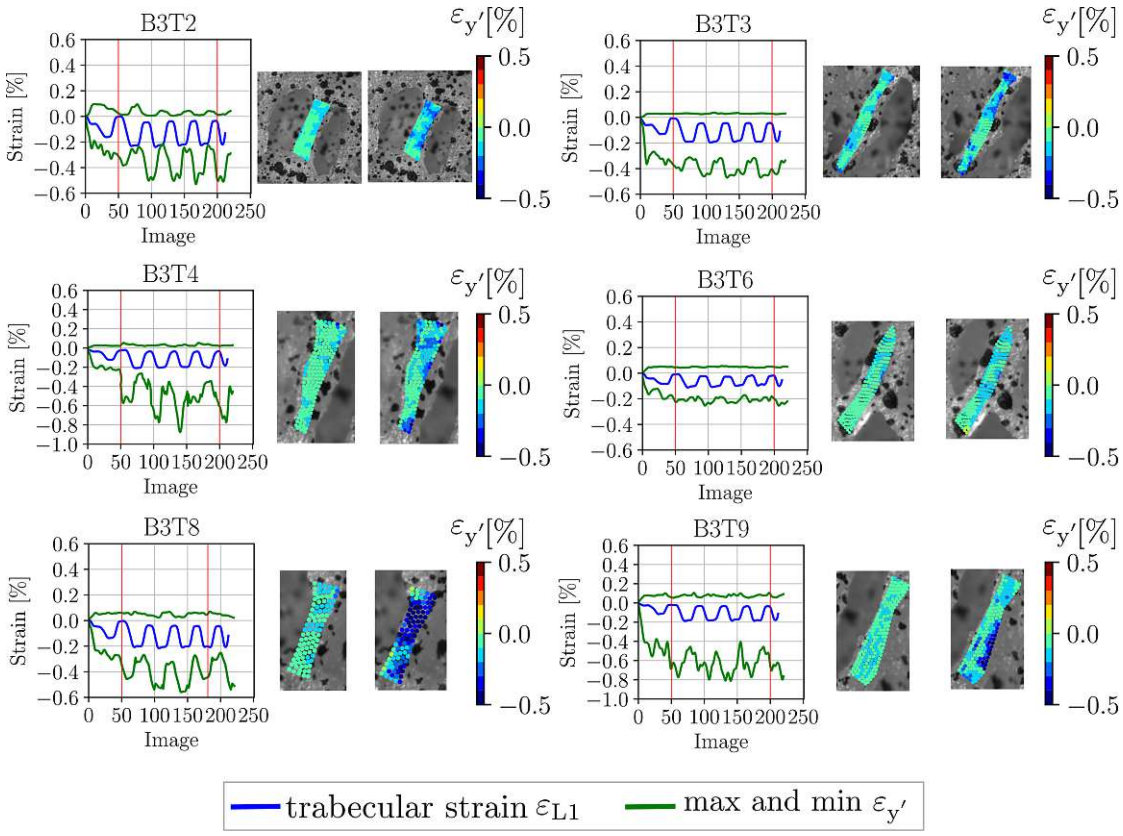

Figure 6.11: Local transformed full-field surface strain for six trabeculae in specimen B3. The blue line is the trabecular longitudinal strain ε_{L1}, and the green lines show the maximum and minimum of the local transformed surface strain $\varepsilon_{y'}$ of the trabeculae.

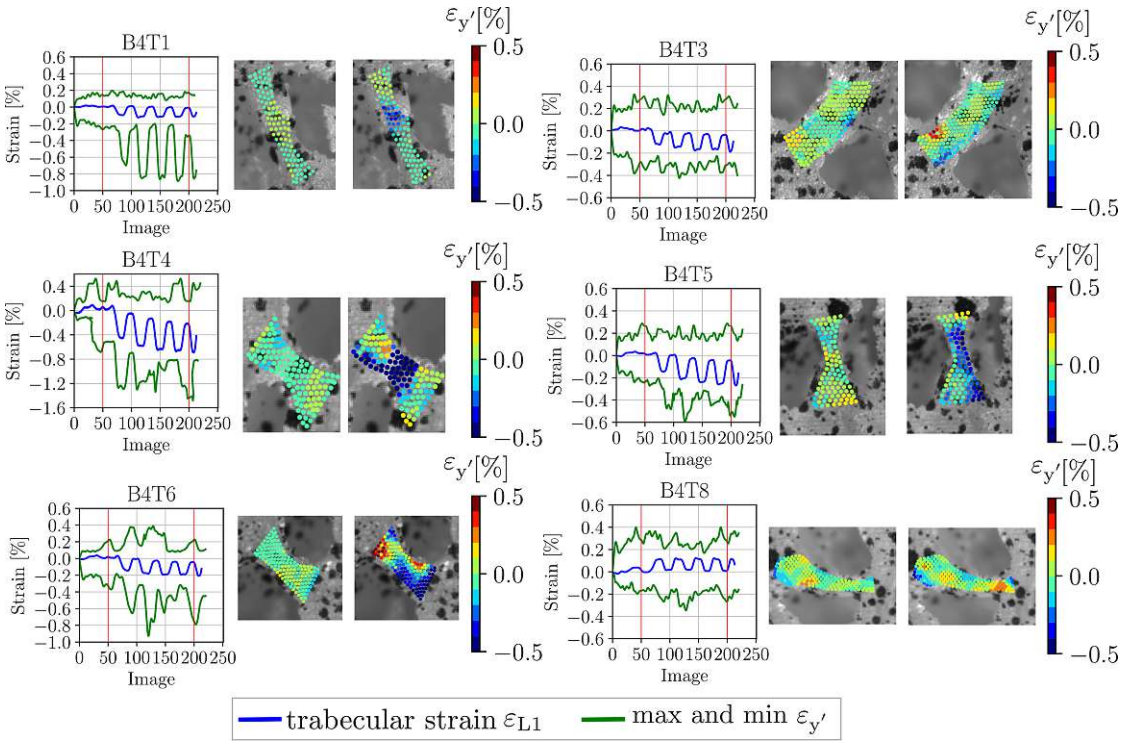

Figure 6.12: Local transformed full-field surface strain for six trabeculae in specimen B4. The blue line is the trabecular longitudinal strain ε_{L1}, and the green lines show the maximum and minimum of the local transformed surface strain $\varepsilon_{y'}$ of the trabeculae.

6.5.4 Correlation between orientation/slenderness and the longitudinal trabecular strain

Figure 6.13 shows the longitudinal trabecular strain values along the different (a) inclination angles and (b) slenderness ratios of the selected trabeculae. No significant correlation was found between the strain magnitude and the inclination angle or the slenderness ratio, $p = 0.302$ and 0.672, respectively.

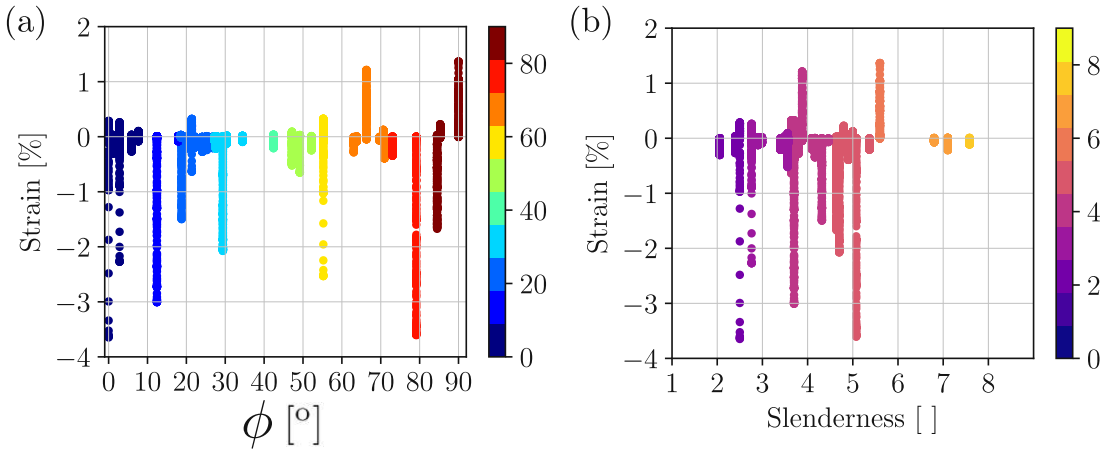

Figure 6.13: The longitudinal trabecular strain values along (a) the different inclination angles, and (b) the slenderness ratio of the selected trabeculae.

The figure below shows the longitudinal trabecular strains according to the slenderness ratio of each measured trabeculae.

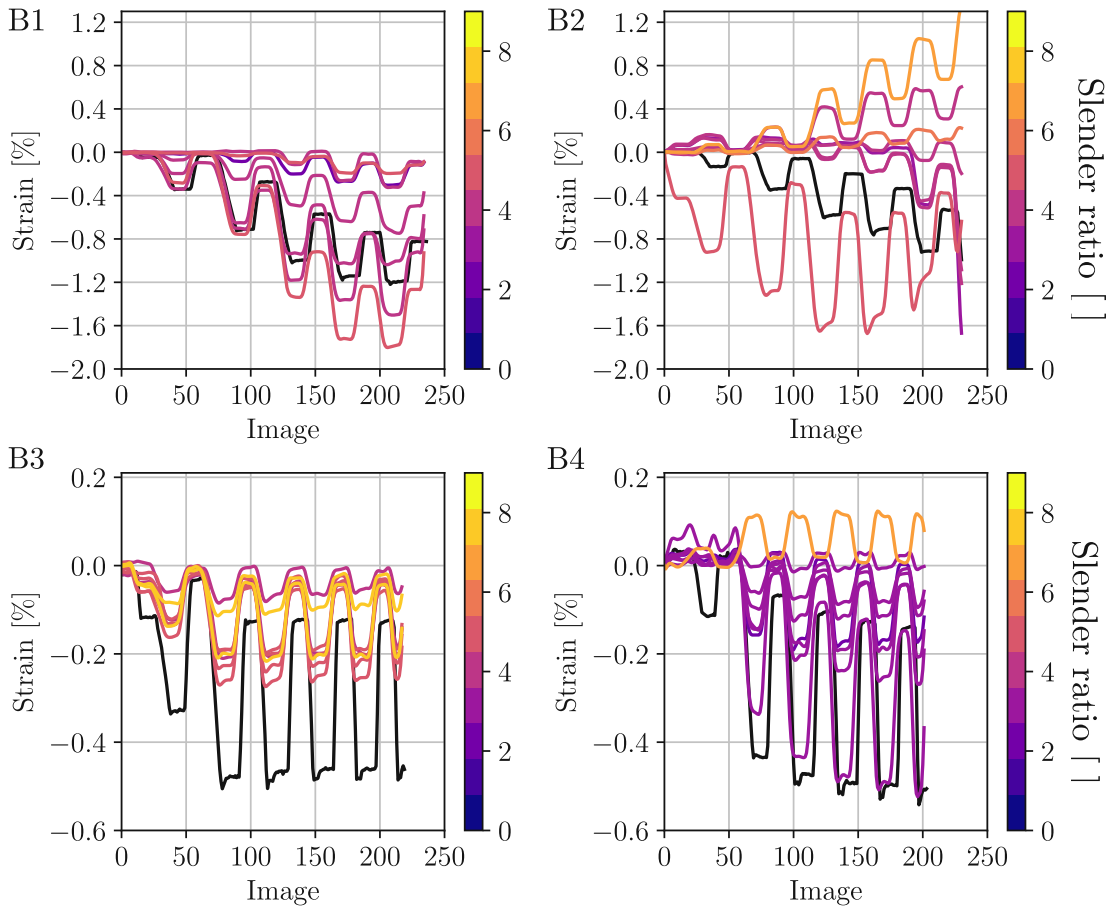

Figure 6.14: The longitudinal trabecular strains (in colours) and the average global sample strain (in black) for each specimen. Trabeculae are coloured, indicating their slenderness ratio.

6.5.5 Global strain versus longitudinal trabecular strain

The average global sample strain $\bar{\varepsilon}_G$ obtained from three virtual extensometers is plotted in Figure 6.15 (in black); the standard deviation of the three virtual extensometers are plotted in 6.16. The ramp and hold phases of all four specimens followed the loading profile, as depicted by the different colours indicating the trabeculae's inclination angle ϕ from the main loading axis. Compression strains were observed in many trabeculae following the loading profile and the average global strain. However, some trabeculae, especially in specimens B2 and B4, showed

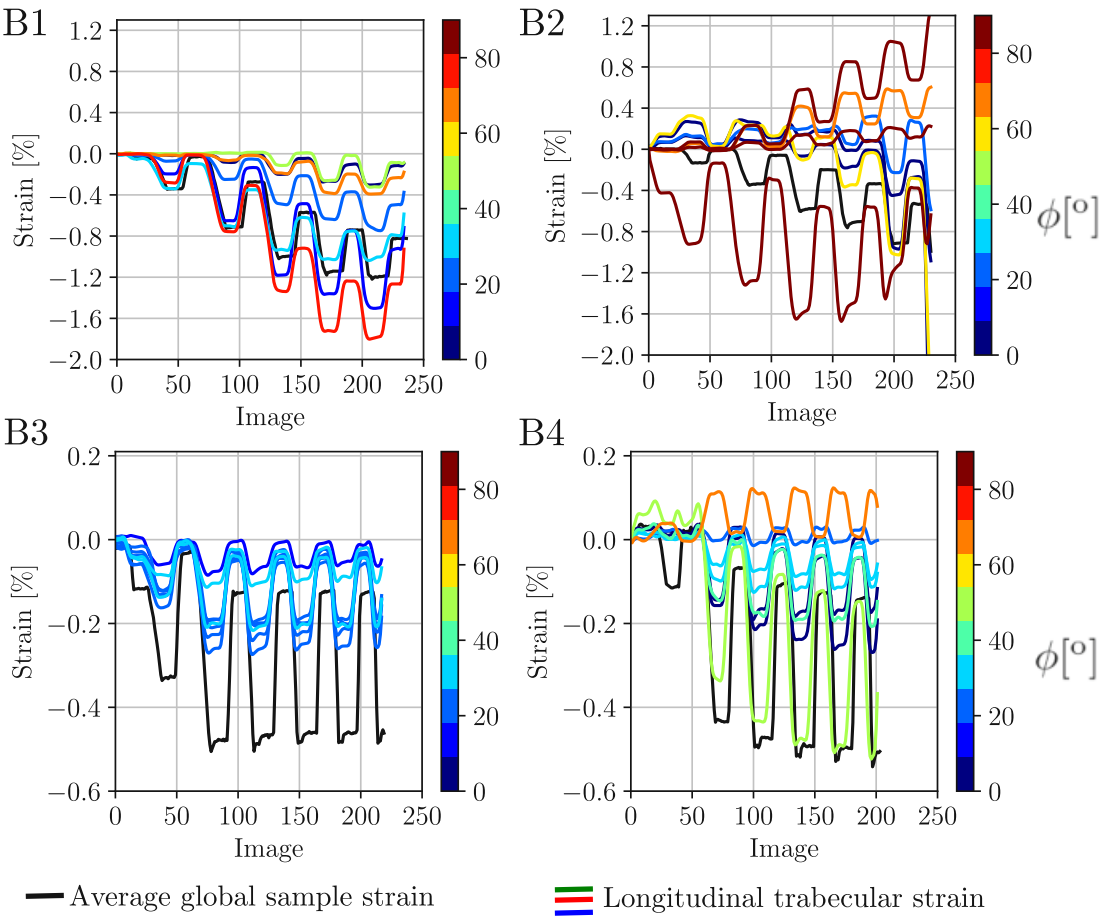

Figure 6.15: The longitudinal trabecular strain ε_{L1} (in colours) and the average global sample strain $\bar{\varepsilon}_G$ (in black) for each specimen. Trabeculae are coloured, indicating the inclination angle ϕ [°] of the trabeculae from the main loading axis.

tensile strains. Notably, the longitudinal trabecular strain was generally lower in magnitude than the average global sample strain, as seen in the difference between the black line and the other coloured lines. More information about the selected trabeculae and their locations within the trabecular network can be found in 6.5.3.

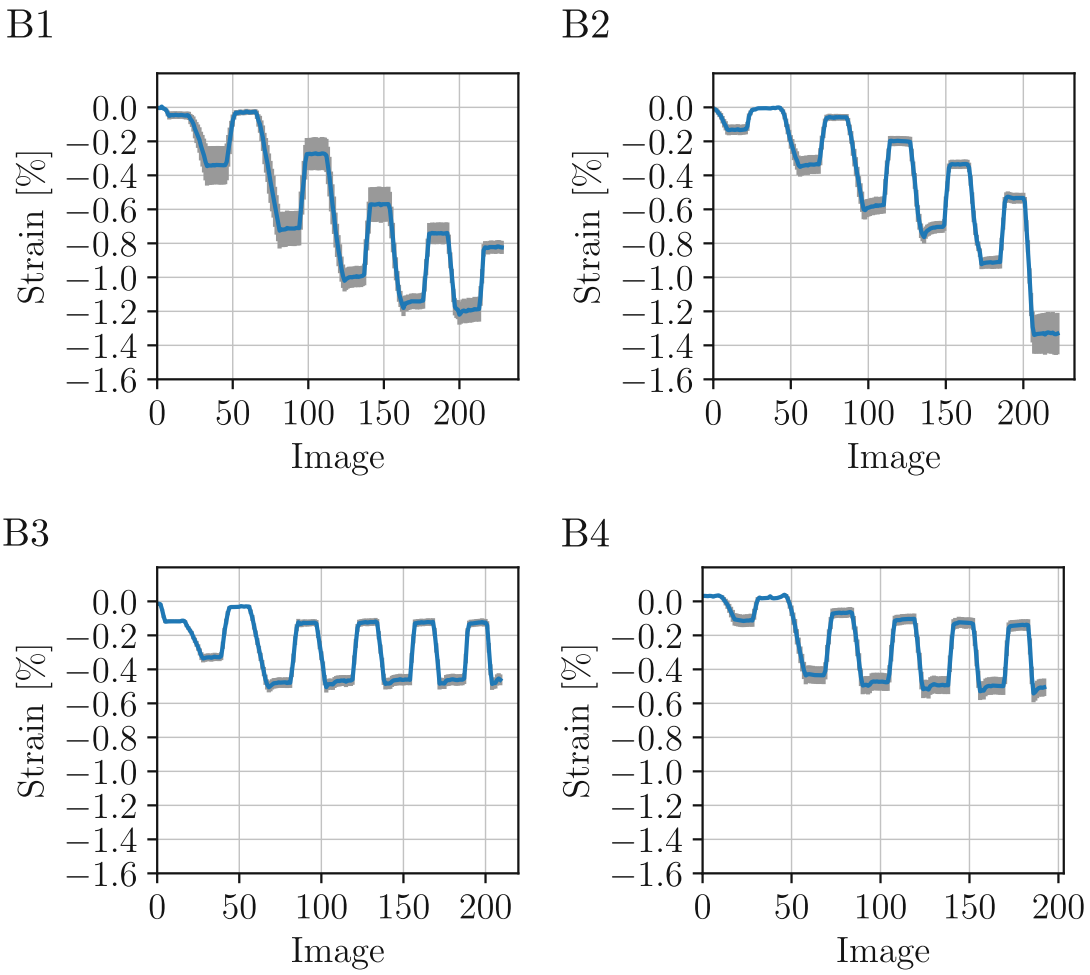

Figure 6.16: The average and standard deviation of the global sample strain from three virtual extensometers created on the surface of each sample.

The ratio between the longitudinal trabecular strain and the average global sample strain, for the fourth hold-phase around (image 160), is depicted in Figure 6.17 for all the investigated trabeculae (n=38). The red line indicates "equal" longitudinal trabecular and average global strains in tension and compression. Overall, the longitudinal trabecular strain was not higher than the average global sample strain, but the opposite, the ratio was between 0.008 and 0.81. In most cases, the average global sample strain was 2-folds the longitudinal trabecular strain. Interestingly, we see that the ratios are around 0.5. This means we apply an average global sample strain of "1" and see a longitudinal trabecular strain of "0.5". An exception

however can be seen at sample B1 and B2 where for three trabeculae the ratio is between 1.5 and 2, showing that the strain of the trabeculae can exceed the overall global strain applied to the sample. The difference can be related to the position of the trabeculae, where they were not highly loaded to show a magnification of the average global sample strain.

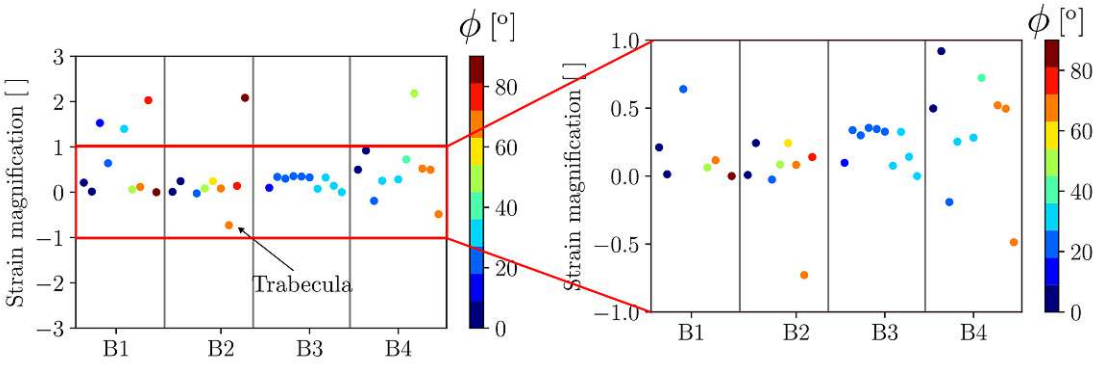

Figure 6.17: Strain ratio between the trabecular longitudinal strain and the global sample strain. These values are for the third hold-phase for each evaluated trabecula ($n = 38$) in each specimen.

6.6 Discussion

In this study, four specimens of trabecular bone were tested to analyze strains of individual trabeculae within their trabecular structure. The overall aim of this study was to gain a better understanding of the trabecular strain response within its network. Bending state of individual trabeculae within their trabecular structure was investigated by assessing the longitudinal strain of the trabeculae at both the middle and near the edge regions. High-resolution local surface strain of trabeculae were analyzed near the cutting surface of cubical samples. The influence of a trabecula's alignment and slenderness were presented as well as the magnification between the global sample strain and the longitudinal trabecular strain.

The applied force causes deformation in the trabecular network, resulting in compressive or tensile strains in individual trabeculae. While few studies [46] have shown full-field strain maps from experimental data that reveal both the

trabecular network and the strains in individual trabeculae, many other studies have focused solely on full-field strain analysis [80, 43, 52, 79] without detailed strain information on the surface of the trabeculae. The use of a telecentric lens allowed for highly accurate measurement of full-field strain maps, with a local (facet-point) strain error of only 0.04%±0.05% at zero-load and the ability to track the movement of a trabecula's endpoints. This level of accuracy was not achieved using a standard Sony camera, which had a facet-point strain error of approximately 0.3%. Investigation of longitudinal trabecular strain showed that the strain in a trabecula matched the average local surface strain ($\bar{\varepsilon}_{y'}$) for non-curved trabeculae. A minor difference was observed between the average transformed local strain and the longitudinal trabecular strain, which is expected since the overall change in the length of trabeculae is approximately equal to the average transformed local strain of the same trabecula.

Previous studies have focused either on single trabeculae, mostly rods, or on the trabecular structure/network as a whole. Experimental studies that tested single trabeculae extracted from their trabecular network reported ultimate strains of 5.1% [49], 20.2% [198], and 11.0% [76] under tensile load, and 8.2% [49] and 12.0% [199] under a three-point bending load of 60 N. However, these results provide no insights into strain magnification and cannot be compared to the strains experienced by trabecular bone within its trabecular network because trabeculae have different orientations and connections to other trabeculae, resulting in different strains when loaded within the network. The ratio between the longitudinal trabecular strain in the centre of the trabeculae and the global sample strain was less than one for most trabeculae at a global deformation of 0.6 mm, indicating no trabecular-level strain magnification. However, when the longitudinal trabecular strains near the edge of the trabeculae were considered, they showed pure compression, bending, or a mixed state of trabecular strain. In the case of a bending state, the strain magnification increased with increasing load and reached a maximum of 8-fold for the selected trabeculae, in line with the strain values reported in the literature by Morgan et al. [183] for maximum principal strains. Bayraktar et al. [196] and Odgaard et al. [195] reported a tissue yield strain between 0.6–1.0% at 0.8% global strain, corresponding to 1.25 magnification, and local

ultimate strains of 3.7% at 2.7% global strain, corresponding to 1.37 magnification, for human femoral neck trabecular bone and proximal tibiae trabecular bone, respectively. These results indicate that local yielding in trabecular bone occurs at a very small global strain which can be discovered experimentally by investigating the full-field surface strain of trabeculae within its trabecular network.

To the best of the authors' knowledge, no previous study has reported full-field surface strain measurements on the surface of trabeculae within their trabecular structure at a resolution of 2.4 µm. The results of this study indicate that the heterogeneity of deformation becomes more prominent with increasing load, as some trabeculae exhibit tension and/or compression strain. Inclined trabeculae were found to exhibit bending states, while trabeculae aligned along the loading direction showed compression strain at the centre of the trabecula where it is thinner, and finally, tensile strain was also present.

Finally the last objective of this study was to investigate the relation between the trabecula's orientation (and trabecula's slenderness) and the longitudinal trabecular strain. Even though it is counterintuitive not to find a relation between the orientation angle or the slenderness and the strain magnitude, this was the case for 38 trabeculae ranging between 0°and 90°inclination from the loading axis, with a slenderness ratio between 0 and 10. Nevertheless, it is important to study the trabecular bone network with regard to their architecture, since trabecular bone from the human vertebra is rod-like and from the femoral neck and head is plate-like [200, 201]. In our study, the longitudinal trabecular strain was less than 1% for trabeculae oriented between 35°and 55°. And it was less than 1% for trabeculae with a slenderness ratio greater than 6.5 and less than 2.5. This low maximum strain magnitude for slender trabeculae is associated with buckling rather than yielding, as confirmed by Kopperdahl and Keaveny [202] and Nagaraja et al. [51]. Slenderness helps in understanding buckling behaviour and fracture of trabecula within its trabecular network. As confirmed decades ago by Müller et al. [203] that a rod-like architecture failure was initiated by the buckling of the trabecula followed by the collapse of the overloaded structure.

This study provided high-resolution full-field strain maps and quantified the longitudinal trabecular strain of trabecular bone. However, there are some limitations

that need to be mentioned. First, only one DIC camera with a telecentric lens was used to track the deformation, which limited the analysis of the 3D deformation of the surface. Nevertheless, the local strain deformation was reliable due to the working principle of telecentric lenses, which are less sensitive to out-of-plane movement and the magnitude of the facet strain error was on average less than 0.09%. Moreover, the optimal facet size of 25 × 25 pixels was chosen based on the matching between the facet strain on a trabecula and the longitudinal trabecular strain. While a smaller facet size could be chosen, it would lead to higher noise, which would compromise the accuracy of the results. Additionally, the width of the trabeculae must be slightly higher than the reported values because cylindrical rods were projected onto the image plane. Despite these limitations, the presented results demonstrated that it was possible to evaluate the strain state (pure bending, tensile, compression, or a mixture) in single trabeculae with this setup, which was previously unobtainable for trabeculae within their trabecular structure.

6.7 Conclusion

This study demonstrated that high-resolution imaging can be used to obtain strain maps of trabeculae within the trabecular network, allowing for a relatively precise measurement of longitudinal trabecular strains and the local strains. These strains provide valuable insight into the ratio between globally applied strain and strain along the trabecular length within the network. Furthermore, utilizing a combination of the measurement method with another telecentric lens and camera would allow for deformation measurement of the trabecular surface from two sides. These strain maps can provide valuable information to expand our understanding of how individual trabeculae respond to load and support the overall structure of a trabecular network.

CHAPTER 7

Synthesis and outlook

7.1 Synthesis

The previous Chapters 4 to 6 contained the original research published in peer-reviewed journals during this dissertation. In the following, the main findings of the original contributions are summarized.

- The first study [133] provided a method for finding an optimal filtering parameter that can filter strain fields regardless of their strain nature being constant or with gradients, window size, and the applied load. Filtering can have a positive effect on reducing the noise, but the information lost needs to be evaluated; for instance, the simple mean and Gauss mean filters had a higher loss of information than that of Gauss LPF.
- A novel sample shape showing a strain field with two linear gradients is introduced [197]. It was possible to measure the linear gradient strain fields experimentally using DIC for engineering and biological materials at the macroscopic scale. The accuracy of DIC was high (less than 10 μstrain difference) with respect to the measurement of the strain gauges in the location of the constant strain field. In contrast in the linear gradient fields, due to the size of the strain gauges an evaluation of accuracy was not feasible.

However, it was shown that filtering was essential for the accurate detection of the normalized strain gradient, which was better for polymer and aluminium than for bone specimens.

- The third study [204] showed that it was possible to measure local strain using DIC at microscopic scale. The strain error at zero-load was less than 0.05% (500 μstrain) due to the high-resolution 2.4 μm/pixel of the used telecentric lens which counted for out-of-plane movements.

- With optimal DIC parameters and test setup, strain measurement on the surface of trabeculae was achievable. It was demonstrated that at least four and nine measurement points were obtainable across the width of the trabeculae, for width of at least 120 μm and 240 μm, respectively. From these measurement points, detailed high-resolution strain maps were generated [204].

- At the microscopic scale, linear gradients (pure bending states) were detected at the outermost edge of the trabeculae. Resulting in a distinctive increase in strain magnification reaching up to eight times the strain detected at the center of the trabeculae [204].

7.2 Future outlook

This thesis work aimed to evaluate the capability of DIC measurement systems to assess linear gradient strain fields at both macroscopic and microscopic scales. The findings of these studies offer promising prospects for future research in DIC as a measurement system and its application in the field of biomechanics.

For DIC as a measurement system, this thesis introduced methodological approaches that can be adopted for scrutinizing and validating the strain fields obtained from DIC systems. The filtering strategies and the novel specimen shape can be used as a reference to determine the accuracy of DIC systems and to improve it accordingly.

For the field of biomechanics, studying the mechanical response of single trabeculae within the trabecular structure to loading will open up new possibilities for studying trabecular bone mechanics and will help in understanding the factors contributing to the mechanical properties of trabeculae. It would be interesting to apply the findings of this dissertation in utilizing DIC to obtain strain fields on a variety of trabecular bone and loading conditions. These findings would lead to a deeper comprehension of how individual trabeculae contribute to the stability of the trabecular bone structure.

Bibliography

[1] Michael A Sutton, Jean Jose Orteu, and Hubert Schreier. *Image correlation for shape, motion and deformation measurements: basic concepts, theory and applications*. Springer Science & Business Media, 2009.

[2] Stéphane Avril, Fabrice Pierron, Michael A Sutton, and Junhui Yan. Identification of elasto-visco-plastic parameters and characterization of lüders behavior using digital image correlation and the virtual fields method. *Mechanics of materials*, 40(9):729–742, 2008.

[3] Xu Liu and Rongsheng Lu. Testing system for the mechanical properties of small-scale specimens based on 3d microscopic digital image correlation. *Sensors*, 20(12):3530, 2020.

[4] Pierre Darry Versaillot, Yu-Fei Wu, and Zi-Long Zhao. Experimental study on the evolution of necking zones of metallic materials. *International Journal of Mechanical Sciences*, 189:106002, 2021.

[5] Zhutian Xu, Linfa Peng, Mukesh K Jain, David Anderson, and John Carsley. Local and global tensile deformation behavior of aa7075 sheet material at 673ok and different strain rates. *International Journal of Mechanical Sciences*, 195:106241, 2021.

[6] Lorenzo Grassi, Sami P Väänänen, Saber Amin Yavari, Jukka S Jurvelin, Harrie Weinans, Matti Ristinmaa, Amir A Zadpoor, and Hanna Isaksson. Full-field strain measurement during mechanical testing of the human femur at physiologically relevant strain rates. *Journal of biomechanical engineering*, 136(11):111010, 2014.

[7] Fabienne Lagattu, Jean Brillaud, and Marie-Christine Lafarie-Frenot. High strain gradient measurements by using digital image correlation technique. *Materials Characterization*, 53(1):17–28, 2004.

[8] Shun-Fa Hwang and Wei-Jie Wu. Deformation measurement around a high strain-gradient region using a digital image correlation method. *Journal of Mechanical Science and Technology*, 26(10):3169–3175, 2012.

[9] Mahdi Ashrafi and Mark E. Tuttle. Measurement of strain gradients using digital image correlation by applying printed-speckle patterns. *Experimental Techniques*, 40(2):891–897, 2016.

[10] D Lecompte, S Bossuyt, S Cooreman, H Sol, and J Vantomme. Study and generation of optimal speckle patterns for DIC. In *Proceedings of the annual conference and exposition on experimental and applied mechanics*, volume 3, pages 1643–1649, 2007.

[11] Giacomo Lionello and Luca Cristofolini. A practical approach to optimizing the preparation of speckle patterns for digital-image correlation. *Meas. Sci. Technol.*, 25(10):107001, 2014.

[12] Marco Palanca, Gianluca Tozzi, and Luca Cristofolini. The use of digital image correlation in the biomechanical area: a review. *International biomechanics*, 3(1):1–21, 2016.

[13] Jacopo Baldoni, Giacomo Lionello, Fabiana Zama, and Luca Cristofolini. Comparison of different filtering strategies to reduce noise in strain measurement with digital image correlation. *The Journal of Strain Analysis for Engineering Design*, 51(6):416–430, August 2016.

[14] Sarah Hensley, Mackenzie Christensen, Scott Small, Derek Archer, Emily Lakes, and Renee Rogge. Digital image correlation techniques for strain measurement in a variety of biomechanical test models. *Acta of bioengineering and biomechanics*, 19:187–195, 2017.

[15] Alice Acciaioli, Giacomo Lionello, and Massimiliano Baleani. Experimentally achievable accuracy using a digital image correlation technique in measuring

small-magnitude (less than 0.1%) homogeneous strain fields. *Materials*, 11(5):751, 2018.

[16] MGD Geers, R De Borst, and WAM Brekelmans. Computing strain fields from discrete displacement fields in 2d-solids. *International Journal of Solids and Structures*, 33(29):4293–4307, 1996.

[17] Stéphane Avril, Pierre Feissel, Fabrice Pierron, and Pierre Villon. Comparison of two approaches for differentiating full-field data in solid mechanics. *Measurement Science and Technology*, 21(1):015703, 2009.

[18] VP Rajan, MN Rossol, and FW Zok. Optimization of digital image correlation for high-resolution strain mapping of ceramic composites. *Experimental mechanics*, 52(9):1407–1421, 2012.

[19] V Rubino, N Lapusta, AJ Rosakis, S Leprince, and JP Avouac. Static laboratory earthquake measurements with the digital image correlation method. *Experimental Mechanics*, 55(1):77–94, 2015.

[20] Lorenzo Grassi, Sami P Väänänen, Saber Amin Yavari, Harrie Weinans, Jukka S Jurvelin, Amir A Zadpoor, and Hanna Isaksson. Experimental validation of finite element model for proximal composite femur using optical measurements. *Journal of the mechanical behavior of biomedical materials*, 21:86–94, 2013.

[21] Mark Begonia, Mark Dallas, Mark L Johnson, and Ganesh Thiagarajan. Comparison of strain measurement in the mouse forearm using subject-specific finite element models, strain gaging, and digital image correlation. *Biomechanics and modeling in mechanobiology*, 16(4):1243–1253, 2017.

[22] Hao Wu, Guoyan Zhao, and Weizhang Liang. Investigation of cracking behavior and mechanism of sandstone specimens with a hole under compression. *International Journal of Mechanical Sciences*, 163:105084, 2019.

[23] Hannah Gustafson, Gunter Siegmund, and Peter Cripton. Comparison of strain rosettes and digital image correlation for measuring vertebral body strain. *J. Biomech. Eng.*, 138(5):054501, 2016.

[24] Yekutiel Katz and Zohar Yosibash. New insights on the proximal femur biomechanics using digital image correlation. *Journal of biomechanics*, 101:109599, 2020.

[25] M Liu, J Guo, C-Y Hui, and AT Zehnder. Application of digital image correlation (dic) to the measurement of strain concentration of a pva dual-crosslink hydrogel under large deformation. *Experimental Mechanics*, 59(7):1021–1032, 2019.

[26] Enrico Schileo, Jonathan Pitocchi, Cristina Falcinelli, and Fulvia Taddei. Cortical bone mapping improves finite element strain prediction accuracy at the proximal femur. *Bone*, 136:115348, 2020.

[27] Anna Gustafsson, Martina Tognini, Frida Bengtsson, T Christian Gasser, Hanna Isaksson, and Lorenzo Grassi. Subject-specific fe models of the human femur predict fracture path and bone strength under single-leg-stance loading. *Journal of the Mechanical Behavior of Biomedical Materials*, 113:104118, 2021.

[28] Lorenzo Grassi, Joeri Kok, Anna Gustafsson, Yi Zheng, Sami P Väänänen, Jukka S Jurvelin, and Hanna Isaksson. Elucidating failure mechanisms in human femurs during a fall to the side using bilateral digital image correlation. *Journal of biomechanics*, 106:109826, 2020.

[29] Marco Palanca, Egon Perilli, and Saulo Martelli. Body anthropometry and bone strength conjointly determine the risk of hip fracture in a sideways fall. *Annals of biomedical engineering*, pages 1–11, 2020.

[30] Bing Pan. Bias error reduction of digital image correlation using gaussian pre-filtering. *Optics and Lasers in Engineering*, 51(10):1161–1167, 2013.

[31] Yihao Zhou, Chen Sun, Yuntao Song, and Jubing Chen. Image pre-filtering for measurement error reduction in digital image correlation. *Optics and Lasers in Engineering*, 65:46–56, 2015.

[32] José Xavier, António MR Sousa, José JL Morais, Vitor MJ Filipe, and Mario A Vaz. Measuring displacement fields by cross-correlation and a differential technique: experimental validation. *Optical Engineering*, 51(4):043602, 2012.

[33] V Rubino, AJ Rosakis, and N Lapusta. Full-field ultrahigh-speed quantification of dynamic shear ruptures using digital image correlation. *Experimental Mechanics*, 59(5):551–582, 2019.

[34] F Mortazavi, M Levesque, and I Villemure. Image-based continuous displacement measurements using an improved spectral approach. *Strain*, 49(3):233–248, 2013.

[35] TH Becker and TJ Marrow. A robust finite element-based filter for digital image and volume correlation displacement data. *Experimental Mechanics*, 61(6):901–916, 2021.

[36] Jiangping Xu, Ali Moussawi, Renaud Gras, and Gilles Lubineau. Using image gradients to improve robustness of digital image correlation to non-uniform illumination: effects of weighting and normalization choices. *Experimental Mechanics*, 55(5):963–979, 2015.

[37] Paolo Mazzoleni, Fabio Matta, Emanuele Zappa, Michael A Sutton, and Alfredo Cigada. Gaussian pre-filtering for uncertainty minimization in digital image correlation using numerically-designed speckle patterns. *Optics and Lasers in Engineering*, 66:19–33, 2015.

[38] G Boivin and PJ Meunier. The mineralization of bone tissue: a forgotten dimension in osteoporosis research. *Osteoporosis International*, 14(3):19–24, 2003.

[39] Georg Osterhoff, Elise F Morgan, Sandra J Shefelbine, Lamya Karim, Laoise M McNamara, and Peter Augat. Bone mechanical properties and changes with osteoporosis. *Injury*, 47:S11–S20, 2016.

[40] Martin Stauber and Ralph Müller. Age-related changes in trabecular bone microstructures: global and local morphometry. *Osteoporosis International*, 17(4):616–626, 2006.

[41] X Sherry Liu, Paul Sajda, Punam K Saha, Felix W Wehrli, Grant Bevill, Tony M Keaveny, and X Edward Guo. Complete volumetric decomposition of individual trabecular plates and rods and its morphological correlations with anisotropic elastic moduli in human trabecular bone. *Journal of Bone and Mineral Research*, 23(2):223–235, 2008.

[42] Tony M Keaveny, Robert E Borchers, Lorna J Gibson, and Wilson C Hayes. Theoretical analysis of the experimental artifact in trabecular bone compressive modulus. *Journal of Biomechanics*, 26(4-5):599–607, 1993.

[43] Alice Acciaioli, Luigi Falco, and Massimiliano Baleani. Measurement of apparent mechanical properties of trabecular bone tissue: Accuracy and limitation of digital image correlation technique. *Journal of the mechanical behavior of biomedical materials*, 103:103542, 2020.

[44] Giulia Cavazzoni, Luca Cristofolini, Enrico Dall'Ara, and Marco Palanca. Bone metastases do not affect the measurement uncertainties of a global digital volume correlation algorithm. *Frontiers in Bioengineering and Biotechnology*, 11:1152358, 2023.

[45] F Gillard, Richard Boardman, Mark Mavrogordato, Dave Hollis, Ian Sinclair, Fabrice Pierron, and Martin Browne. The application of digital volume correlation (dvc) to study the microstructural behaviour of trabecular bone during compression. *Journal of the mechanical behavior of biomedical materials*, 29:480–499, 2014.

[46] Mikael J Turunen, Sophie Le Cann, Erika Tudisco, Goran Lovric, Alessandra Patera, Stephen A Hall, and Hanna Isaksson. Sub-trabecular strain evolution in human trabecular bone. *Scientific reports*, 10(1):1–14, 2020.

[47] Marco Palanca, Andrew J Bodey, Mario Giorgi, Marco Viceconti, Damien Lacroix, Luca Cristofolini, and Enrico Dall'Ara. Local displacement and strain uncertainties in different bone types by digital volume correlation of synchrotron microtomograms. *Journal of biomechanics*, 58:27–36, 2017.

[48] GL Niebur, JC Yuen, AC Hsia, and TM Keaveny. Convergence behavior of high-resolution finite element models of trabecular bone. *J Biomech Eng*, 1999.

[49] Roberto Carretta, Edgar Stüssi, Ralph Müller, and Silvio Lorenzetti. Within subject heterogeneity in tissue-level post-yield mechanical and material properties in human trabecular bone. *Journal of the mechanical behavior of biomedical materials*, 24:64–73, 2013.

[50] Noel M Harrison, Pat F McDonnell, Denis C O'Mahoney, Oran D Kennedy, Fergal J O'Brien, and Peter E McHugh. Heterogeneous linear elastic trabecular bone modelling using micro-ct attenuation data and experimentally measured heterogeneous tissue properties. *Journal of biomechanics*, 41(11):2589–2596, 2008.

[51] Srinidhi Nagaraja, Tracey L Couse, and Robert E Guldberg. Trabecular bone microdamage and microstructural stresses under uniaxial compression. *Journal of biomechanics*, 38(4):707–716, 2005.

[52] Ricardo Belda, Marta Palomar, José Luis Peris-Serra, Ana Vercher-Martínez, and Eugenio Giner. Compression failure characterization of cancellous bone combining experimental testing, digital image correlation and finite element modeling. *International Journal of Mechanical Sciences*, 165:105213, 2020.

[53] Narges Kaynia, Elaine Soohoo, Tony M Keaveny, and Galateia J Kazakia. Effect of intraspecimen spatial variation in tissue mineral density on the apparent stiffness of trabecular bone. *Journal of biomechanical engineering*, 137(1), 2015.

[54] FM Sánchez-Arévalo and G Pulos. Use of digital image correlation to determine the mechanical behavior of materials. *Materials characterization*, 59(11):1572–1579, 2008.

[55] Neil A Hoult, W Andy Take, Chris Lee, and Michael Dutton. Experimental accuracy of two dimensional strain measurements using digital image correlation. *Engineering Structures*, 46:718–726, 2013.

[56] Gwendolin Prusa, Leandra Bauer, Inês Santos, Christoph Thorwächter, Matthias Woiczinski, and Manuel Kistler. Strain evaluation of axially loaded collateral ligaments: a comparison of digital image correlation and strain gauges. *BioMedical Engineering OnLine*, 22(1):13, 2023.

[57] Jean-Noël Périé, Sylvain Calloch, Christophe Cluzel, and François Hild. Analysis of a multiaxial test on a c/c composite by using digital image correlation and a damage model. *Experimental Mechanics*, 42(3):318–328, 2002.

[58] Pavel Sztefek, Maximilien Vanleene, Robin Olsson, Rebecca Collinson, Andrew A. Pitsillides, and Sandra Shefelbine. Using digital image correlation to determine bone surface strains during loading and after adaptation of the mouse tibia. *J. Biomech.*, 43(4):599–605, March 2010.

[59] Luc Chevalier, Sylvain Calloch, François Hild, and Yann Marco. Digital image correlation used to analyze the multiaxial behavior of rubber-like materials. *European Journal of Mechanics-A/Solids*, 20(2):169–187, 2001.

[60] Ha Koerber, Jb Xavier, and PP Camanho. High strain rate characterisation of unidirectional carbon-epoxy im7-8552 in transverse compression and in-plane shear using digital image correlation. *Mechanics of Materials*, 42(11):1004–1019, 2010.

[61] M Eskandari, MR Yadegari-Dehnavi, A Zarei-Hanzaki, MA Mohtadi-Bonab, R Basu, and JA Szpunar. In-situ strain localization analysis in low density transformation-twinning induced plasticity steel using digital image correlation. *Optics and Lasers in Engineering*, 67:1–16, 2015.

[62] Luis Pablo Canal, Carlos González, Jon M Molina-Aldareguía, Javier Segurado, and Javier LLorca. Application of digital image correlation at the microscale in fiber-reinforced composites. *Composites Part A: Applied Science and Manufacturing*, 43(10):1630–1638, 2012.

[63] F Grytten, H Daiyan, M Polanco-Loria, and S Dumoulin. Use of digital image correlation to measure large-strain tensile properties of ductile thermoplastics. *Polymer Testing*, 28(6):653–660, 2009.

[64] Bertrand Wattrisse, A Chrysochoos, J-M Muracciole, and M Némoz-Gaillard. Analysis of strain localization during tensile tests by digital image correlation. *Experimental mechanics*, 41(1):29–39, 2001.

[65] H Lu, G Vendroux, and WG Knauss. Surface deformation measurements of a cylindrical specimen by digital image correlation. *Experimental Mechanics*, 37(4):433–439, 1997.

[66] F Lagattu, MC Lafarie-Frenot, TQ Lam, and J Brillaud. Experimental characterisation of overstress accommodation in notched cfrp composite laminates. *Composite Structures*, 67(3):347–357, 2005.

[67] Jun Zhang, Yaxiong Cai, Wenjing Ye, and TX Yu. On the use of the digital image correlation method for heterogeneous deformation measurement of porous solids. *Optics and lasers in engineering*, 49(2):200–209, 2011.

[68] EV Iarve and NJ Pagano. Singular full-field stresses in composite laminates with open holes. *International Journal of Solids and Structures*, 38(1):1–28, 2001.

[69] Bing Pan, Zhaoyang Wang, and Zixing Lu. Genuine full-field deformation measurement of an object with complex shape using reliability-guided digital image correlation. *Optics express*, 18(2):1011–1023, 2010.

[70] Yueqi Wang, Pascal Lava, Sam Coppieters, Maarten De Strycker, Paul Van Houtte, and Dimitri Debruyne. Investigation of the uncertainty of DIC under heterogeneous strain states with numerical tests. *Strain*, 48(6):453–462, 2012.

[71] Michael Jerabek, Zoltan Major, and Reinhold W Lang. Strain determination of polymeric materials using digital image correlation. *Polymer Testing*, 29(3):407–416, 2010.

[72] Dong Sheng Zhang and Dwayne D Arola. Applications of digital image correlation to biological tissues. *Journal of Biomedical Optics*, 9(4):691–699, 2004.

[73] Melissa K Ryan, Sara Oliviero, Maria Cristiana Costa, J Mark Wilkinson, and Enrico Dall'Ara. Heterogeneous strain distribution in the subchondral bone of human osteoarthritic femoral heads, measured with digital volume correlation. *Materials*, 13(20):4619, 2020.

[74] JD Currey. Bones: Structure and mechanicsprinceton university press. *Princeton, NJ*, 2002.

[75] R Scott Braithwaite, Nananda F Col, and John B Wong. Estimating hip fracture morbidity, mortality and costs. *Journal of the American Geriatrics Society*, 51(3):364–370, 2003.

[76] Martin Frank, Dorothee Marx, Vedran Nedelkovski, Dieter H Pahr, Philipp J Thurner, et al. Dehydration of individual bovine trabeculae causes transition from ductile to quasi-brittle failure mode. *Journal of the mechanical behavior of biomedical materials*, 87:296–305, 2018.

[77] Roberto Carretta, Benoit Luisier, Daniel Bernoulli, Edgar Stüssi, Ralph Müller, and Silvio Lorenzetti. Novel method to analyze post-yield mechanical properties at trabecular bone tissue level. *Journal of the mechanical behavior of biomedical materials*, 20:6–18, 2013.

[78] P Bokam, A Germaneau, C Breque, P Rigoard, T Vendeuvre, and V Valle. Fracture behavior of cancellous bone and cancellous bone-pmma bone cement interface: An experimental study using an integrated methodology (wedge splitting test and heaviside-based digital image correlation). *Journal of the Mechanical Behavior of Biomedical Materials*, 122:104663, 2021.

[79] P Bokam, A Germaneau, P Rigoard, T Vendeuvre, and Valery Valle. Evaluation of fracture properties of cancellous bone tissues using digital image correlation/wedge splitting test method. *Journal of the mechanical behavior of biomedical materials*, 102:103469, 2020.

[80] Athanasios Tsirigotis and Despoina D Deligianni. Combining digital image correlation and acoustic emission for monitoring of the strain distribution until yielding during compression of bovine cancellous bone. *Frontiers in Materials*, 4:44, 2017.

[81] Hannah M Gustafson, Peter A Cripton, Stephen J Ferguson, and Benedikt Helgason. Comparison of specimen-specific vertebral body finite element models with experimental digital image correlation measurements. *Journal of the mechanical behavior of biomedical materials*, 65:801–807, 2017.

[82] D Spera, K Genovese, and A Voloshin. Application of stereo-digital image correlation to full-field 3-d deformation measurement of intervertebral disc. *Strain*, 47:e572–e587, 2011.

[83] Timothy Patrick Holsgrove, Dario Cazzola, Ezio Preatoni, Grant Trewartha, Anthony W Miles, Harinderjit Singh Gill, and Sabina Gheduzzi. An investigation into axial impacts of the cervical spine using digital image correlation. *The Spine Journal*, 15(8):1856–1863, 2015.

[84] Maria Luisa Ruspi, Marco Palanca, Cesare Faldini, and Luca Cristofolini. Full-field in vitro investigation of hard and soft tissue strain in the spine by means of digital image correlation. *Muscles, ligaments and tendons journal*, 7(4):538, 2017.

[85] Marco Palanca, Miguel Marco, Maria Luisa Ruspi, and Luca Cristofolini. Full-field strain distribution in multi-vertebra spine segments: An in vitro application of digital image correlation. *Medical engineering & physics*, 52:76–83, 2018.

[86] Anna Gustafsson, Neashan Mathavan, Mikael J Turunen, Jonas Engqvist, Hanifeh Khayyeri, Stephen A Hall, and Hanna Isaksson. Linking multiscale deformation to microstructure in cortical bone using in situ loading, digital image correlation and synchrotron x-ray scattering. *Acta biomaterialia*, 69:323–331, 2018.

[87] Seth Gilchrist, Pierre Guy, and Peter A Cripton. Development of an inertia-driven model of sideways fall for detailed study of femur fracture mechanics. *Journal of biomechanical engineering*, 135(12), 2013.

[88] Yekutiel Katz, Zohar Yosibash, Moshe Salai, and Nimrod Snir. Strain shielding for cemented hip implants. *Clinical Biomechanics*, 77:105027, 2020.

[89] L Cristofolini, M Juszczyk, F Taddei, and M Viceconti. Strain distribution in the proximal human femoral metaphysis. *Proceedings of the Institution of Mechanical Engineers, Part H: Journal of Engineering in Medicine*, 223(3):273–288, 2009.

[90] Lorenzo Grassi, Sami P Väänänen, Matti Ristinmaa, Jukka S Jurvelin, and Hanna Isaksson. How accurately can subject-specific finite element models predict strains and strength of human femora? investigation using full-field measurements. *Journal of Biomechanics*, 49(5):802–806, 2016.

[91] AS Dickinson, AC Taylor, H Ozturk, and M Browne. Experimental validation of a finite element model of the proximal femur using digital image correlation and a composite bone model. *Journal of biomechanical engineering*, 133(1):014504, January 2011.

[92] Sami P Väänänen, Saber Amin Yavari, Harrie Weinans, Amir Abbas Zadpoor, Jukka S Jurvelin, and Hanna Isaksson. Repeatability of digital image correlation for measurement of surface strains in composite long bones. *Journal of biomechanics*, 46(11):1928–1932, 2013.

[93] Souptick Chanda, Alexander Dickinson, Sanjay Gupta, and Martin Browne. Full-field in vitro measurements and in silico predictions of strain shielding in the implanted femur after total hip arthroplasty. *Proceedings of the Institution of Mechanical Engineers, Part H: Journal of Engineering in Medicine*, 229(8):549–559, 2015.

[94] E Tayton, S Evans, and D O'doherty. Mapping the strain distribution on the proximal femur with titanium and flexible-stemmed implants using digital image correlation. *The Journal of bone and joint surgery. British volume*, 92(8):1176–1181, 2010.

[95] Irini Tatani, Panagiotis Megas, Andreas Panagopoulos, Ioannis Diamantakos, Ph Nanopoulos, and Sp Pantelakis. Comparative analysis of the biomechanical behavior of two different design metaphyseal-fitting short stems using digital image correlation. *Biomedical engineering online*, 19(1):1–18, 2020.

[96] Luca Cristofolini and Marco Viceconti. Comparison of uniaxial and triaxial rosette gages for strain measurement in the femur. *Experimental mechanics*, 37(3):350–354, 1997.

[97] JH Keyak, MG Fourkas, JM Meagher, and HB Skinner. Validation of an automated method of three-dimensional finite element modelling of bone. *Journal of biomedical engineering*, 15(6):505–509, 1993.

[98] Y-H Kim, J-S Kim, and S-H Cho. Strain distribution in the proximal human femur: an in vitro comparison in the intact femur and after insertion of reference and experimental femoral stems. *The Journal of Bone and Joint Surgery. British volume*, 83(2):295–301, 2001.

[99] Lorenzo Zani, Paolo Erani, Lorenzo Grassi, Fulvia Taddei, and Luca Cristofolini. Strain distribution in the proximal human femur during in vitro simulated sideways fall. *Journal of Biomechanics*, 48(10):2130–2143, 2015.

[100] Verne L Roberts. Strain-gage techniques in biomechanics. *Experimental Mechanics*, 6(3):19A–22A, 1966.

[101] PO Østbyhaug, J Klaksvik, P Romundstad, and A Aamodt. An in vitro study of the strain distribution in human femora with anatomical and customised femoral stems. *The Journal of Bone and Joint Surgery. British volume*, 91(5):676–682, 2009.

[102] Mark T Begonia, Mark Dallas, Bruno Vizcarra, Ying Liu, Mark L Johnson, and Ganesh Thiagarajan. Non-contact strain measurement in the mouse forearm loading model using digital image correlation (dic). *Bone*, 81:593–601, 2015.

[103] C Rolf, P Westblad, I Ekenman, A Lundberg, N Murphy, M Lamontagne, and K Halvorsen. An experimental in vivo method for analysis of local deformation on tibia, with simultaneous measures of ground reaction forces, lower extremity muscle activity and joint motion. *Scandinavian journal of medicine & science in sports*, 7(3):144–151, 1997.

[104] Susan J Hoshaw, David P Fyhrie, Y Takano, DB Burr, and C Milgrom. A method suitable for in vivo measurement of bone strain in humans. *Journal of biomechanics*, 30(5):521–524, 1997.

[105] LE Lanyon, WGJ Hampson, AE Goodship, and JS Shah. Bone deformation recorded in vivo from strain gauges attached to the human tibial shaft. *Acta Orthopaedica Scandinavica*, 46(2):256–268, 1975.

[106] LE Lanyon and RN Smith. Bone strain in the tibia during normal quadrupedal locomotion. *Acta Orthopaedica Scandinavica*, 41(3):238–248, 1970.

[107] Luca Cristofolini, Marco Viceconti, Angelo Cappello, and Aldo Toni. Mechanical validation of whole bone composite femur models. *Journal of biomechanics*, 29(4):525–535, 1996.

[108] A Completo, F Fonseca, and JA Simoes. Finite element and experimental cortex strains of the intact and implanted tibia. *Journal of Biomechanical Engineering*, 2007.

[109] Ievgen Levadnyi, Jan Awrejcewicz, Yan Zhang, and Yaodong Gu. Comparison of femur strain under different loading scenarios: Experimental testing. *Proceedings of the Institution of Mechanical Engineers, Part H: Journal of Engineering in Medicine*, 235(1):17–27, 2021.

[110] Fulvia Taddei, Enrico Schileo, Benedikt Helgason, Luca Cristofolini, and Marco Viceconti. The material mapping strategy influences the accuracy of ct-based finite element models of bones: an evaluation against experimental measurements. *Medical engineering & physics*, 29(9):973–979, 2007.

[111] Anita Fung, Lindsay L Loundagin, and W Brent Edwards. Experimental validation of finite element predicted bone strain in the human metatarsal. *Journal of Biomechanics*, 60:22–29, 2017.

[112] CC Perry. Strain-gage reinforcement effects on orthotropic materials. *Exp. Tech.*, 10(2):20–24, 1986.

[113] Steven Boyd, Nigel Shrive, Greg Wohl, Ralph Müller, and Ron Zernicke. Measurement of cancellous bone strain during mechanical tests using a new extensometer device. *Medical engineering & physics*, 23(6):411–416, 2001.

[114] Anders Odgaard and Frank Linde. The underestimation of young's modulus in compressive testing of cancellous bone specimens. *Journal of biomechanics*, 24(8):691–698, 1991.

[115] Gail P Perusek, Brian L Davis, Amy C Courtney, and Susan E D'Andrea. An extensometer for global measurement of bone strain suitable for use in vivo in humans. *Journal of biomechanics*, 34(3):385–391, 2001.

[116] Thomas Luyckx, Matthias Verstraete, Karel De Roo, Wim De Waele, Johan Bellemans, and Jan Victor. Digital image correlation as a tool for three-dimensional strain analysis in human tendon tissue. *Journal of experimental orthopaedics*, 1(1):7, 2014.

[117] Michael A Sutton, J H Yan, V Tiwari, HW Schreier, and Jean-José Orteu. The effect of out-of-plane motion on 2d and 3d digital image correlation measurements. *Optics and Lasers in Engineering*, 46(10):746–757, 2008.

[118] Thomas Luhmann, Stuart Robson, Stephen Kyle, and Ian Harley. *Close range photogrammetry: principles, techniques and applications*, volume 3. Whittles publishing Dunbeath, 2006.

[119] GOM-GmbH. *Acquisition Basic: GOM Software 2016*. Germany, 2015.

[120] Bing Pan, Kemao Qian, Huimin Xie, and Anand Asundi. Two-dimensional digital image correlation for in-plane displacement and strain measurement: a review. *Measurement science and technology*, 20(6):062001, 2009.

[121] Sun Yaofeng and John HL Pang. Study of optimal subset size in digital image correlation of speckle pattern images. *Opt Lasers Eng*, 45(9):967–974, 2007.

[122] Y Barranger, P Doumalin, JC Dupré, and A Germaneau. Digital image correlation accuracy: influence of kind of speckle and recording setup. In *EPJ web of conferences*, volume 6, page 31002. EDP Sciences, 2010.

[123] Giacomo Lionello, Camille Sirieix, and Massimiliano Baleani. An effective procedure to create a speckle pattern on biological soft tissue for digital image correlation measurements. *J Mech Behav Biomed Mater*, 39:1–8, 2014.

[124] Farhad Mortazavi. *Development of a global digital image correlation approach for fast high-resolution displacement measurements*. PhD thesis, École Polytechnique de Montréal, 2013.

[125] Jakson M Vassoler and Eduardo A Fancello. Error analysis of the digital image correlation method. *Mecánica Computacional*, 29(61):6149–6161, 2010.

[126] François Hild and Stéphane Roux. Comparison of local and global approaches to digital image correlation. *Experimental Mechanics*, 52(9):1503–1519, 2012.

[127] Bo Wang and Bing Pan. Subset-based local vs. finite element-based global digital image correlation: A comparison study. *Theoretical and Applied Mechanics Letters*, 6(5):200–208, 2016.

[128] GOM-GmbH. *Digital Image Correlation and Strain Computation Basics*. Germany, 2016.

[129] D. Lecompte, A. Smits, Sven Bossuyt, H. Sol, J. Vantomme, D. Van Hemelrijck, and A. M. Habraken. Quality assessment of speckle patterns for digital image correlation. *Opt. Lasers Eng.*, 44(11):1132–1145, November 2006.

[130] Marco Palanca, Tommaso Maria Brugo, and Luca Cristofolini. Use of digital image correlation to investigate the biomechanics of the vertebra. *Journal of Mechanics in Medicine and Biology*, 15(02):1540004, 2015.

[131] E Dall'Ara, D Barber, and M Viceconti. About the inevitable compromise between spatial resolution and accuracy of strain measurement for bone tissue: A 3d zero-strain study. *Journal of biomechanics*, 47(12):2956–2963, 2014.

[132] H Haddadi and S Belhabib. Use of rigid-body motion for the investigation and estimation of the measurement errors related to digital image correlation technique. *Optics and Lasers in Engineering*, 46(2):185–196, 2008.

[133] Nedaa Amraish, Andreas Reisinger, and Dieter H Pahr. Robust filtering options for higher-order strain fields generated by digital image correlation. *Applied Mechanics*, 1(4):174–192, 2020.

[134] Pascal Lava, Steven Cooreman, and Dimitri Debruyne. Study of systematic errors in strain fields obtained via dic using heterogeneous deformation generated by plastic fea. *Optics and Lasers in Engineering*, 48(4):457–468, 2010.

[135] Rafael C. Gonzalez and Richard E. Woods. *Digital Image Processing*. Addison-Wesley Longman Publishing Co., Inc., USA, 2nd edition, 1992.

[136] Hubert W Schreier, Joachim R Braasch, and Michael A Sutton. Systematic errors in digital image correlation caused by intensity interpolation. *Optical engineering*, 39(11):2915–2921, 2000.

[137] Yihao Zhou, Chen Sun, Yuntao Song, and Jubing Chen. Image pre-filtering for measurement error reduction in digital image correlation. *Optics and Lasers in Engineering*, 65:46–56, 2015.

[138] Bing Pan. Bias error reduction of digital image correlation using gaussian pre-filtering. *Optics and Lasers in Engineering*, 51(10):1161–1167, 2013.

[139] Bing Pan, Dafang Wu, Zhaoyang Wang, and Yong Xia. High-temperature digital image correlation method for full-field deformation measurement at 1200 c. *Measurement science and technology*, 22(1):015701, 2010.

[140] Wei Tong. An evaluation of digital image correlation criteria for strain mapping applications. *Strain*, 41(4):167–175, 2005.

[141] Yaofeng Sun, John HL Pang, Chee Khuen Wong, and Fei Su. Finite element formulation for a digital image correlation method. *Applied optics*, 44(34):7357–7363, 2005.

[142] ASTM International. E8," standard test methods for tension testing of metallic materials. *Annual book of ASTM standards*, 3:57–72, 2004.

[143] Corneliu Cofaru, Wilfried Philips, and Wim Van Paepegem. A novel speckle pattern—adaptive digital image correlation approach with robust strain calculation. *Opt. Lasers Eng.*, 50(2):187–198, 2012.

[144] Bing Pan, Jieyu Yuan, and Yong Xia. Strain field denoising for digital image correlation using a regularized cost-function. *Opt. Lasers Eng.*, 65:9–17, 2015.

[145] Corneliu Cofaru, Wilfried Philips, and Wim Van Paepegem. Improved newton–raphson digital image correlation method for full-field displacement and strain calculation. *Appl Opt*, 49(33):6472–6484, 2010.

[146] Bing Pan and Long Tian. Advanced video extensometer for non-contact, real-time, high-accuracy strain measurement. *Optics express*, 24(17):19082–19093, 2016.

[147] Přemysl Janíček, Marek Blažo, Petr Navrátil, Tomáš Návrat, and Petr Vosynek. Accuracy testing of the dic optical measuring method the aramis system by gom. In *49th International Scientific Conference*, page 139, 2011.

[148] Sudharshan Venkatesan, Ling Yin, Shankar Kalyanasundaram, Qing-Hua Qin, et al. A study on the real time strain measurement system for analysis of strain evolution and failure behavior of cortical bone materials. In *Materials Forum*, volume 33, 2009.

[149] Dong Sheng Zhang and Dwayne D Arola. Applications of digital image correlation to biological tissues. *Journal of Biomedical Optics*, 9(4):691–700, 2004.

[150] Gunthard Benecke, Michael Kerschnitzki, Peter Fratzl, and Himadri S Gupta. Digital image correlation shows localized deformation bands in inelastic loading of fibrolamellar bone. *Journal of Materials Research*, 24(2):421–429, 2009.

[151] Elise F Morgan, Ginu U Unnikrisnan, and Amira I Hussein. Bone mechanical properties in healthy and diseased states. *Annual review of biomedical engineering*, 20:119–143, 2018.

[152] Rajesh Ghosh, Sanjay Gupta, Alex Dickinson, and Martin Browne. Experimental validation of finite element models of intact and implanted composite hemipelvises using digital image correlation. *Journal of biomechanical engineering*, 134:081003, 08 2012.

[153] Rodrigo Tiossi, Marco AA Vasco, Lianshan Lin, Heather J Conrad, Osvaldo L Bezzon, Ricardo F Ribeiro, and Alex SL Fok. Validation of finite element models for strain analysis of implant-supported prostheses using digital image correlation. *Dental Materials*, 29(7):788–796, 2013.

[154] Alexander Synek and Dieter H Pahr. Plausibility and parameter sensitivity of micro-finite element-based joint load prediction at the proximal femur. *Biomechanics and Modeling in Mechanobiology*, 17(3):843–852, 2018.

[155] Saulo Martelli, Peter Pivonka, and Peter R Ebeling. Femoral shaft strains during daily activities: implications for atypical femoral fractures. *Clinical Biomechanics*, 29(8):869–876, 2014.

[156] Jae Young Rho, Richard B Ashman, and Charles H Turner. Young's modulus of trabecular and cortical bone material: ultrasonic and microtensile measurements. *Journal of biomechanics*, 26(2):111–119, 1993.

[157] M Cuppone, BB Seedhom, E Berry, and AE Ostell. The longitudinal young's modulus of cortical bone in the midshaft of human femur and its correlation with ct scanning data. *Calcified tissue international*, 74(3):302–309, 2004.

[158] Sabah Nobakhti, Orestis L Katsamenis, Nizar Zaarour, Georges Limbert, and Philipp J Thurner. Elastic modulus varies along the bovine femur. *Journal of the mechanical behavior of biomedical materials*, 71:279–285, 2017.

[159] L JOSEPH MELTON III, Stephen H Kan, Mark A Frye, Heinz W Wahner, W Michael O'fallon, and B Lawrence Riggs. Epidemiology of vertebral fractures in women. *American journal of epidemiology*, 129(5):1000–1011, 1989.

[160] Ming Ding. Age variations in the properties of human tibial trabecular bone and cartilage. *Acta Orthopaedica Scandinavica*, 71(sup292):i–45, 2000.

[161] Ji Wang, Bin Zhou, Ian Parkinson, C David L Thomas, John G Clement, Nick Fazzalari, and X Edward Guo. Trabecular plate loss and deteriorating elastic modulus of femoral trabecular bone in intertrochanteric hip fractures. *Bone research*, 1(1):346–354, 2013.

[162] Dennis R Cater and Wilson C Hayes. The compressive behavior of bone as a two-phase porous structure. *Journal of Bone Joint Surgery*, 59:954–962, 1977.

[163] Martin Stauber, Laurent Rapillard, G Harry van Lenthe, Philippe Zysset, and Ralph Müller. Importance of individual rods and plates in the assessment of bone quality and their contribution to bone stiffness. *Journal of Bone and Mineral Research*, 21(4):586–595, 2006.

[164] Robert W Goulet, Steven A Goldstein, Michael J Ciarelli, Janet L Kuhn, MB Brown, and LA Feldkamp. The relationship between the structural and orthogonal compressive properties of trabecular bone. *Journal of biomechanics*, 27(4):375–389, 1994.

[165] Tony M Keaveny, Edward F Wachtel, X Edward Guo, and Wilson C Hayes. Mechanical behavior of damaged trabecular bone. *Journal of biomechanics*, 27(11):1309–1318, 1994.

[166] Tony S Keller. Predicting the compressive mechanical behavior of bone. *Journal of biomechanics*, 27(9):1159–1168, 1994.

[167] J Kabel, B Van Rietbergen, A Odgaard, and R Huiskes. Constitutive relationships of fabric, density, and elastic properties in cancellous bone architecture. *Bone*, 25(4):481–486, 1999.

[168] Eelco Verhulp, Bert van Rietbergen, Ralph Müller, and Rik Huiskes. Indirect determination of trabecular bone effective tissue properties using micro-finite element simulations. *Analyses of trabecular bone failure*, page 53, 2006.

[169] Ara Nazarian, Dietrich von Stechow, David Zurakowski, Ralph Müller, and Brian D Snyder. Bone volume fraction explains the variation in strength and

stiffness of cancellous bone affected by metastatic cancer and osteoporosis. *Calcified tissue international*, 83(6):368–379, 2008.

[170] Łukasz Cyganik, Marcin Binkowski, Grzegorz Kokot, Tomasz Rusin, Paulina Popik, Filip Bolechała, Roman Nowak, Zygmunt Wróbel, and Antoni John. Prediction of young's modulus of trabeculae in microscale using macro-scale's relationships between bone density and mechanical properties. *Journal of the mechanical behavior of biomedical materials*, 36:120–134, 2014.

[171] Terence J Wilkin, Jan Dequeker, Devasenan Devendra, and Frank P Luyten. Bone densitometry is not a good predictor of hip fractureforagainst. *Bmj*, 323(7316):795–799, 2001.

[172] Francesc Levrero-Florencio, Lee Margetts, Erika Sales, Shuqiao Xie, Krishnagoud Manda, and Pankaj Pankaj. Evaluating the macroscopic yield behaviour of trabecular bone using a nonlinear homogenisation approach. *journal of the mechanical behavior of biomedical materials*, 61:384–396, 2016.

[173] Simone Tassani and George K Matsopoulos. The micro-structure of bone trabecular fracture: an inter-site study. *Bone*, 60:78–86, 2014.

[174] Vasileios Ch Korfiatis, Simone Tassani, and George K Matsopoulos. A new ensemble classification system for fracture zone prediction using imbalanced micro-ct bone morphometrical data. *IEEE journal of biomedical and health informatics*, 22(4):1189–1196, 2017.

[175] Simone Tassani, Martino Pani, Jerome Noailly, and Miguel Angel Gonzalez Ballester. Trabecular fracture zone might not be the higher strain region of the trabecular framework. *Frontiers in Materials*, 5:6, 2018.

[176] GH Bell, Olive Dunbar, JS Beck, and A Gibb. Variations in strength of vertebrae with age and their relation to osteoporosis. *Calcified tissue research*, 1(1):75–86, 1967.

[177] Paul R Townsend, Robert M Rose, and Eric L Radin. Buckling studies of single human trabeculae. *Journal of biomechanics*, 8(3-4):199–201, 1975.

[178] LJ Gibson. The mechanical behaviour of cancellous bone. *Journal of biomechanics*, 18(5):317–328, 1985.

[179] JS Stölken and JH Kinney. On the importance of geometric nonlinearity in finite-element simulations of trabecular bone failure. *Bone*, 33(4):494–504, 2003.

[180] Lis Mosekilde, EN Ebbesen, L Tornvig, and JS Thomsen. Trabecular bone structure and strength-remodelling and repair. *J Musculoskelet Neuronal Interact*, 1(1):25–30, 2000.

[181] Jacqueline G Garrison, Constance L Slaboch, and Glen L Niebur. Density and architecture have greater effects on the toughness of trabecular bone than damage. *Bone*, 44(5):924–929, 2009.

[182] Xiutao Shi, X Sherry Liu, Xiang Wang, X Edward Guo, and Glen L Niebur. Type and orientation of yielded trabeculae during overloading of trabecular bone along orthogonal directions. *Journal of biomechanics*, 43(13):2460–2466, 2010.

[183] Elsie F Morgan, Oscar C Yeh, and Tony M Keaveny. Damage in trabecular bone at small strains. *European journal of morphology*, 42(1-2):13–21, 2005.

[184] BD Snyder, S Piazza, WT Edwards, and WC Hayes. Role of trabecular morphology in the etiology of age-related vertebral fractures. *Calcified tissue international*, 53(1):S14–S22, 1993.

[185] Jens Bay Vegger, Annemarie Brüel, and Jesper Skovhus Thomsen. Vertical trabeculae are thinned more than horizontal trabeculae in skeletal-unloaded rats. *Calcified tissue international*, 97(5):516–526, 2015.

[186] Aaron J Fields, Gideon L Lee, X Sherry Liu, Michael G Jekir, X Edward Guo, and Tony M Keaveny. Influence of vertical trabeculae on the compressive strength of the human vertebra. *Journal of Bone and Mineral Research*, 26(2):263–269, 2011.

[187] Bert van Rietbergen. Micro-fe analyses of bone: state of the art. *Noninvasive assessment of trabecular bone architecture and the competence of bone*, pages 21–30, 2001.

[188] Romain Rieger, Jean-Charles Auregan, and Thierry Hoc. Micro-finite-element method to assess elastic properties of trabecular bone at micro-and macroscopic level. *Morphologie*, 102(336):12–20, 2018.

[189] Eelco Verhulp, Bert Van Rietbergen, Ralph Müller, and Rik Huiskes. Micro-finite element simulation of trabecular-bone post-yield behaviour–effects of material model, element size and type. *Computer methods in biomechanics and biomedical engineering*, 11(4):389–395, 2008.

[190] Marta Peña Fernández, Alexander P Kao, Roxane Bonithon, David Howells, Andrew J Bodey, Kazimir Wanelik, Frank Witte, Richard Johnston, Hari Arora, and Gianluca Tozzi. Time-resolved in situ synchrotron-microct: 4d deformation of bone and bone analogues using digital volume correlation. *Acta Biomaterialia*, 131:424–439, 2021.

[191] Holly D Barth, Maximilien E Launey, Alastair A MacDowell, Joel W Ager III, and Robert O Ritchie. On the effect of x-ray irradiation on the deformation and fracture behavior of human cortical bone. *Bone*, 46(6):1475–1485, 2010.

[192] Holly D Barth, Elizabeth A Zimmermann, Eric Schaible, Simon Y Tang, Tamara Alliston, and Robert O Ritchie. Characterization of the effects of x-ray irradiation on the hierarchical structure and mechanical properties of human cortical bone. *Biomaterials*, 32(34):8892–8904, 2011.

[193] Bert van Rietbergen, Harrie Weinans, Rik Huiskes, and A Odgaard. A new method to determine trabecular bone elastic properties and loading using micromechanical finite-element models. *Journal of biomechanics*, 28(1):69–81, 1995.

[194] Anthony JC Ladd and John H Kinney. Numerical errors and uncertainties in finite-element modeling of trabecular bone. *Journal of biomechanics*, 31(10):941–945, 1998.

[195] Anders Odgaard, Ivan Hvid, and Frank Linde. Compressive axial strain distributions in cancellous bone specimens. *Journal of biomechanics*, 22(8-9):829–835, 1989.

[196] Harun H Bayraktar, Elise F Morgan, Glen L Niebur, Grayson E Morris, Eric K Wong, and Tony M Keaveny. Comparison of the elastic and yield properties of human femoral trabecular and cortical bone tissue. *Journal of biomechanics*, 37(1):27–35, 2004.

[197] Nedaa Amraish, Andreas Reisinger, and Dieter Pahr. A novel specimen shape for measurement of linear strain fields by means of digital image correlation. *Scientific Reports*, 11(1):1–13, 2021.

[198] Christopher J Hernandez, Simon Y Tang, Bethany M Baumbach, Paul B Hwu, A Nico Sakkee, Frits Van Der Ham, Jeroen DeGroot, Ruud A Bank, and Tony M Keaveny. Trabecular microfracture and the influence of pyridinium and non-enzymatic glycation-mediated collagen cross-links. *Bone*, 37(6):825–832, 2005.

[199] R Jungmann, ME Szabo, G Schitter, Raymond Yue-Sing Tang, D Vashishth, PK Hansma, and PJ Thurner. Local strain and damage mapping in single trabeculae during three-point bending tests. *Journal of the mechanical behavior of biomedical materials*, 4(4):523–534, 2011.

[200] Tor Hildebrand, Andres Laib, Ralph Müller, Jan Dequeker, and Peter Rüegsegger. Direct three-dimensional morphometric analysis of human cancellous bone: microstructural data from spine, femur, iliac crest, and calcaneus. *Journal of bone and mineral research*, 14(7):1167–1174, 1999.

[201] David P Fyhrie and MB Schaffler. Failure mechanisms in human vertebral cancellous bone. *Bone*, 15(1):105–109, 1994.

[202] David L Kopperdahl and Tony M Keaveny. Yield strain behavior of trabecular bone. *Journal of biomechanics*, 31(7):601–608, 1998.

[203] Ralph Müller, SC Gerber, and WC Hayes. Micro-compression: a novel technique for the nondestructive assessment of local bone failure. *Technology and Health Care*, 6(5-6):433–444, 1998.

[204] Nedaa Amraish and Dieter H Pahr. High-resolution local trabecular strain within trabecular structure under cyclic loading. *Journal of the Mechanical Behavior of Biomedical Materials*, page 106318, 2023.

Appendix A: List of publications

Peer-reviewed journal publications

Amraish, N., Reisinger, A., Pahr, D.H. Robust Filtering Options for Higher-Order Strain Fields Generated by Digital Image Correlation. Appl. Mech. 2020, 1, 174-192. https://doi.org/10.3390/applmech1040012

Amraish, N., Reisinger, A., Pahr, D. A novel specimen shape for measurement of linear strain fields by means of digital image correlation. Sci Rep 11, 17515 (2021). https://doi.org/10.1038/s41598-021-97085-x

Amraish, N., Pahr, D. High-resolution local trabecular strain within trabecular structure under cyclic loading. JMBBM (2023) https://doi.org/10.1016/j.jmbbm.2023.106318.

Conference contributions

Amraish, N.; Reisinger, A.; Pahr, D.H. Accuracy and precision of full field surface strain measurements. In European Society of Biomechanics. 2019. Vienna: TU Verlag, S. 223.

Amraish, N.; Reisinger, A.; Pahr, D.H. Measurement of linear strain fields by means of digital image correlation. In European Society of Biomechanics. 2021.

Amraish, N., and Pahr, D.H. New insights into high-resolution strain fields of trabecular bone using digital image correlation. In European Society of Biomechanics. 2022.

Amraish, N., and Pahr, D.H. High-resolution local trabecular strain within trabecular structure. In European Society of Biomechanics. 2024.